

DTIC FILE COPY

WRDC-TR-89-4085

AD-A218 063



THRESHOLD FATIGUE CRACK GROWTH BEHAVIOR

F.K. Haake, G. C. Salivar, E. H. Hindle, J. W. Fischer, C. G. Annis, Jr.

United Technologies Corporation
Pratt & Whitney
Government Engine Business
P. O. Box 109600
West Palm Beach, Florida 33410-9600

October 1989

Final Report for Period August 1985 - July 1988

Approved for public release; distribution unlimited

DTIC
ELECTED
FEB 16 1990
S B D
(Co)

MATERIALS LABORATORY
WRIGHT RESEARCH DEVELOPMENT CENTER
AIR FORCE SYSTEMS COMMAND
WRIGHT-PATTERSON AIR FORCE BASE, OHIO 45433-6533

90 02 14 010

NOTICE

When government drawings, specifications, or other data are used for any purpose other than in connection with a definitely government-related procurement, the United States Government incurs no responsibility or any obligation whatsoever. The fact that the government may have formulated or in any way supplied the said drawings, specifications, or other data, is not to be regarded by implication, or otherwise in any manner construed, as licensing the holder, or any other person or corporation; or as conveying any rights or permission to manufacture, use, or sell any patented invention that may in any way be related thereto.

This report has been reviewed by the Office of Public Affairs (ASD/CPA) and is releasable to the National Technical Information Service (NTIS). At NTIS, it will be available to the general public, including foreign nations.

This technical report has been reviewed and is approved for publication.



STEPHEN J. BALSONE, Capt, USAF
FOR THE COMMANDER



THEODORE NICHOLAS
Metals Behavior Branch
Metals and Ceramics Division



ALLAN W. GUNDERSON
Acting Branch Chief
Metals Behavior Branch
Metals and Ceramics Division

If your address has changed, if you wish to be removed from our mailing list, or if the addressee is no longer employed by your organization, please notify WRDC/MLLN, Wright-Patterson AFB OH 45433-6533 to help us maintain a current mailing list.

Copies of this report should not be returned unless return is required by security considerations, contractual obligations, or notice on a specific document.

UNCLASSIFIED

SECURITY CLASSIFICATION OF THIS PAGE

REPORT DOCUMENTATION PAGE				Form Approved OMB No. 0704-0188
1a. REPORT SECURITY CLASSIFICATION None		1b. RESTRICTIVE MARKINGS None		
2a. SECURITY CLASSIFICATION AUTHORITY N/A		3. DISTRIBUTION/AVAILABILITY OF REPORT Approved for public release; distribution unlimited.		
2b. DECLASSIFICATION/DOWNGRADING SCHEDULE N/A				
4. PERFORMING ORGANIZATION REPORT NUMBER(S) P&W/GEB/FR-20431		5. MONITORING ORGANIZATION REPORT NUMBER(S) WRDC-TR-89-4085		
6a. NAME OF PERFORMING ORGANIZATION United Technologies Corporation Pratt & Whitney/Government Engine Business	6b. OFFICE SYMBOL <i>(If applicable)</i>	7a. NAME OF MONITORING ORGANIZATION Materials Laboratory (WRDC/MLLN)		
6c. ADDRESS (City, State, and ZIP Code) P. O. Box 109600 West Palm Beach, FL 33410-9600		7b. ADDRESS (City, State, and ZIP Code) Wright Research Development Center Wright-Patterson AFB, Ohio 45433-6533		
8a. NAME OF FUNDING/SPONSORING ORGANIZATION WRDC/MLLN	8b. OFFICE SYMBOL <i>(If applicable)</i>	9. PROCUREMENT INSTRUMENT IDENTIFICATION NUMBER F33615-85-C-5050		
8c. ADDRESS (City, State, and ZIP Code) Wright-Patterson AFB, Ohio 45433-6533		10. SOURCE OF FUNDING NOS. PROGRAM ELEMENT NO. PROJECT NO. TASK NO. WORK UNIT ACCESSION NO. 62102F 2420 01 63		
11. TITLE <i>(Include Security Classification)</i> Threshold Fatigue Crack Growth Behavior				
12. PERSONAL AUTHOR(S) F. K. Haake, G. C. Salivar, E. H. Hindle, J. W. Fischer, C. G. Annis, Jr.				
13a. TYPE OF REPORT Final	13b. TIME COVERED FROM 8-1-85 TO 7-31-88	14. DATE OF REPORT(Year, Month, Day) 1989 October		15. PAGE COUNT 111
16. SUPPLEMENTARY NOTATION				
17. COSATI CODES		18. SUBJECT TERMS <i>(Continue on reverse if necessary and identify by block number)</i> Threshold Crack Growth, Fracture Mechanics, High Cycle Fatigue, Fatigue, (KR)		
FIELD	GROUP	SUB. GR.		
19. ABSTRACT <i>(Continue on reverse if necessary and identify by block number)</i> This constitutes the Final Report for Air Force Contract F33615-85-C-5050, "Threshold Fatigue Crack Growth Behavior." The sponsoring agency was the Materials Laboratory, Wright Research Development Center, Wright-Patterson Air Force Base, Dayton, Ohio. The period of performance was 1 August 1985 through 31 July 1988. The objective of the program was to develop and demonstrate a methodology for predicting the high cycle fatigue (HCF) life of a gas turbine engine blade alloy containing defects of either intrinsic or extrinsic origin using threshold fracture mechanics concepts. The program centered around experimental measurements of threshold stress intensity (ΔK_{th}) for Ti 8Al-1Mo-1V and the assessment of influencing factors such as frequency, stress ratio, and temperature. The uniqueness of ΔK_{th} , as well as the effects of time-dependent crack growth behavior were also investigated. Finally, an attempt was made to model HCF behavior based on fracture mechanics principles and the ΔK_{th} data base. (KR)				
20. DISTRIBUTION/AVAILABILITY OF ABSTRACT <input checked="" type="checkbox"/> UNCLASSIFIED/UNLIMITED <input type="checkbox"/> SAME AS RPT. <input type="checkbox"/> DTIC USERS			21. ABSTRACT SECURITY CLASSIFICATION Unclassified	
22a. NAME OF RESPONSIBLE INDIVIDUAL Capt Stephen J. Balsone		22b. TELEPHONE (Include Area Code) (513) 255-1346		22c. OFFICE SYMBOL WRDC/MLLN

UNCLASSIFIED

SECURITY CLASSIFICATION OF THIS PAGE

The following general conclusions are based on the results of this study:

ΔK_{th} is slightly decreased at elevated temperature and is insensitive to frequencies above 30 Hz. The addition of an intermittent dwell to high-frequency cycling causes a small increase in ΔK_{th} at high mean stresses, $R=0.7$ or greater. Threshold stress intensity remains approximately constant as a function of stress ratio after correction for closure or when the test technique minimizes closure. In the absence of these conditions, ΔK_{th} decreases with increasing stress ratio.

ΔK_{th} measurements vary with test specimen and procedure. This problem can be circumvented through closure correction, or a test technique which minimizes closure and load history effects.

HCF behavior of Ti 8-1-1 is degraded by the presence of FOD in those size ranges observed in engine fan and compressor blades, but not to the degree predicted by fracture mechanics calculations. (In practice, FOD of this size is removed by blending and polishing during periodic engine overhauls.)

HCF behavior in Ti 8-1-1 cannot be accurately predicted using simple fracture mechanics models and ΔK_{th} data. These models can predict rough trends for HCF behavior of material containing relatively large damage. A successful damage-based HCF life prediction system for the class of materials similar to Ti 8-1-1 would require the assessment of both crack initiation and propagation lives, and would likely require consideration of small flaw behavior. HCF modeling based on ΔK_{th} behavior may be applicable to materials containing large initial defects, or materials with low defect tolerance.

UNCLASSIFIED

SECURITY CLASSIFICATION OF THIS PAGE

FOREWORD

This work was performed under Air Force Contract F33615-85-C-5050, "Threshold Fatigue Crack Growth Behavior." The sponsoring agency was the Materials Laboratory, Wright Research Development Center, Wright-Patterson Air Force Base, Dayton, Ohio. The Air Force Program Monitor was Capt S. J. Balsone. The program was conducted at the Materials Engineering Laboratories, Pratt and Whitney, West Palm Beach, Florida. The principal investigator for the program was F. K. Haake. The P&W program manager was C. G. Annis, Jr., reporting to M. C. VanWanderham. Florida Atlantic University, Boca Raton, Florida, was subcontracted to perform part of the threshold testing. That testing was directed by Dr G. C. Salivar. J. E. Heine was also instrumental in conducting the testing at FAU. The authors would also like to acknowledge the contributions of J. R. Jira who made closure measurements at WRDC/MLLN and T. Watkins who developed the computer software at P&W. We would also like to thank the technicians of the Fracture Mechanics and High Cycle Fatigue groups at P&W for their part in conducting the testing for this program.

Accession Per	
NTIS GRA&I	<input checked="" type="checkbox"/>
DTIC TAB	<input type="checkbox"/>
Unannounced	<input type="checkbox"/>
Justification	
By _____	
Distribution/	
Availability Codes	
Dist	Avail and/or Special
A-1	



SUMMARY

The Air Force is currently developing technology for a damage-tolerance approach to the design of gas turbine engine components. The Turbine Engine Structural Integrity Program (ENSIP) is intended to provide an organized approach to the structural design, analysis, qualification, production, and life management of gas turbine engines. Under ENSIP, fracture critical structural components will be capable of maintaining adequate damage tolerance to handling and foreign object damage (FOD) as well as material, manufacturing, and processing defects. The Threshold Fatigue Crack Growth Behavior program is directly applicable to the ENSIP philosophy. The understanding of threshold behavior provides the basis for improved life prediction models and the foundation for a systematic technology for damage-tolerant design with alloys presently in service and with advanced alloys.

The objective of the program was to develop and demonstrate a methodology for predicting the high cycle fatigue (HCF) life of a gas turbine engine blade alloy containing defects of either intrinsic or extrinsic origin using threshold fracture mechanics concepts. The program centered around experimental measurements of threshold stress intensity (ΔK_{th}) for Ti 8Al-1Mo-1V, and the assessment of influencing factors such as frequency, stress ratio, and temperature. The uniqueness of ΔK_{th} , as well as the effects of time-dependent crack growth behavior were also investigated. Finally, an attempt was made to model HCF behavior based on fracture mechanics principles and the ΔK_{th} data base.

The following general conclusions are based on the results of this study:

ΔK_{th} is slightly decreased at elevated temperature and is insensitive to frequencies above 30 Hz. The addition of an intermittent dwell to high-frequency cycling causes a small increase in ΔK_{th} at high mean stresses, R=0.7 or greater. Threshold stress intensity remains approximately constant as a function of stress ratio after correction for closure or when the test technique minimizes closure. In the absence of these conditions, ΔK_{th} decreases with increasing stress ratio.

ΔK_{th} measurements vary with test specimen and procedure. This problem can be circumvented through closure correction, or a test technique which minimizes closure and load history effects.

HCF behavior of Ti 8-1-1 is degraded by the presence of FOD in those size ranges observed in engine fan and compressor blades, but not to the degree predicted by fracture mechanics calculations. (In practice, FOD of this size is removed by blending and polishing during periodic engine overhauls.)

HCF behavior in Ti 8-1-1 cannot be accurately predicted using simple fracture mechanics models and ΔK_{th} data. These models can predict rough trends for HCF behavior of material containing relatively large damage. A successful damage-based HCF life prediction system for the class of materials similar to Ti 8-1-1 would require the assessment of both crack initiation and propagation lives, and would likely require consideration of small flaw behavior. HCF modeling based on ΔK_{th} behavior may be applicable to materials containing large initial defects, or materials with low defect tolerance.

TABLE OF CONTENTS

<i>Section</i>	<i>Page</i>
I INTRODUCTION AND OBJECTIVES	1
Background and Overview of Technical Approach	1
II TASK 1 — MATERIAL SELECTION AND PROCUREMENT	6
III TASK II — THRESHOLD CRACK GROWTH BEHAVIOR	11
Test Specimen and Procedure	11
a. Increasing ΔK Threshold Testing	11
b. Decreasing ΔK Threshold Testing	17
Results	20
Stress Ratio Effect	22
Closure	30
Effect of Secondary Parameters	35
Test Method Comparisons	39
IV TASK III — SMOOTH BAR FATIGUE TESTING	45
Test Specimens and Procedure	45
Testing and Fractography Results	50
Testing	50
Fractography	63
V TASK IV — ANALYTICAL MODELING	72
1. Model Description	72
2. Results	73
VI TASK V — VALIDATION TESTING	83
VII DISCUSSION	91
1. Measurement of ΔK_{th}	85
2. Analytical Modeling Considerations	86
VIII CONCLUSIONS	89
REFERENCES	90
APPENDIX A — Florida Atlantic University	A-1
Computer Controlled Fatigue-Crack Growth Testing	A-1
Crack Mouth Opening Displacement (COD) Measurement at High Temperature	A-2
Resistive Furnace System	A-2
APPENDIX B — Threshold Testing	B-1

TABLE OF CONTENTS (Continued)

<i>Section</i>	<i>Page</i>
APPENDIX C — Axial Fatigue Results of PWA 1202	C-1
APPENDIX D — Monte Carlo Simulation	D-1

LIST OF ILLUSTRATIONS

<i>Figure</i>		<i>Page</i>
1	Characteristic da/dN Versus ΔK Curve	3
2	HCF-Related HPC Blade Failure Due to FOD	5
3	PWA 1202, Transverse Microstructure (100X, Kroll's Etch)	8
4	PWA 1202, Longitudinal Microstructure (100X, Kroll's Etch)	8
5	Crack Orientation for Threshold Crack Growth Specimens	9
6	Typical da/dN vs ΔK Curve Illustrating Near Threshold Point	12
7	Fatigue Crack Growth Threshold Specimen Configuration	13
8	Typical Threshold Specimens	14
9	Near-Threshold Crack Growth Test	15
10	Typical Threshold Crack Growth Specimen Fracture Surface	16
11	Average Crack Length Measurements	16
12	Compact Specimen for Alternate Testing Method	17
13	Typical Compact-Type (CT) Specimen	18
14	Effect of Closure on Stress Intensity Range	20
15	Commonly Recognized Closure Mechanisms	20
16	PWA 1202 Near-Threshold Fatigue Crack Growth Rates, 27°C, R=0.1, 20 Hz	22
17	PWA 1202 Near-Threshold Fatigue Crack Growth Rates, 260°C, R=0.1, 20 Hz	23
18	PWA 1202 Near-Threshold Fatigue Crack Growth Rates, 260°C, R=0.5, 20 Hz	24
19	PWA 1202 Near-Threshold Fatigue Crack Growth Rates, 260°C, R=0.7, 20 Hz	25
20	Combined Near-Threshold and Constant Amplitude FCG Data, 27°C, R=0.1, 20 Hz	26
21	Combined Near-Threshold and Constant Amplitude FCG Data, 260°C, R=0.1, 20 Hz	27

LIST OF ILLUSTRATIONS (Continued)

Figure		Page
22	Combined Near-Threshold and Constant Amplitude FCG Data, 260°C, R=0.5, 20 Hz	28
23	Combined Near-Threshold and Constant Amplitude FCG Data, 260°C, R=0.7, 20 Hz	29
24	Threshold Stress Intensity Plotted as a Function of Stress Ratio	30
25	Schematic Representation of Differential Load-COD Trace	31
26	Load vs COD Trace With Indicated Closure Levels, Testing at RT, R=0.1, 20 Hz	32
27	Load-COD Plot Showing the Opening Load Determined by the Tangent-Intercept Method	33
28	Near-Threshold Fatigue Crack Growth Without Correction for Crack Closure for R=0.1, 0.5, 0.7 at 260°C	34
29	Near-Threshold Fatigue Crack Growth With Correction for Crack Closure for R=0.1, 0.5, 0.7 at 260°C	35
30	Near-Threshold FCG Curves With Correction for Crack Closure Using 16-Percent Slope Deviation Method to Determine Opening Load	36
31	The Effect of Crack Length on the Opening Load for Specimens with Crack Closure	37
32	Comparison of the FCG Curves From Sequential Threshold Tests, Demonstrating Negligible Crack Length Effects	38
33	Combined High-Frequency/Hold-Time Cycle for Determining Time Dependence	38
34	Fracture Surface Comparison of 200-Hz vs 200-Hz/2-Minute Dwell Threshold Tests	39
35	Comparison of Increasing-R and Constant-R Near-Threshold Fatigue Crack Growth Rates at 260°C	41
36	Constant K_{max} Increasing-R Threshold Crack Growth Rates at 260°C, 20 Hz	42
37	PWA 1202 Crack Growth Rate Data, Comparing Methods for Determining ΔK_{th} at 27°C, R=0.1, 30 Hz	43
38	PWA 1202 Crack Growth Rate Data, Comparing Methods for Determining ΔK_{th} at 260°C, R=0.1, 30 Hz	44

LIST OF ILLUSTRATIONS (Continued)

<i>Figure</i>		<i>Page</i>
39	Smooth HCF Specimen	45
40	Typical Smooth HCF Specimen	46
41	V-Notch in Ti 8-1-1 1st-Stage Fan Blades	47
42	Typical Notched HCF Specimen With a 0.20-mm-Deep, 60-Degree V-Notch	48
43	Modified Goodman Diagram For PWA 1202 at 27°C	50
44	Modified Goodman Diagram For PWA 1202 at 500°C	51
45	Axial High Cycle Fatigue Results for PWA 1202 at 27°C, R=-1.0, $K_t = 1.0$	51
46	Axial High Cycle Fatigue Results for PWA 1202 at 27°C, R=0.1, $K_t = 1.0$	52
47	Axial High Cycle Fatigue Results for PWA 1202 at 27°C, R=0.5, $K_t = 1.0$	52
48	Axial High Cycle Fatigue Results for PWA 1202 at 260°C, R=-1.0, $K_t = 1.0$	53
49	Axial High Cycle Fatigue Results for PWA 1202 at 260°C, R=0.1, $K_t = 1.0$	53
50	Axial High Cycle Fatigue Results for PWA 1202 at 260°C, R=0.5, $K_t = 1.0$	54
51	Modified Goodman Diagram for PWA 1202 at 260°C, Comparing Smooth, 0.2-mm Defect, and 0.38-mm Defect Specimens	54
52	Axial High Cycle Fatigue Results for PWA 1202 at 260°C, R=-1.0, 0.2-mm Defect	55
53	Axial High Cycle Fatigue Results for PWA 1202 at 260°C, R=0.1, 0.2-mm Defect	55
54	Axial High Cycle Fatigue Results for PWA 1202 at 260°C, R=0.5, 0.2-mm Defect	56
55	Axial High Cycle Fatigue Results for PWA 1202 at 260°C, R=-1.0, 0.38-mm Defect	56
56	Axial High Cycle Fatigue Results for PWA 1202 at 260°C, R=0.1, 0.38-mm Defect	57

LIST OF ILLUSTRATIONS (Continued)

<i>Figure</i>		<i>Page</i>
57	Axial High Cycle Fatigue Results for PWA 1202 at 260°C, R=0.5, 0.38-mm Defect	58
58	PWA 1202 HCF Fracture Surface, Tested With 0.20-mm-Deep Sharp Notch at 260°C, R=0.1, 30 Hz, and (a) 552 MPa or (b) 414 MPa	59
59	PWA 1202 HCF Fracture Surface, Tested at 260°C, R=0.1, 30 Hz, and 552 MPa, Arrow Indicates Probable Initiation Site at Notch	60
60	Notched HCF Secimen Fracture Surface. Tested At 260°C, R=0.1, σ_{max} = 414 MPa. Notch Depth Is 0.46 mm. Arrow Indicates Initiation Site At Base of Notch	61
61	Notched HCF Secimen Fracture Surface. Tested At 260°C, R=0.1, σ_{max} = 483 MPa. Notch Depth Is 0.28 mm. Arrow Indicates Initiation Site At Base of Notch	62
62	Axial High Cycle Fatigue Results For PWA 1202 at 260°C, R=0.5, K_t = 1.0, 30-Hz vs 30-Hz/2-min.-Dwell	63
63	Axial High Cycle Fatigue Results For PWA 1202 at 260°C, R=0.7, K_t = 1.0, 30-Hz vs 30-Hz/2-min.-Dwell	64
64	HCF Failure Origin Tested at RT, R=0.1, 548 MPa, Arrow Indicates Origin	65
65	Smooth HCF Fracture Surface Tested at 260°C, R=0.1, σ_{max} = 552 MPa. For a-c, Arrows Indicate Fracture Origin; d shows Striations in High ΔK Region	66
66	HCF Fracture Surface Showing Fatigue Striations in High ΔK Region Tested at 27°C, 480 MPa	67
67	Threshold Specimen Fracture Surfaces; Area Adjacent to Precrack	68
68	HCF Fracture Surface With Subsurface Initiation Tested at 260°C, R=0.7, 30 Hz, 828 MPa	69
69	HCF Fracture Surface With Subsurface Initiation Tested at 260°C, R=0.7, 30-Hz/2-Min-Dwell, 828 MPa	70
70	HCF Fracture Surface: Area Removed From Notch Showing Fine Striations. Tested at 260°C, R=0.1, 30 Hz, 552 MPa	71
71	Repairable FOD Distribution	75
72	Non-Repairable FOD Distribution	76
73	Ti 8-1-1 IMQ Distribution	77

LIST OF ILLUSTRATIONS (Continued)

<i>Figure</i>		<i>Page</i>
74	Fracture Based Goodman Approximation vs HCF Test Data at 27°C ..	78
75	Fracture Based Goodman Approximation vs HCF Test Data at 260°C ..	79
76	Simulated Goodman Diagrams vs HCF Test Data for Defect	80
77	HCF Fracture Surface Showing Fine Striations Approximately 0.4 mm from Origin; Tested at 27°C, R=0.1, T _{max} σ = 620 MPa	87

LIST OF TABLES

<i>Table</i>		<i>Page</i>
1	PWA 1202 Material Chemistry	7
2	Mechanical Property Specification Test	7
3	ΔK_{th} Test Results	21
4	ΔK_{th} Comparison	21
5	FOD Size Distributions for Repairable Blades	73
6	FOD Size Distributions for Non-Repairable Blades	73
7	Summary of FOD Sampling	77
8	Integrated Life Summary	81
9	HCF Tests with Inspections	84
B-1	Low Frequency Threshold Testing	B-1
B-2	High Frequency Threshold Testing	B-2
B-3	Tests Conducted at FAU-CT Geometry	B-3
C-1	Temp = 27°C K_t = 1.0	C-1
C-2	Temp = 260°C K_t = 1.0	C-2
C-3	Temp = 260°C 0.20mm Defect	C-3
C-4	Temp = 260°C 0.38mm Defect	C-3
C-5	Temp = 260°C K_t = 1.0, 30 Hz/2 Minute Dwell	C-4
D-1	Sample Input Dataset	D-2
D-2	Sample Output Dataset	D-2

SECTION I

INTRODUCTION AND OBJECTIVES

The U. S. Air Force is currently developing technology to allow for an eventual damage tolerant approach to the design of gas turbine engine components. The need for such a disciplined approach to turbine engine structural development has been illustrated by numerous structural problems resulting in a high level of maintenance and modification costs and even loss of aircraft. As a result, the Turbine Engine Structural Integrity Program (ENSIP) is intended to reduce these problems by providing an organized approach to the structural design, analysis, qualification, production, and life management of gas turbine engines.

The threshold fatigue crack growth behavior program is directly applicable to the ENSIP philosophy. Under ENSIP, fracture critical structural components will be capable of maintaining adequate damage tolerance in the presence of handling and foreign object damage (FOD) as well as material, manufacturing, and processing defects. The combination of high strength and low ductility in such components may promote initiation of fatigue cracks from inherent defects under cyclic loading. A better understanding of threshold behavior will provide the basis for improved life-prediction models and the foundation for a systematic technology for damage tolerant design of alloys presently in service and for advanced materials such as titanium aluminides.

High cycle fatigue (HCF) is a primary life limiting consideration in advanced blade design, and a lifting capability is necessary to assess the effects of defects to evaluate the durability of blade alloy. It is *not* realistic to assume a defect-free structure in a fracture critical component. Thus, it is important to have an approach which can correlate the HCF life of an alloy with initial defects using threshold fracture mechanics concepts. This program aims to demonstrate that threshold fracture mechanics concepts can be used to predict an HCF life without the need to generate complete (stress-cycle) S-N curve data at each defect size to determine a fatigue life.

The overall objective of this program was to develop and demonstrate a methodology for predicting the high cycle fatigue life of a gas turbine engine blade alloy containing defects of either intrinsic or extrinsic origin using threshold fracture mechanics concepts. Although the aim was to develop a generic technology, specific consideration has been given to alloys, defect sizes, and testing conditions representative of gas turbine engine components.

The program centered around experimental measurements of threshold stress intensity, ΔK_{th} , and the assessment of factors such as frequency, stress ratio, and temperature, which influence it. The uniqueness of ΔK_{th} , as well as the effects of time-dependent crack growth behavior have also been investigated.

Background and Overview of Technical Approach

Cyclic life, or fatigue capability, has been a major design criterion for aircraft gas turbine engine components for more than two decades. Both low cycle fatigue (LCF), usually associated with major engine throttle cycles, and HCF, usually associated with resonant vibration, have been considered. LCF frequently limits major rotating components, such as disks, spacers, and airfoil attachments, and is a direct result of the high thermal and mechanical stresses experienced by these components during major throttle excursions. LCF has historically been addressed by predicting the engine cycles or hours required to produce a small (1/32 inch) surface crack in a statistically small fraction of parts (1/1000). Component retirement life has often been based on this prediction.

Conversely, HCF has been addressed in a significantly different manner. HCF is usually also high frequency fatigue (HFF) for engine components, because it is most often associated with resonant vibration. Blades and their attachments are particularly susceptible to HCF since they are more easily excited at resonance than are disks or spacers. Typical frequencies range from below 100 Hz to over 3000 Hz. At such high frequencies, it is not practical either to predict or use predicted HCF life. Consequently, HCF capability is usually expressed in terms of "vibratory allowable" stresses. Components are designed to operate below the vibratory allowable stress limits with no resulting failures.

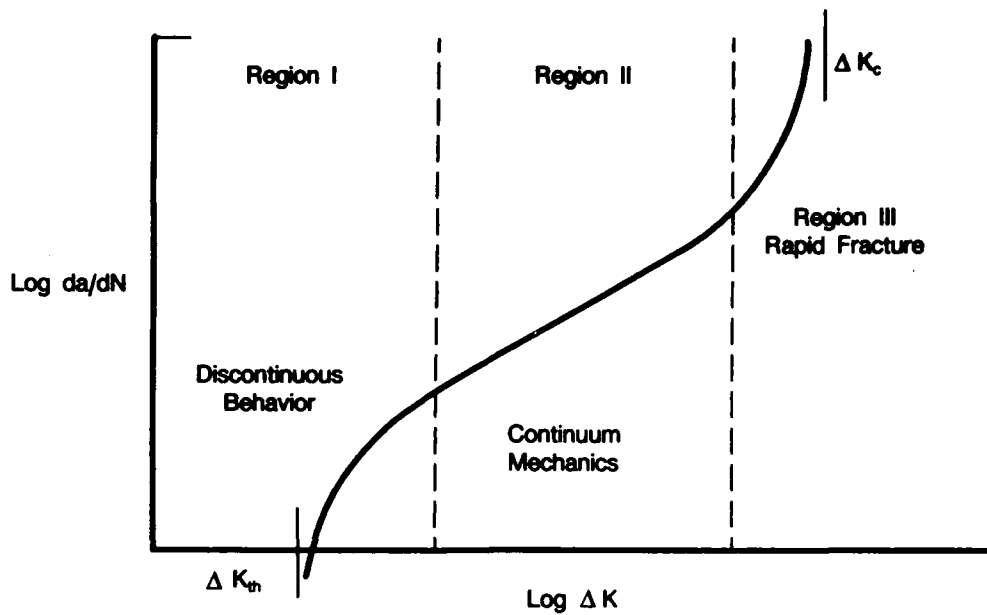
Cyclic (alternating) and mean (steady) stresses are considered jointly in estimating the allowable stress limits. The relationship of the endurance limit or fatigue strength to the vibratory and mean stresses is usually represented by a modified Goodman diagram. The Goodman diagram is determined by fatigue testing of blades and/or smooth bar specimens at temperatures of interest. Usually, the tests are run fully reversed, so that the mean stress is zero. A stress versus cycles-to-failure (S-N) curve is obtained, and the fatigue strength, which is usually estimated at 10^7 or 10^8 cycles, is used as a key point on the Goodman diagram. Many additional tests are then required to generate S-N curves for other mean stresses or stress ratios. The cost for generating an entire Goodman diagram then becomes quite high. Often, the diagram is estimated using the fully reversed-stress fatigue strength and tensile properties.

Beginning in the mid-1970s, changes in engine design and life prediction philosophy occurred, incorporating fracture mechanics concepts into design, life prediction, material selection, and inspection requirements. The Air Force ENSIP, which is now an engine design specification, requires extensive use of fracture mechanics analyses, particularly for fracture critical parts. Most of these components are disks, spacers, or cases; and the loading of concern is LCF. However, in single-engine aircraft, blades may be determined to be fracture critical components, where the primary loading of concern is HCF. Since the prediction of HCF life is not practical, the approach, even with ENSIP, has still been based on a "vibratory stress allowable" or Goodman diagram. An alternative approach to this convention could be based on the fracture mechanics threshold stress intensity, which is the topic of the proposed program. This approach would permit analytical handling of material defects based on initial material quality (IMQ), inspection flaw size limitations, and FOD. It could, if effective, reduce the large number of tests currently required to handle these variables while remaining consistent with ENSIP philosophy and requirements.

This program develops a methodology based on linear elastic fracture mechanics (LEFM) for converting threshold crack propagation behavior into the more common Goodman diagrams. The resulting blade design lifting algorithms take into account the level of possible prior damage, an essential element of ENSIP. An understanding of the applicability of, and limits to LEFM, is therefore essential to this undertaking.

The presence of a crack in a stressed component necessitates redistribution of stresses around the crack. The stress intensity factor is a parameter that reflects this redistribution and is a function of nominal stress, crack size, and part or specimen and crack geometries. The concept of stress intensity factor was originally defined for an infinitely sharp elastic crack tip, and it is this deformation that gives the material resistance to crack propagation.

The usefulness of LEFM depends on a uniparametric relationship between crack growth rate, da/dN , and the stress intensity factor range, ΔK . This relationship is illustrated schematically in Figure 1. The curve is usually roughly divided into three regions. Region I, where crack advance is discontinuous and measured growth is an average of behavior over many loading cycles. Continuum behavior predominates in Region II, and a unique relationship between ΔK and the resulting da/dN is best observed in this region. Rapid crack advance toward failure is observed in Region III. Threshold is defined as the behavior of the $da/dN-\Delta K$ relationship at the beginning of Region I.



FD 293812

Figure 1. Characteristic da/dN Versus ΔK Curve

Crack behavior under HCF, where many thousands of cycles can be accumulated rapidly (when a blade is resonating, for example), makes Region I the focus of this investigation. Threshold, ΔK_{th} , is the quasi-asymptotic value of the stress intensity range below which no crack advance will occur. Because K relates crack size, a , and applied stress, σ , the existence of a greatest lower bound, a threshold value, provides the theoretical basis for considering prior damage as well as service loading in ENSIP life assessment computations.

IMQ and the potential for manufacturing defects, such as machining damage or forging cracks, have received considerable attention since fracture mechanics concepts have been incorporated into engine component life predictions, particularly for large rotating components like disks and spacers. In these components, with large volumes of material and high LCF stresses, these types of defects are often associated with fatigue origins.

In powder nickel disk alloys, such as IN100, recent studies have shown that more than 50 percent of LCF origins may be associated with small material defects (References 1, 2). Conventional nickel alloys produced from ingot, such as Waspaloy, show a significantly reduced fraction of origins at microstructural defects or inclusions — about 20 percent, and the titanium alloy which was evaluated, Ti 6-2-4-6, showed only a small fraction associated with defects — less than 13 percent. Consequently, extensive evaluation of material defects in titanium alloys would not be productive nor cost-effective. In general blades have very high surface area to volume ratios, constant gas-path exposure, and higher vibratory stresses. Accordingly, titanium blade failure origins are most often associated with surface damage such as FOD. Fatigue origins are occasionally associated with manufacturing or handling damage to the surfaces, but only rarely with material defects.

Pratt & Whitney's experience with HCF-related failures in compressor blades clearly shows FOD, rather than initial material defects, to be the primary cause of failure. The photographs in Figure 2 typify this experience, which was most recently illustrated in a review made of F100 engine high-pressure compressor (HPC) blade failures for the period from 1970 to 1982. In this

study, FOD-related damage was the leading cause of failure (among 10 generic failure causes), and such failures occurred 2.5 times more often than initial material defect-related failures. Consistent with this experience, this program addresses defects both in the form of initial material quality and foreign object damage.

Using the Goodman format as a starting point, a methodology can be developed for incorporating the effects of prior damage, intrinsic and extrinsic, into a HCF lifting system. The level of damage can be considered analogous to the fracture mechanics crack size, a . Fracture mechanics also provides the physical and mathematical basis for relating this damage level with the stress field in which the component must operate and survive. The conventional definition of HCF survival is the S-N runout, typically 10^7 cycles. This program will consider another definition: the cyclic life obtained by integrating the material $da/dN = \Delta K$ relationships from ΔK_{th} to ΔK_{IC} as shown in Figure 1.

Following the arguments developed above, this program has focused on quantifying ΔK_{th} and describing the initial damage state for a typical fan/compressor alloy, Ti 8Al-1Mo-1V. That information is incorporated in a fracture mechanics based model for HCF behavior. The specific intent of the model is to produce representative Goodman diagrams based on the threshold and damage level data generated for Ti 8-1-1. However, it is presented as a generic technology which can be used to examine other materials of interest. In addition, conventional Goodman diagrams were generated from HCF specimen testing for comparison purposes.

To accomplish these objectives, the 36-month technical effort was organized into the following five tasks, plus the reports and oral briefings which comprised Task VI:

Task I — Determination of Test Material, involved the material selection and procurement process.

Task II — Threshold Crack Growth Testing, assessed the effects of frequency, stress ratio (R), temperature, and hold time in determining ΔK_{th} . A second test procedure and geometry was examined at Florida Atlantic University during this task.

Task III — Smooth Bar Fatigue Testing, generated data to establish S-N curves, fatigue limits, and conventional Goodman diagrams. Metallographic analysis of failed smooth bar specimens was conducted to assess the influence of IMQ on S-N behavior.

Task IV — Analytical Modeling, developed the algorithms required to convert threshold stress intensity data into Goodman diagrams. This task also included a field hardware survey to quantify FOD.

Task V — Verification Testing, included a series of tests intended to assess the capabilities of the analytical model. It was necessary to modify the content of this task over the course of the program.

Detailed descriptions of the results of these tasks constitute the bulk of this report.

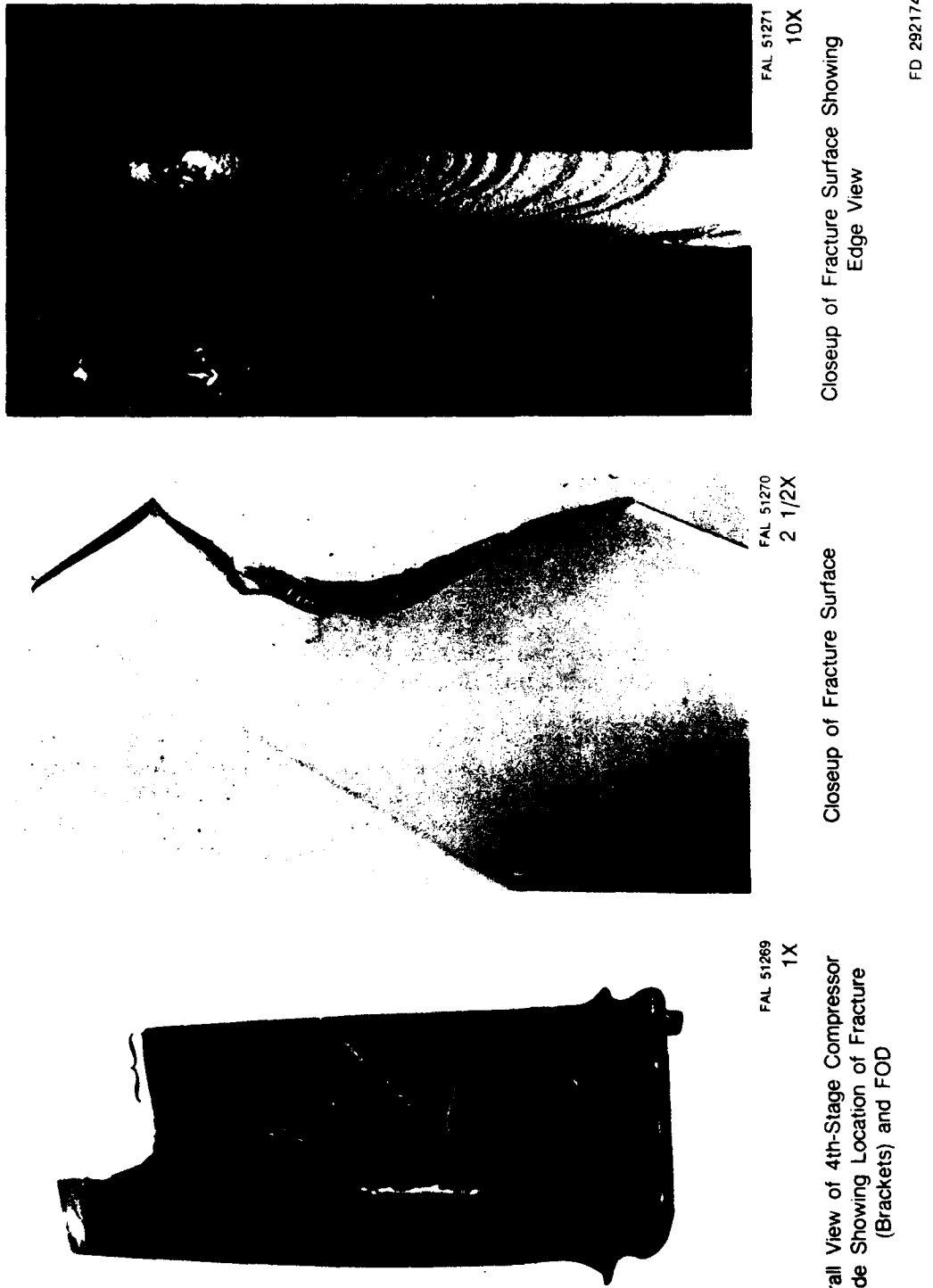


Figure 2. HCF-Related HPC Blade Failure Due to FOD

SECTION II

TASK 1 — MATERIAL SELECTION AND PROCUREMENT

In keeping with the program objectives, this task aimed at selecting an alloy used for fan and compressor blades. Three materials were considered as viable candidates for study: Ti 6Al-4V, Ti-8Al-1Mo-1V, and Ti 6Al-2Sn-4Zr-6Mo. All of these materials are used in either fan or compressor applications, and each had positive and negative attributes as a test material. Ti 8-1-1, heat-treated to PWA 1202 blade specifications, was selected for use in this program, based on the following reasoning:

1. Ti 8-1-1, heat treated to PWA 1202 specifications, has relatively high temperature capabilities (up to 800°F). This is somewhat higher than the Ti 6-4 temperature capabilities.
2. Ti 8-1-1 is used in components, fan and forward compressor stages, which are likely to sustain FOD. This is significant since FOD was considered to be a probable source of blade defects. By comparison, Ti 6-2-4-6 blades are used only in compressor applications.
3. Pratt & Whitney had limited blade failure data available for Ti 8-1-1 components. That data was valuable in identifying fatigue failure origins and fracture modes.
4. Standard crack growth data was available for use in estimating crack growth thresholds, thus facilitating threshold testing.

Approximately 483 cm of 63.5-mm-diameter forged and hot-rolled bar stock was procured from NF&M Corp. That was an adequate amount of material to meet all testing requirements for the program. All the material was from a single heat so as to avoid heat-to-heat variations in test results. This particular material was considered suitable since the majority of the heat had already been purchased by P&W for blade production. The material chemistry as reported by NF&M is given in Table 1.

The bar stock was received in the annealed condition, and was heat treated to PWA 1202 blade specifications. The specific heat treatment used was as follows:

Solution: 927°C + 14°C for one hour — air cool

Age: 580°C + 8°C for eight hours — air cool.

For blade applications, the solution step is conducted in an inert atmosphere to prevent surface oxidation. For the purpose of this program, all specimen surfaces were machined after heat treatment and prior to testing, so the inert atmosphere was not required. Actually, heat treating in air produced only a minimal scale on the surface of the titanium bars.

After heat treating, material specification tests were conducted to ensure that the program material met all PWA 1202 requirements. The results of these tests are given in Table 2. The test material met all specification requirements, except for a minor deviation in stress rupture properties. Since the deviation was small, the material was considered to be acceptable. In addition, all the specification tests were repeated at NF&M with the results being similar to those given in Table 2. The stress rupture tests at NF&M exceeded the specification requirements.

TABLE 1. PWA 1202 Material Chemistry

Element	Chemistry — Wt %			Spec Requirement — Wt %	
	Top	Middle	Bottom	Min	Max
Al	8.2000	8.2000	8.0000	7.30	8.50
V	1.0000	1.0000	1.0000	0.75	1.25
Sn					
Mo	1.0000	1.0000	1.1000	0.75	1.25
Zr					
Cu					
Fe	0.0900	0.0900	0.1000	—	0.30
C	0.0140	0.0170	0.0140	—	0.08
N	0.0050	0.0060	0.0070	—	0.05
O	0.1100	0.1100	0.1100	—	0.12
Mn					
Y	< 0.0010	< 0.1100	< 0.1100	—	0.001
Si	< 0.0300	< 0.0300	< 0.0300	—	0.01
B	< 0.0030	< 0.0030	< 0.0030	—	0.003
Ti				Remainder	
	Edge	M.R.	Center		
H (ppm):	110	50	34	—	150

R20431/1

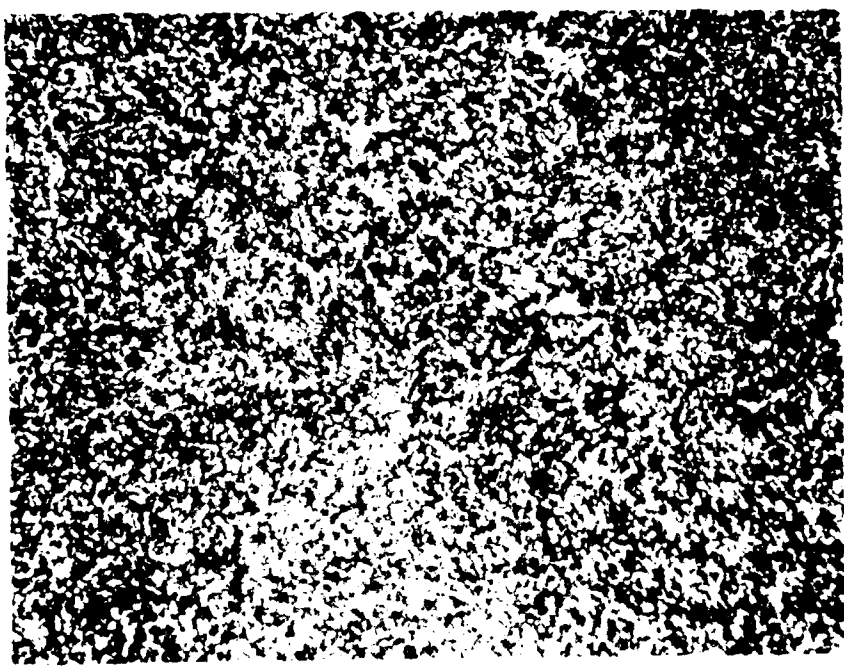
TABLE 2. Mechanical Property Specification Test

Property		Test Result (Average)	Spec Requirement (min.)
Tensile Strength	27°C	1011 MPa	896 MPa
	427°C	717 MPa	621 MPa
2% Offset Yield Strength	27°C	985 MPa	827 MPa
	427°C	596 MPa	483 MPa
Elongation	27°C	16.7%	10%
	427°C	22.3%	10%
Reduction in Area	27°C	32.1%	20%
	427°C	51.7%	25%
Stress Rupture	27°C	10 hrs (Tests Discontinued)	5 hrs
	896 MPa		
Hardness		30.8 HRC	<39 HRC

R20431/1

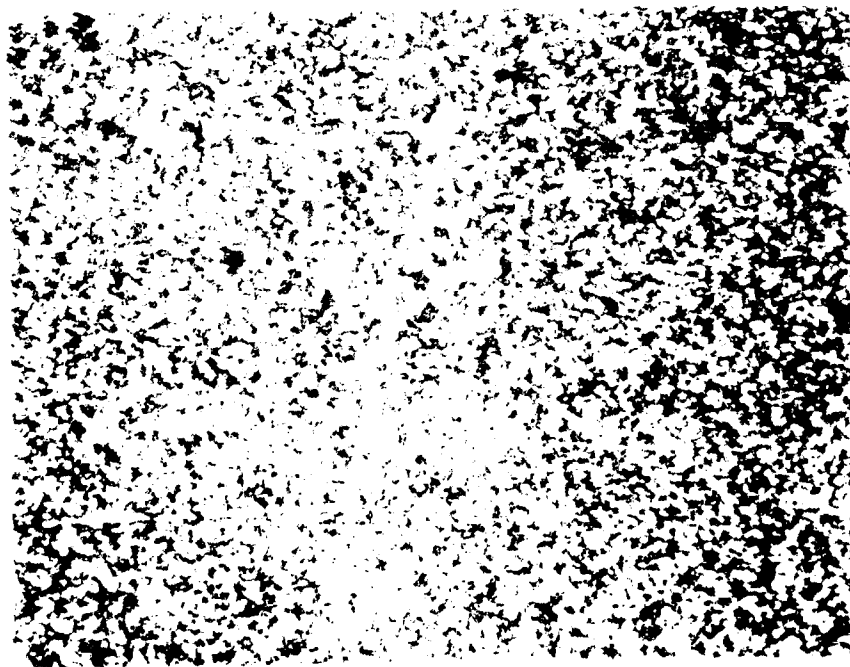
Typical microstructures of the heat treated material in the transverse and longitudinal directions are given in Figures 3 and 4, respectively. These microstructures are typical of PWA 1202. As would be expected, the structure shows a slight elongation in the longitudinal direction, i.e., the bar rolling direction. All specification testing was done in the transverse direction, which was the orientation of the test specimens.

In the interest of effective material utilization, all threshold crack growth specimens were machined so that the cracks propagated in the same orientation and direction. (Crack orientation is a concern, since the material is slightly directional.) To accomplish this, specimens were machined as shown in Figure 5. Using that configuration, both the compact type (CT) and the threshold specimens have cracks oriented in the L — R direction, i.e., crack plane perpendicular to the longitudinal axis of the bar, and crack propagation in the radial direction. Smooth bar HCF specimens were oriented in essentially the same direction as the threshold specimens, with the long axis of the specimen parallel to the longitudinal axis of the bar stock. That resulted in crack initiations with the same orientations, L — R, as the crack growth specimens. Orienting the test specimens in this manner eliminated concerns over material directionality.



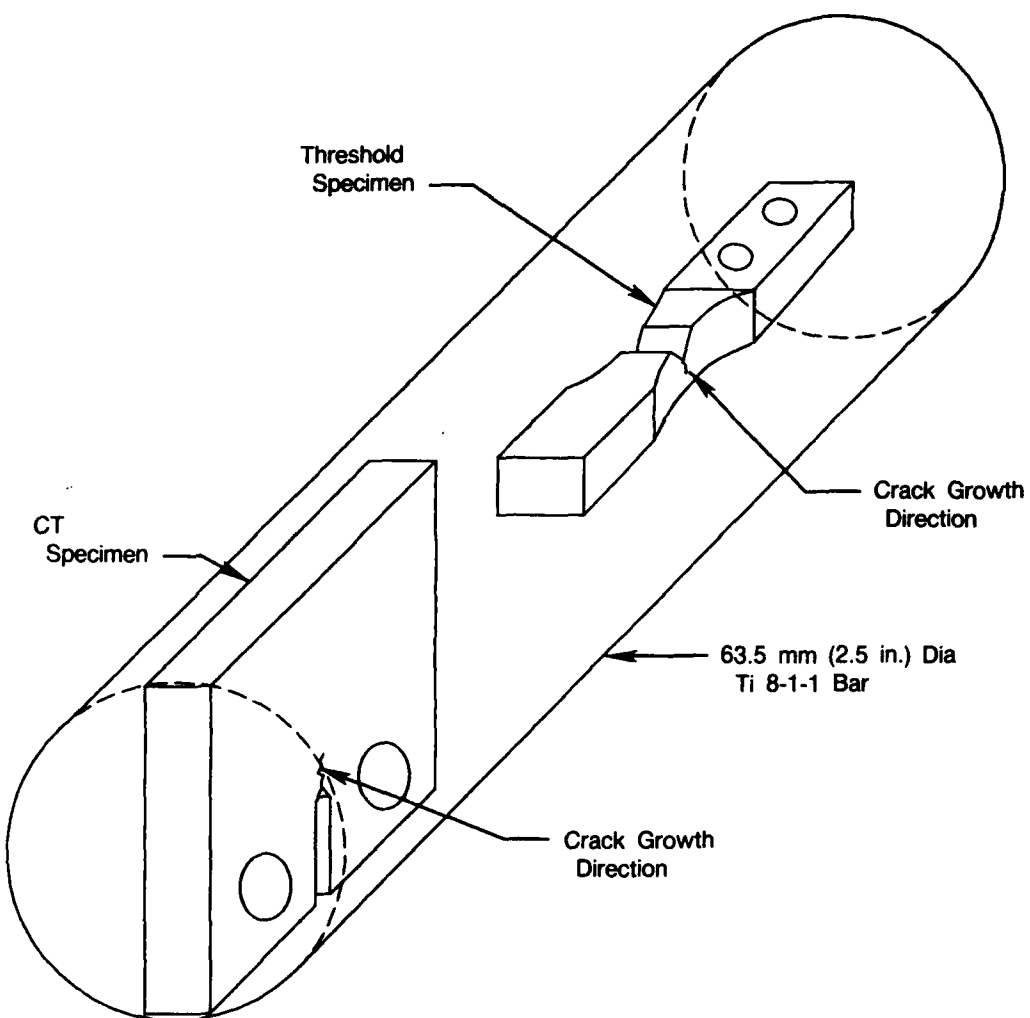
FD 317405

Figure 3. PWA 1202, Transverse Microstructure (100X, Kroll's Etch)



FD 317406

Figure 4. PWA 1202, Longitudinal Microstructure (100X, Kroll's Etch)



FDA 304535

Figure 5. Crack Orientation for Threshold Crack Growth Specimens

A final material consideration was the generation of defects. A review of field and laboratory failures indicated that the vast majority of blade failures are initiated at the surface and are most often associated with surface anomalies, usually FOD, as opposed to intrinsic material defects. Thus, it was determined that the artificially induced material damage to be studied would represent worst case FOD. This damage consisted of sharp surface marks of a controlled depth, produced by a shear cutting method to minimize compressive residual stresses at the notch root. The defects produced in this manner are documented in later sections.

SECTION III

TASK II — THRESHOLD CRACK GROWTH BEHAVIOR

The purpose of this task was to establish an experimental threshold crack growth data base. That information was used to assess the effects of temperature, frequency, and stress ratio on ΔK_{th} . Time dependent effects were also examined to some degree. To gain insight into the uniqueness of ΔK_{th} , an alternate specimen geometry and test technique were used at a separate laboratory. The overall test matrix included two temperatures, two frequencies, four stress ratios, one hold-time incorporated in a high frequency test, two specimen geometries, and two test procedures. Over 90 specimens were tested at 17 sets of test conditions to accomplish the goals of this task.

TEST SPECIMEN AND PROCEDURE

a. Increasing ΔK Threshold Testing

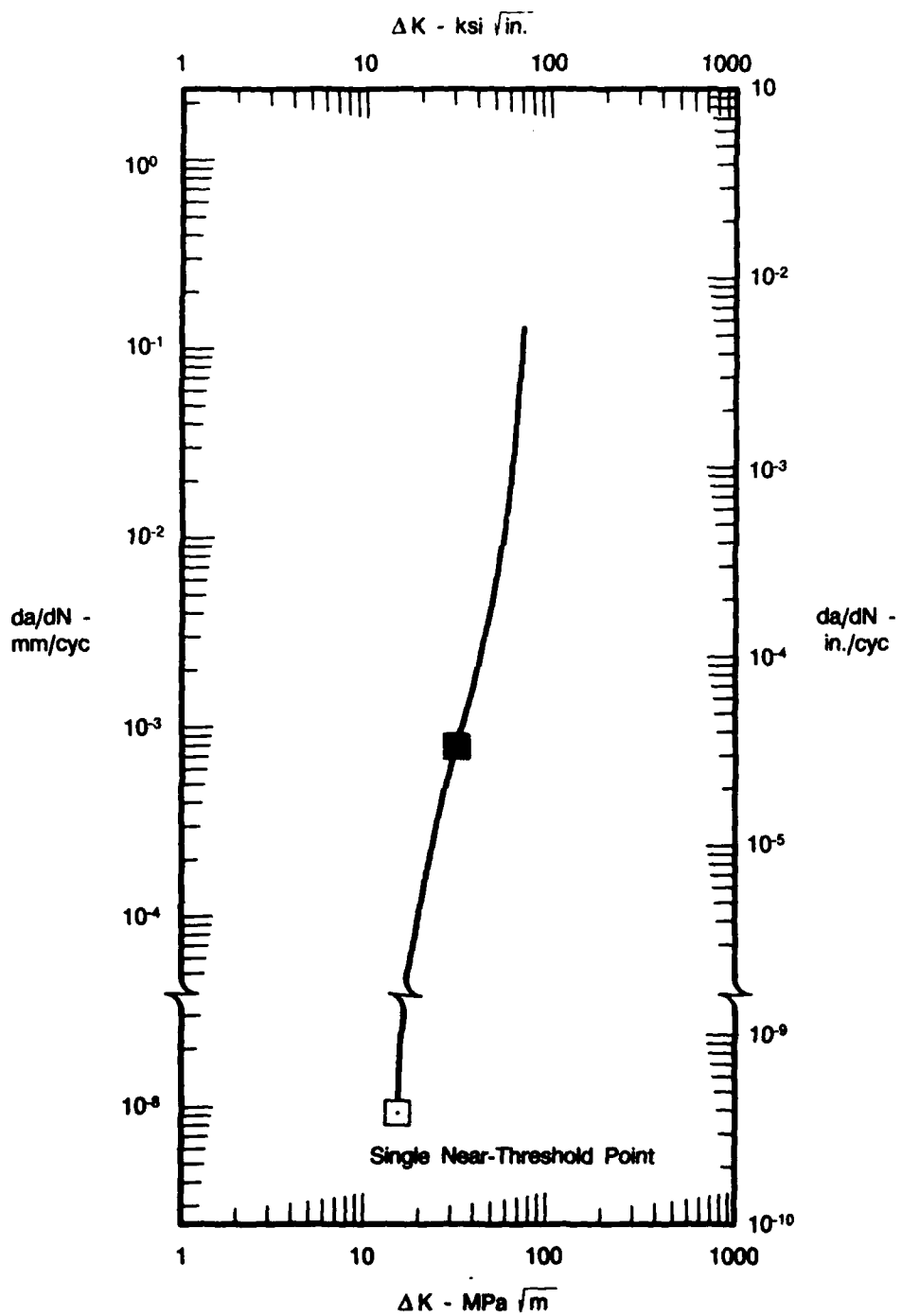
Currently, the load shedding technique defined by ASTM Standard Practice E-647 is probably the most widely used method for determining crack growth threshold stress intensity (ΔK_{th}), but it is very time consuming and expensive. As an alternative, P&W's near-threshold testing method can be less costly and less time consuming, plus it avoids one of the main criticisms of the load shedding method: it identifies the value of ΔK_{th} with the initiation of crack growth from an inactive crack rather than the cessation of growth from an active crack.

The basic idea of P&W's near-threshold test is to define the crack growth rates in the near threshold region with a single point, as illustrated in Figure 6. The technique uses a simple cantilever bend specimen, shown in Figures 7 and 8. Typical specimens for each stage of threshold testing are included in Figure 8. Progressing from top to bottom, the figure includes: a specimen prepared for precracking with the notch intact, a precracked specimen with the notch removed, and a specimen which has failed during testing.

In general, the final test configuration is a through thickness crack, similar to a single edge notch, of 0.3-0.4 mm depth.

Crack lengths are usually measured optically on the surface of the specimen using a traveling microscope at 10-30 \times magnification. In some instances, acetate replication is required to obtain accurate crack length measurements.

A special procedure is used to precrack notched test specimens to avoid possible retardation during subsequent tensile bending cyclic testing. As shown in Figure 9, this procedure first subjects the initial specimen configuration to a compressive load capable of imparting a residual tensile stress at the notch (Figure 9b). Figure 9c shows that by subsequently precracking the specimen using cyclic compression loading, there are no net tensile stresses except the residual stress existing at the notch. Therefore, the subsequent compressive cycling initiates a crack which only propagates to a depth $a_{compressive}$, and then stops. The specimen surface containing the notch is then machined away until the crack remaining has the desired dimensions, after which polishing is used to ensure a stress-free surface.



FDA 358618

Figure 6. Typical da/dN vs ΔK Curve Illustrating Near Threshold Point

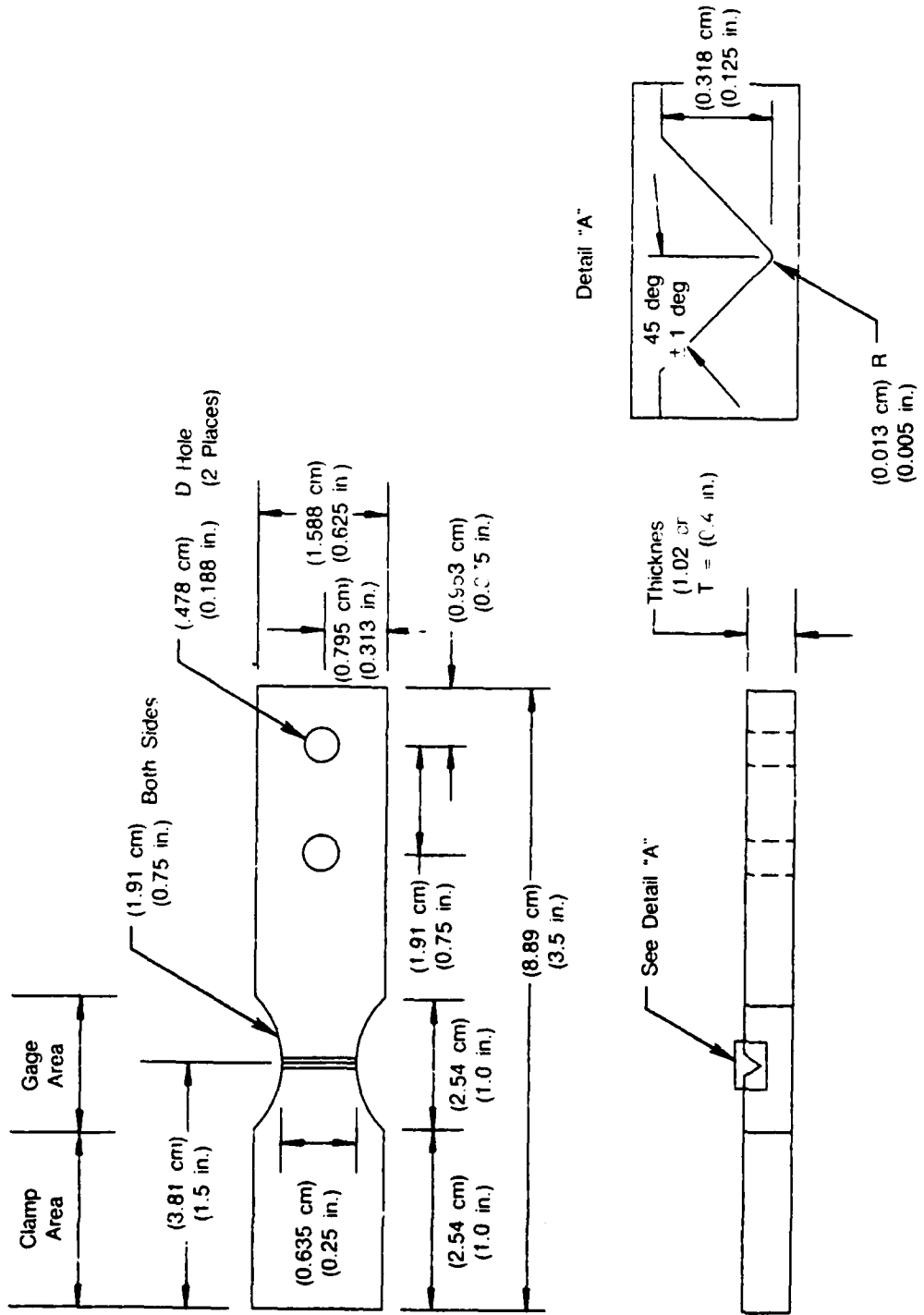
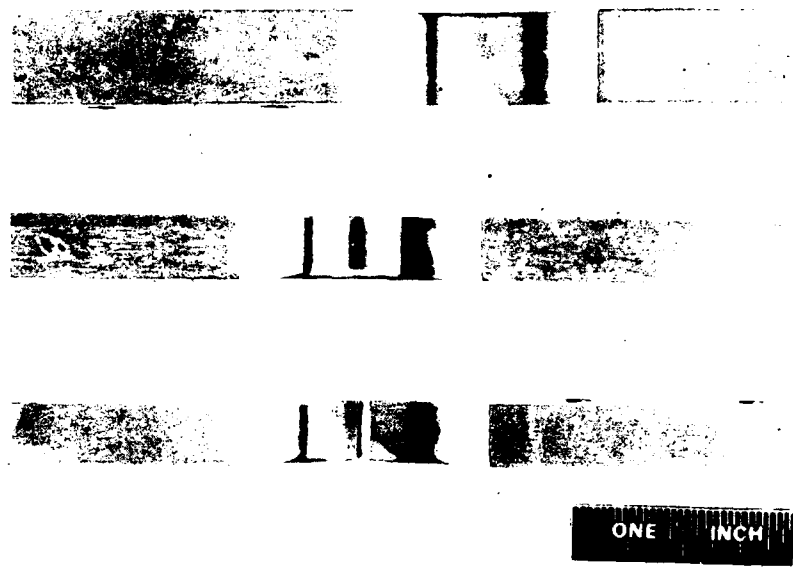


Figure 7. Fatigue Crack Growth Threshold Specimen Configuration

FD 299901

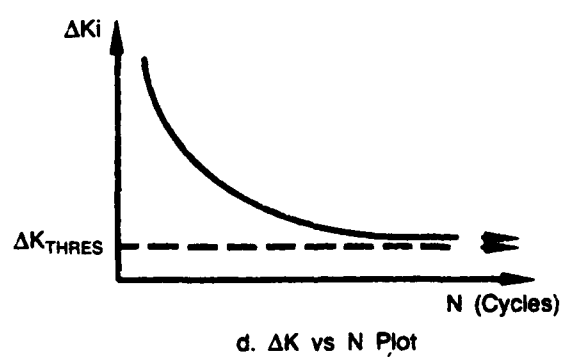
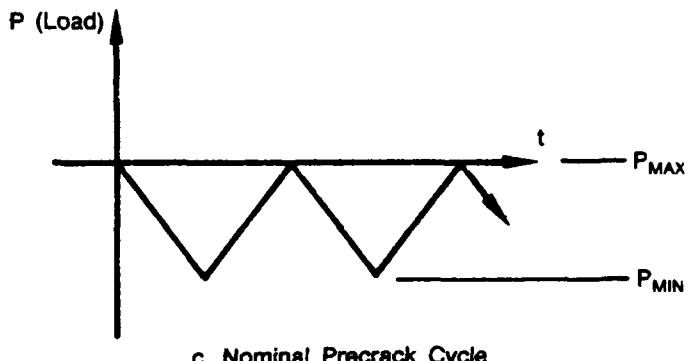
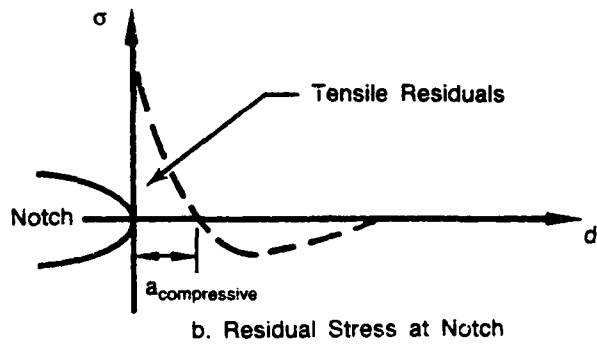
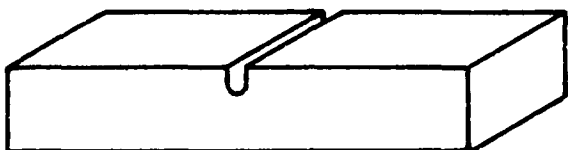


FE 256879

Figure 8. Typical Threshold Specimens

In performing the near-threshold tests using the precracked specimens, several tests are used, changing values of ΔK_i until a threshold value can be found. Commonly, the first value of ΔK_i is selected by extrapolating a mathematical model (sinh curve) of the Region II crack growth behavior into the threshold region. Each precracked specimen is cycled in tensile bending at the selected value of ΔK_i . If the specimen survives 10^7 cycles, its precrack is inspected for growth. If no growth is detected, the corresponding ΔK_i value is assumed to be below or near the threshold stress intensity, and an increased ΔK_i is used for the next specimen. No growth corresponds to an average crack growth rate of about 3×10^{-9} mm/cycle since crack growth of 0.03 mm can be distinguished, i.e., 0.03 mm/ 10^7 cycles. Once growth is detected, sufficient additional tests are conducted to verify the near threshold behavior and the corresponding value of ΔK_{th} . Typically, five near-threshold tests are needed to define ΔK_{th} . The resulting relationship between ΔK_i and ΔK_{th} is shown schematically in Figure 9d.

A fracture surface from a failed specimen is shown in Figure 10. The precrack area is slightly darker than the remainder of the fracture surface. Note that the precrack is not perfectly straight across the thickness of the specimen. Typically, the precrack depth varies by approximately 0.025 to 0.050 mm across the width of the specimen. Although the differences in crack depth are small, they can affect the stress intensity calculations in the threshold region. To avoid error in stress intensity calculations due to uneven crack fronts, all crack lengths are remeasured on the fracture surface after failure. Five crack length measurements are made across the crack front, as shown in Figure 11, and the average of those measurements is used for the final K calculations.



FD 217018

Figure 9. Near-Threshold Crack Growth Test

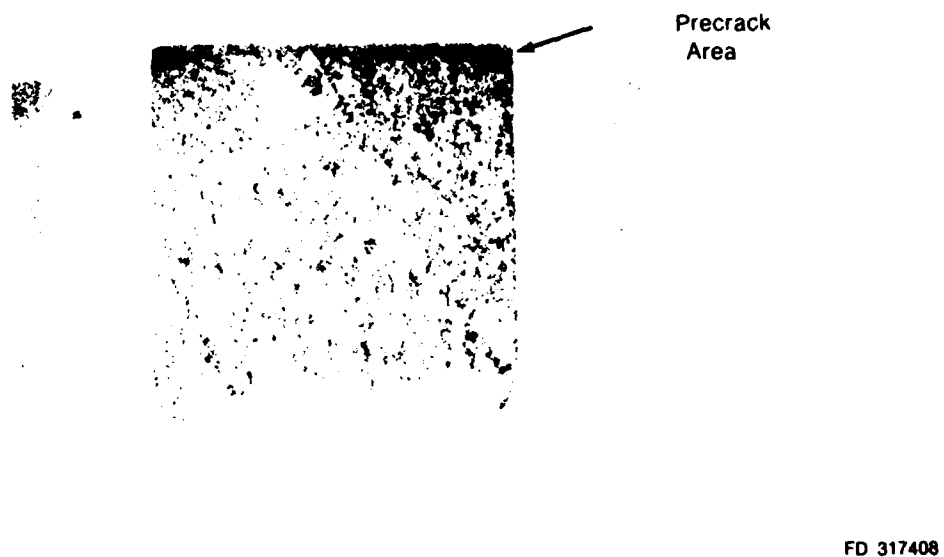


Figure 10. Typical Threshold Crack Growth Specimen Fracture Surface

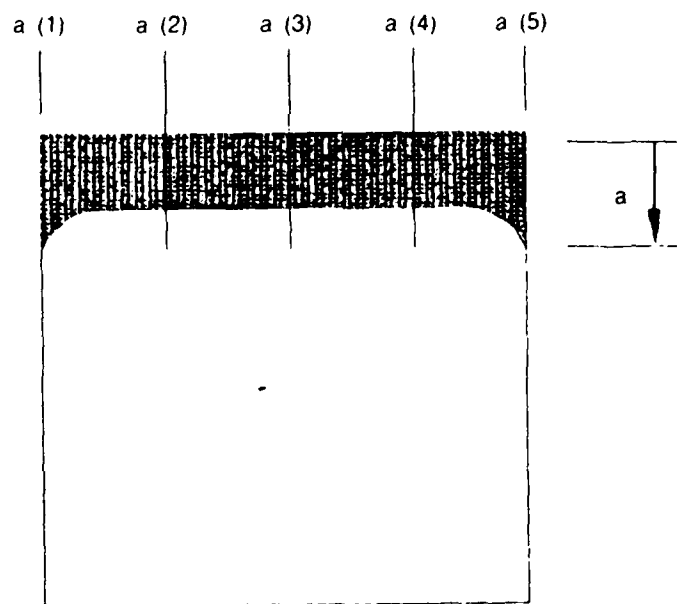


Figure 11. Average Crack Length Measurements

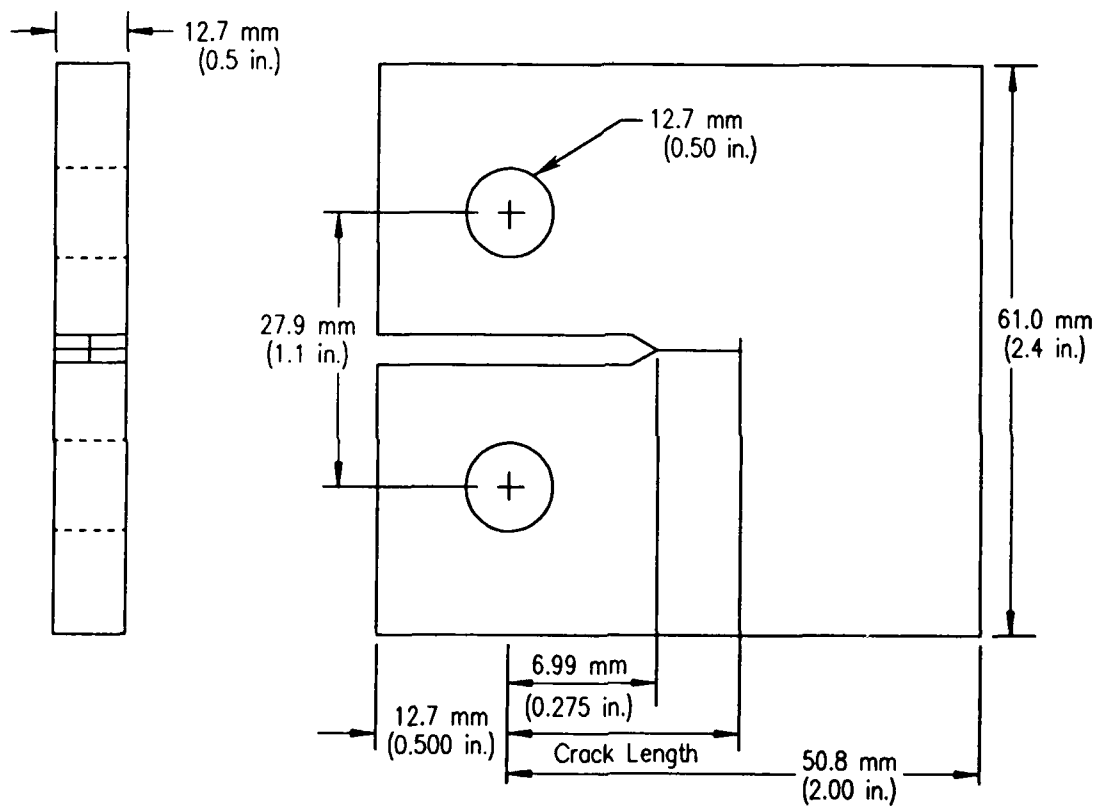
Threshold testing is performed in cyclic bending, using a motor-driven offset cam machine running at 30 Hz. For higher frequency testing, 200 Hz in this case, the testing is conducted on an electrodynamic shaker rig.

Heating for the elevated temperature tests is supplied by clamshell electrical resistance furnaces which completely enclose the specimen. Temperature is monitored using thermocouples attached to the specimen gage section and is controlled digitally to within $\pm 3^{\circ}\text{C}$.

b. Decreasing ΔK Threshold Testing

An alternate fatigue crack growth threshold test method was employed to provide data for comparison with the data obtained from the test procedures previously described. This method is based on ASTM Standard Practice E-647-88, "Measurement of Fatigue Crack Growth Rates." (Ref. 3).

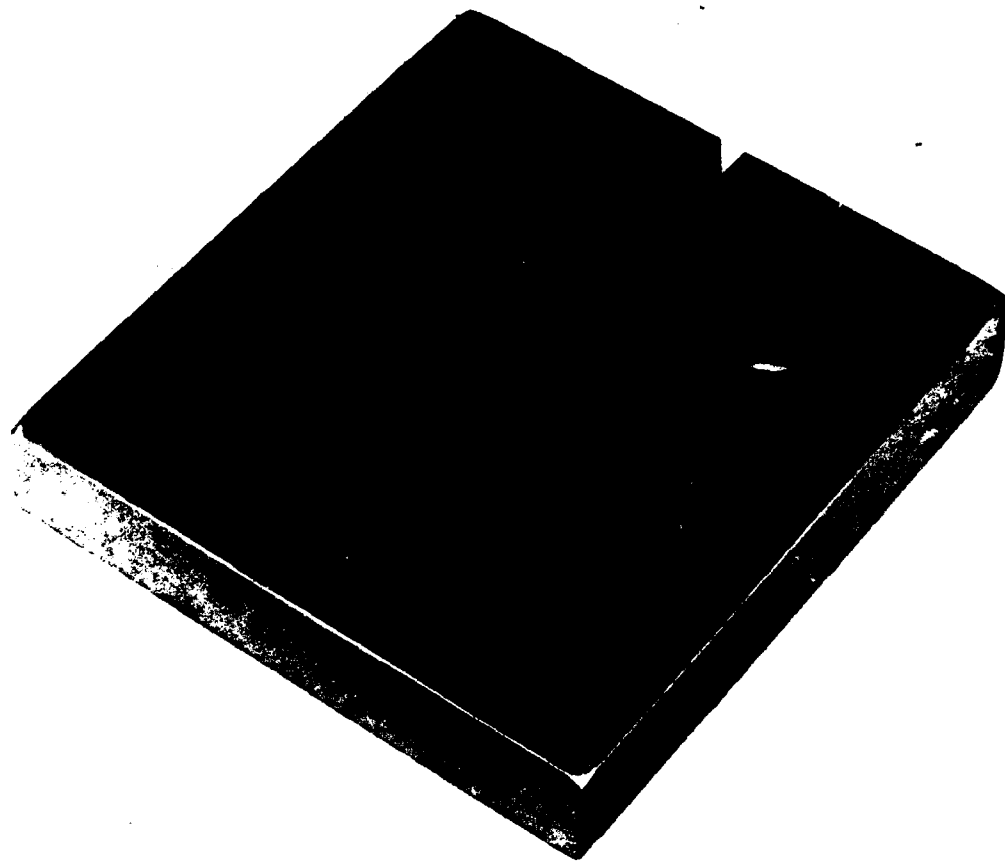
The specimen used in these tests was a standard compact type (CT) specimen defined in ASTM E-647. The specific geometry used is shown in Figures 12 and 13. Standard stress intensity solutions, size restrictions, and crack front curvature limitations are applicable. The initial specimen preparation and precracking procedures used were the same as those employed in standard crack growth rate testing.



FD 292178

Figure 12. Compact Specimen for Alternate Testing Method

The test consists of applying a decreasing stress intensity (K) gradient to the specimen to back down the da/dN , ΔK curve and approach the fatigue crack growth threshold (ΔK_{th}). This is accomplished by decreasing the test load (load shedding) as the crack extends. The test is started by cycling at a ΔK and K_{max} level equal to or greater than the final level used during precracking. The load shedding can then be performed on a continuous basis under computer control. Care must be exercised in the selection of the rate of load shedding to ensure that the decrease in load does not result in retardation of the crack growth rates. This would introduce error into the calculated crack growth rate behavior, which would result in an error in the determination of the fatigue crack growth threshold stress intensity, ΔK_{th} .



FAE 224398

Figure 13. Typical Compact-Type (CT) Specimen

The load shedding schedule used is developed in Reference 4:

$$\Delta K = \Delta K_0 \exp^{C(a - a_0)} \quad (1)$$

where the zero subscript indicates the initial values of the test and C is a constant which determines the rate of decrease of stress intensity range (load). This expression was derived by noting that in a K-decreasing test the monotonic plastic zone size should decrease. It was then assumed that the change in plastic zone size remains constant with increasing crack length. The constant C is defined as:

$$C = \frac{1}{K} \frac{dK}{da} \quad (2)$$

which is the normalized K-gradient. The value of C that is chosen depends on the material, the load ratio, R, and the environment. C also should be chosen to obtain five da/dN, ΔK pairs of approximately equal spacing per decade of crack growth rate. In this program C values of -0.08 mm^{-1} (-2.0 in.^{-1}) and -0.06 mm^{-1} (-1.5 in.^{-1}) were used.

Under computer control, the load is automatically decreased to reduce the stress intensity range, ΔK . The specimen compliance is monitored and used to provide an indication of crack

length. The computer calculates the value of stress intensity range associated with this crack length and adjusts the load to reduce ΔK according to equation (1). Several visual crack length measurements are taken over the course of the test to confirm and calibrate the compliance measurements. The specimen compliance is determined from load vs crack-mouth-opening-displacement records, as described in Appendix A.

Load shedding is continued until a minimum of five da/dN , ΔK pairs of approximately equal spacing are obtained between crack growth rates of 10^{-9} and 10^{-10} m/cycle. Linear regression is then used to obtain the best-fit line to the data in this region. The regressed line is used to calculate the ΔK value that corresponds to a crack growth rate of 10^{-10} m/cycle. This value of ΔK is used as the operational definition of fatigue crack growth threshold, ΔK_{th} .

To check the validity of the data obtained from the K-decreasing tests, a K-increasing test was performed on one specimen after a determination of ΔK_{th} was made by the K-decreasing procedure. The data from the two methods should correspond, indicating that retardation effects are not present in the data obtained from the K-decreasing method and that the value of C chosen provides a valid test for the determination of ΔK_{th} .

Another factor which must be taken into consideration is crack closure. It is generally accepted that under some combinations of environment, geometry, and loading, a crack will remain closed during some portion of the fatigue cycle. This crack closure phenomenon is commonly observed, even for tension-tension cycles. Little or no additional damage accumulates at the crack tip during that portion of the cycle when the crack is closed. Thus the applied stress intensity range, ΔK , is reduced to an effective stress intensity range, ΔK_{eff} , as shown in Figure 14. After Figure 14,

$$\Delta K = K_{max} - K_{min}$$

and,

$$\Delta K_{eff} = K_{max} - K_{cl},$$

where, K_{cl} corresponds to the load level at which the crack closes.

Three general closure mechanisms are commonly recognized; oxide-induced, roughness-induced, and plasticity-induced closure. Those closure mechanisms are shown schematically in Figure 15. Oxide-induced closure can be explained simply. When an oxide layer or oxide debris is formed at the crack tip and reaches a thickness on the order of the crack-tip-opening-displacement, it can serve to prop the crack open at a load above the minimum. The effective stress intensity range is reduced accordingly. Roughness-induced closure occurs by a similar mechanism. Crack surface asperities combined with the minor Mode II (sliding) displacements intrinsic to Mode I crack opening can cause the crack to close before the minimum load is reached. Again, this mechanism is significant only when the scale of roughness is comparable to the crack-tip-opening-displacement. Plasticity-induced closure is related to the plastic deformation occurring at the crack tip. As the crack extends, the residual deformation from the plastic zone ahead of the crack produces a plastic wake along the flanks of the crack. Since the undeformed elastic material surrounding the crack restrains expansion in other directions, the majority of the residual deformation occurs perpendicular to the crack surface. As the crack closes, this expanded material comes into contact before the minimum load is reached, thus reducing the effective ΔK . Although these mechanisms differ considerably, they all have the effect of reducing the effective stress intensity range, thereby decreasing the observed crack growth rates. Crack closure information was recorded for all tests conducted on the CT geometry. That information was used in comparisons of test method dependence. All of this decreasing ΔK

threshold testing was performed at Florida Atlantic University (FAU), under the direction of Dr. G. C. Salivar. The test system and detail procedures used at FAU are described in Appendix A.

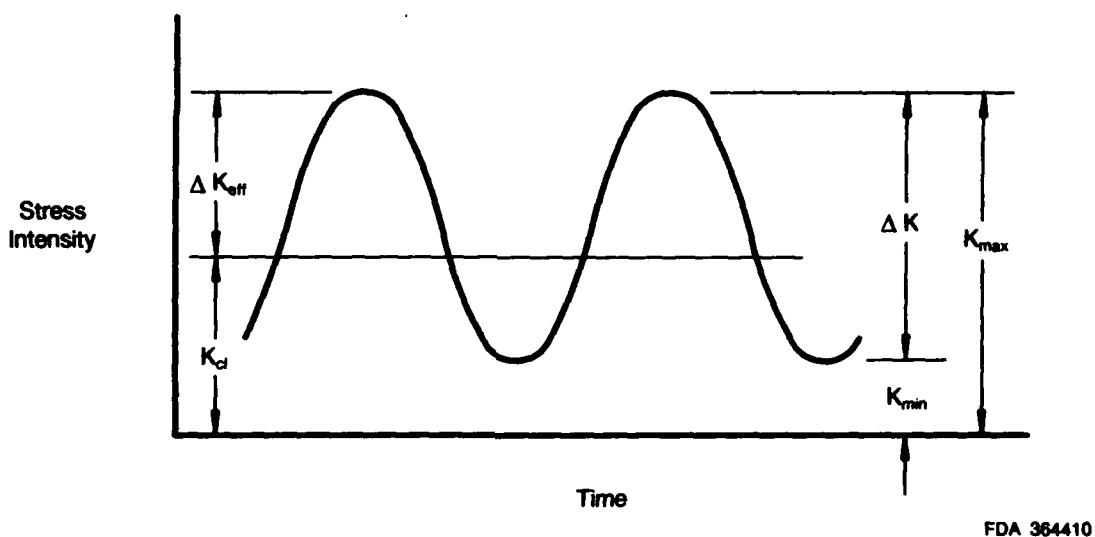
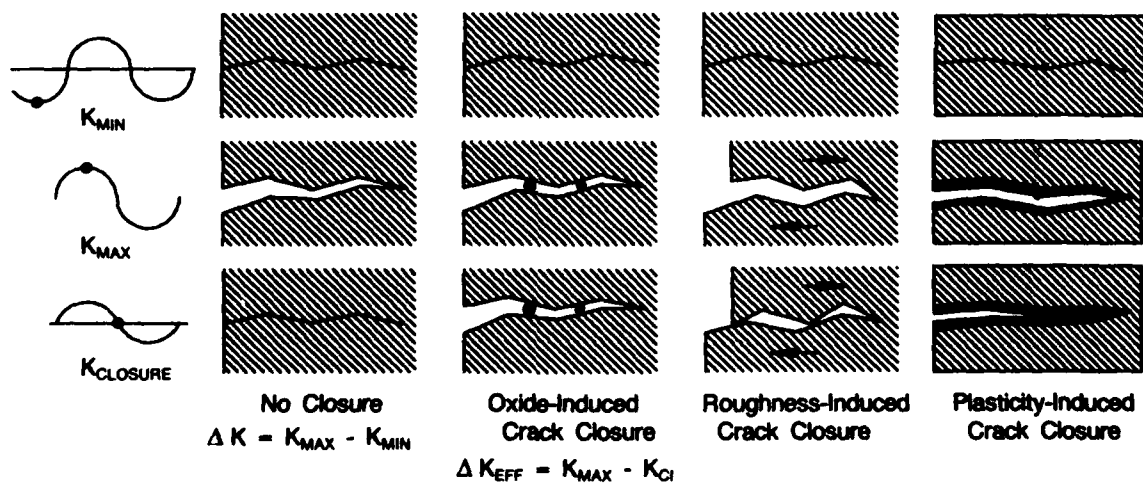


Figure 14. Effect of Closure on Stress Intensity Range



FDA 364411

Figure 15. Commonly Recognized Closure Mechanisms

RESULTS

The results of the threshold crack growth testing performed using the K-increasing bend specimen are summarized in Table 3. The ΔK_{th} results are presented as a range of values representing the highest test ΔK which did not fail, to the lowest test ΔK which caused failure. Typically, enough tests were conducted to produce a ΔK_{th} range which was less than or equal to

0.55 MPa \sqrt{m} . A listing of all tests required to generate this ΔK_{th} information is included in Appendix B.

TABLE 3. ΔK_{th} Test Results

Test Conditions			ΔK_{th} (MPa \sqrt{m})		
Temperature °C	Frequency (Hz)	Stress Ratio (R)		(Did not fail)	(Failed)
27	30	-1.0	2.1	-	2.5
		0.1	2.5	-	2.9
		0.5	2.0	-	2.5
		0.7	2.2	-	2.6
260	30	-1.0	2.1	-	2.4
		0.1	2.2	-	2.2
		0.5	1.9	-	2.2
		0.7	1.3	-	1.6
27	200	0.5	2.3	-	2.9
260	200	-1.0	1.5	-	1.8
		0.1	1.9	-	2.0
		0.5	2.3	-	2.5
		0.7	1.5	-	1.6
260	200 Hz/ 2 min dwell	0.5	2.0	-	2.1
		0.7	2.5	-	2.6

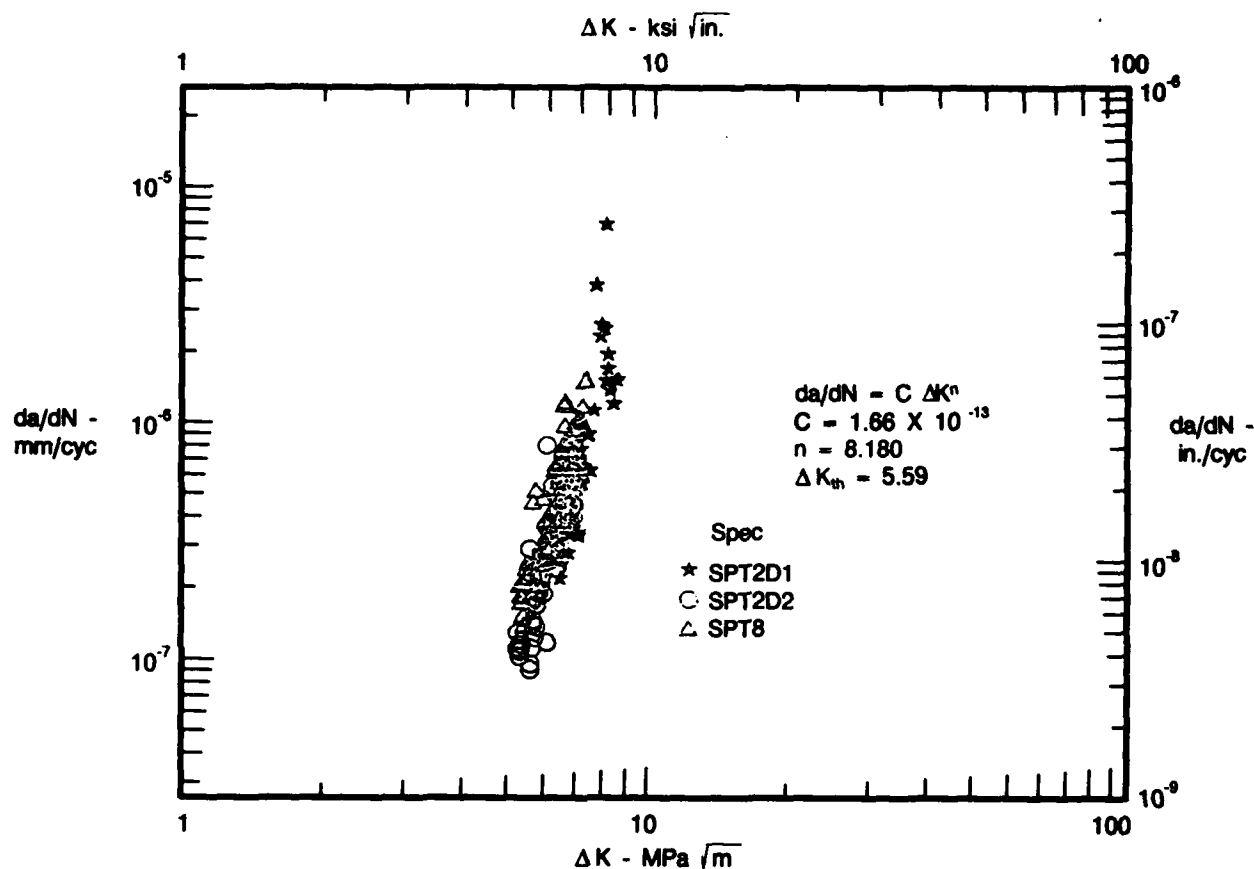
R20431/1

Results of the K-decreasing tests conducted at FAU using CT specimens are summarized in Table 4. Also included in that table are closure corrected values of threshold stress intensity, $\Delta K_{th, eff}$, and ΔK_{th} values for the relevant conditions from the K-increasing tests. Crack growth rate data obtained from the K-decreasing tests are given in Figures 16 through 19. Included in those figures are the Paris coefficients used to establish specific ΔK_{th} values. The Paris lines shown were determined by linear regression of the data between 1.0×10^{-9} and 1.0×10^{-10} m/cycle. The ΔK_{th} values are calculated from the Paris relationship at 1.0×10^{-10} m/cycle. A listing of CT tests and test conditions are given in Appendix B.

TABLE 4. ΔK_{th} Comparison

Temperature (°C)	Frequency (Hz)	Stress Ratio (R)	K-increasing		K-decreasing	
			ΔK_{th} (MPa \sqrt{m})	ΔK_{th} (MPa \sqrt{m})	$\Delta K_{th, eff}$ (MPa \sqrt{m})	$\Delta K_{th, eff}$ (MPa \sqrt{m})
27	20/30	0.1	2.5 - 2.9	5.6	2.5	2.5
260	20/30	0.1	2.2 - 2.2	5.2	2.9	2.9
260	20/30	0.5	1.9 - 2.2	3.5	3.1	3.1
260	20/30	0.7	1.3 - 1.6	2.6	2.6	2.6

R20431/1



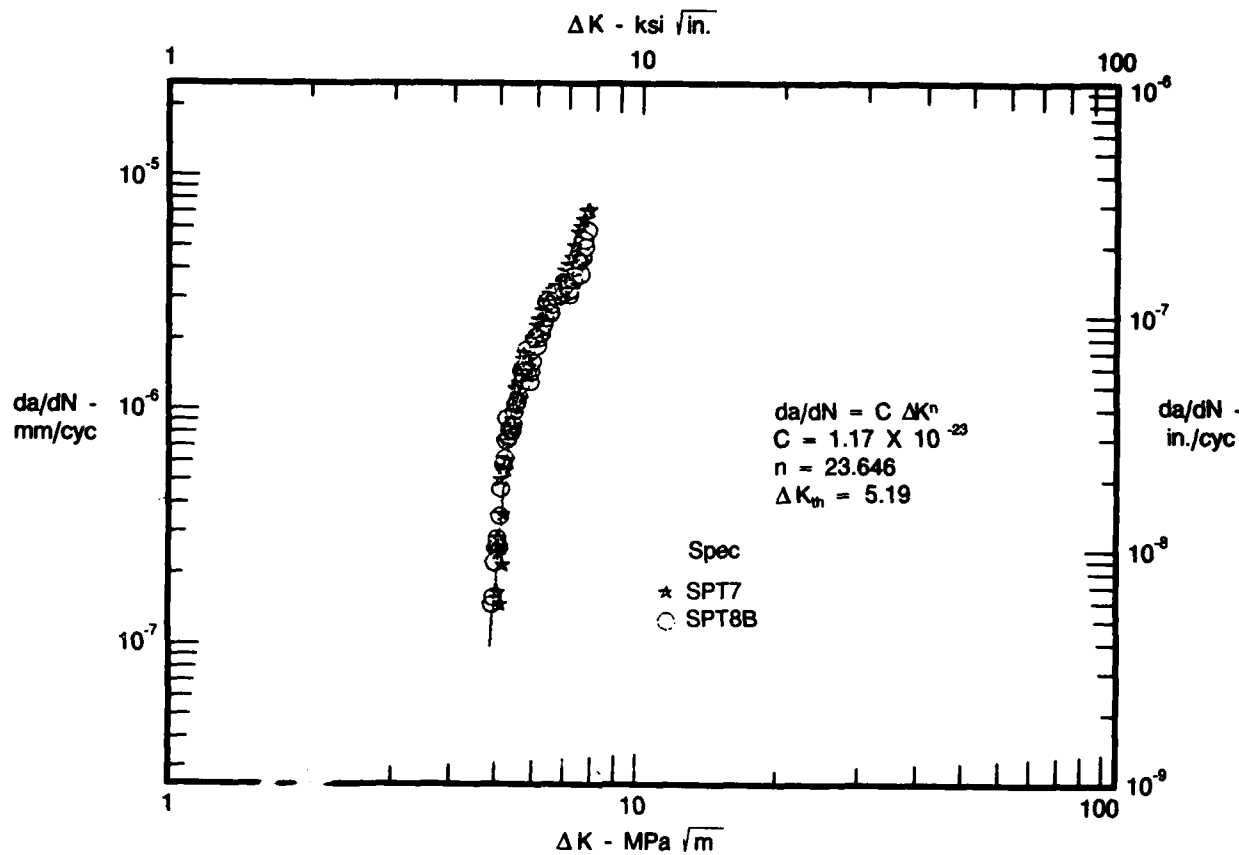
FD 356601

Figure 16. PWA 1202 Near-Threshold Fatigue Crack Growth Rates, 27°C, R=0.1, 20 Hz

Constant-load tests were also conducted with the CT geometry to confirm the K-decreasing tests. The results of the constant-load, i.e., K-increasing, tests are compared to the K-decreasing tests in Figures 20 through 23. (Also included in those figures is closure-corrected data which will be discussed in later sections.) These data were obtained by changing to a load-controlled cycle at a slightly increased K-level directly following the completion of a K-decreasing threshold test. Review of these data shows good correlation with the K-decreasing data. This confirms the validity of the K-decreasing technique, particularly the choice of values for C, the constant in equation (2) which determines the rate of decrease in K.

Stress Ratio Effect

The effect of stress ratio (R) was of particular interest in this program, mainly due to the strong stress ratio trends exhibited by HCF Goodman diagrams. Considerable information is also available in the literature demonstrating a strong effect of stress ratio on ΔK_{th} (References 10, 11, 13, and 17). As indicated by Tables 3 and 4, stress ratio was the major variable in the matrix. The aim of that testing was to quantify the effect of R on ΔK_{th} , so it could be used in fracture-based HCF models.



FD 356602

Figure 17. PWA 1202 Near-Threshold Fatigue Crack Growth Rates, 260°C, R=0.1, 20 Hz

Review of the data in Table 3 indicates that there is no obvious trend in the ΔK_{th} data with respect to stress ratio. A weak trend toward decreasing ΔK_{th} with increasing stress ratio is indicated by the 260°C data at 30 Hz and by comparing large changes in stress ratio (R = 0.1 to 0.7) at the other test conditions. This trend can be expanded to a model. However, the veracity of such a model is questionable since the size of the effects being modeled are not greatly different than the apparent degree of data scatter and the potential experimental error.

The effect of stress ratio in the K-decreasing tests can be seen in Table 4. Those data indicate a substantial effect of R on ΔK_{th} , with ΔK_{th} increasing with decreasing R. However, the magnitude of ΔK_{th} measured in this fashion does not agree with the K-increasing values of ΔK_{th} . $\Delta K_{th,eff}$ values are in much closer agreement with the K-increasing values of ΔK_{th} . $\Delta K_{th,eff}$ is virtually constant with changing R, and is also in rough agreement with the K-increasing data. The effects of R on K-increasing and K-decreasing values of ΔK_{th} and $\Delta K_{th,eff}$ are compared in Figure 24. Further, varying magnitudes of change in ΔK_{th} and little or no change in $\Delta K_{th,eff}$ with respect to stress ratio, appear to be the predominant trends identified in the literature (References 5, 10, 11, and 15). Thus, if consistent threshold stress intensities are to be produced using different test specimens or procedures, the evidence points away from attempting to define a specific stress ratio effect on threshold stress intensity. Comparing closure corrected values would seem to be a more viable solution, but that approach entails its own difficulties. This position generates a serious problem in converting ΔK_{th} data to a fracture-based Goodman Diagram. That problem is addressed in the analytical modeling section.

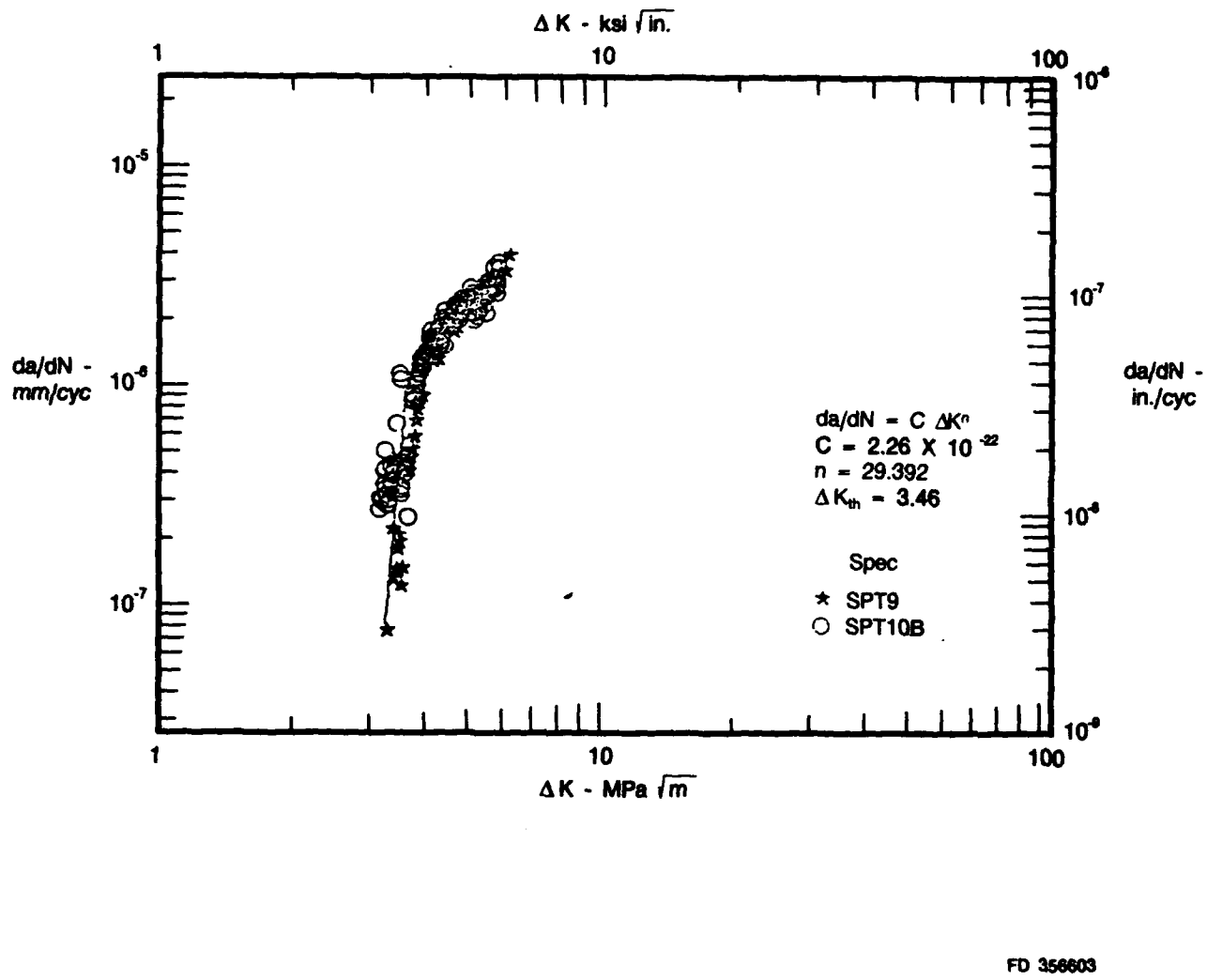


Figure 18. PWA 1202 Near-Threshold Fatigue Crack Growth Rates, 260°C, $R=0.5$, 20 Hz

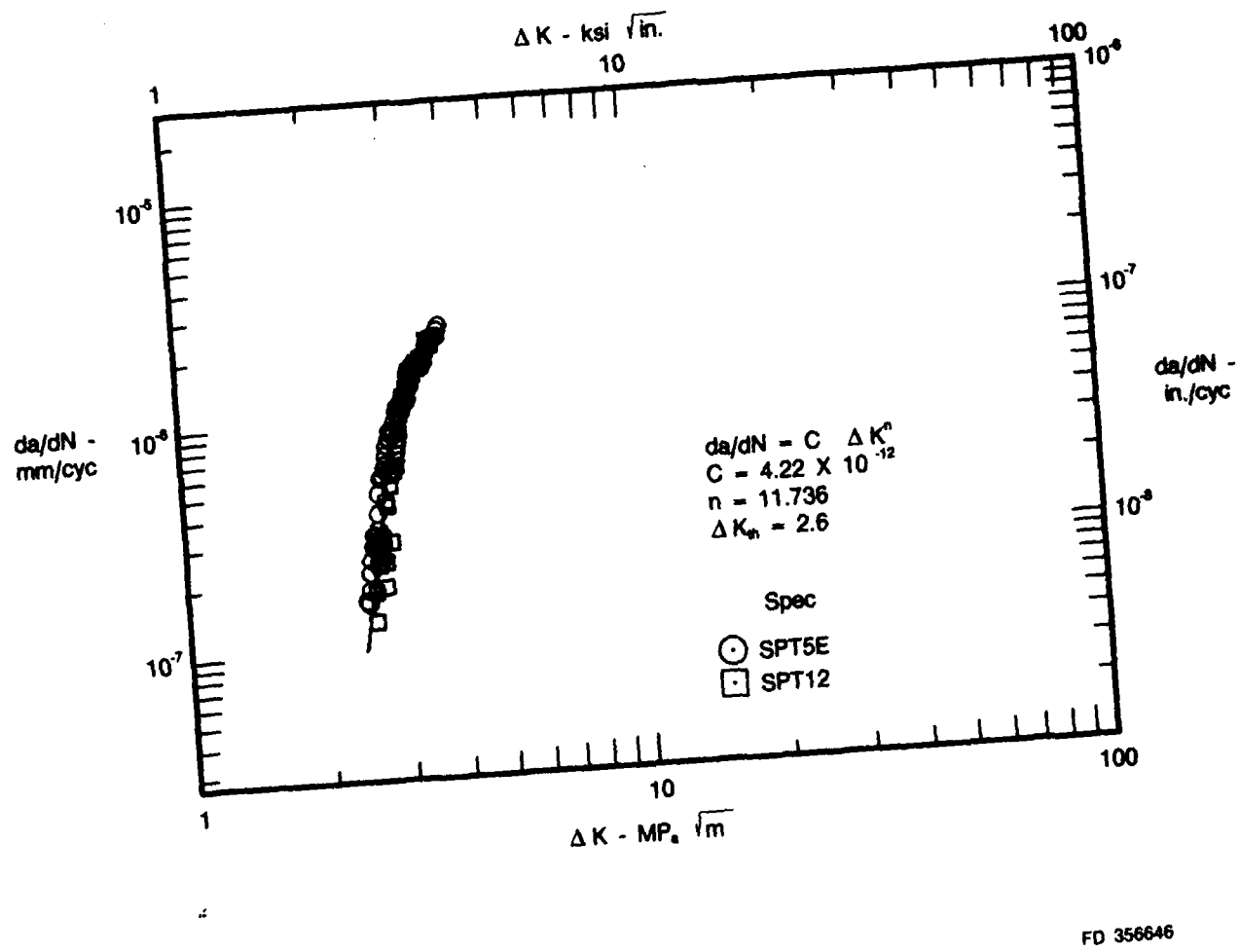


Figure 19. PWA 1202 Near-Threshold Fatigue Crack Growth Rates, 260°C, R=0.7, 20 Hz

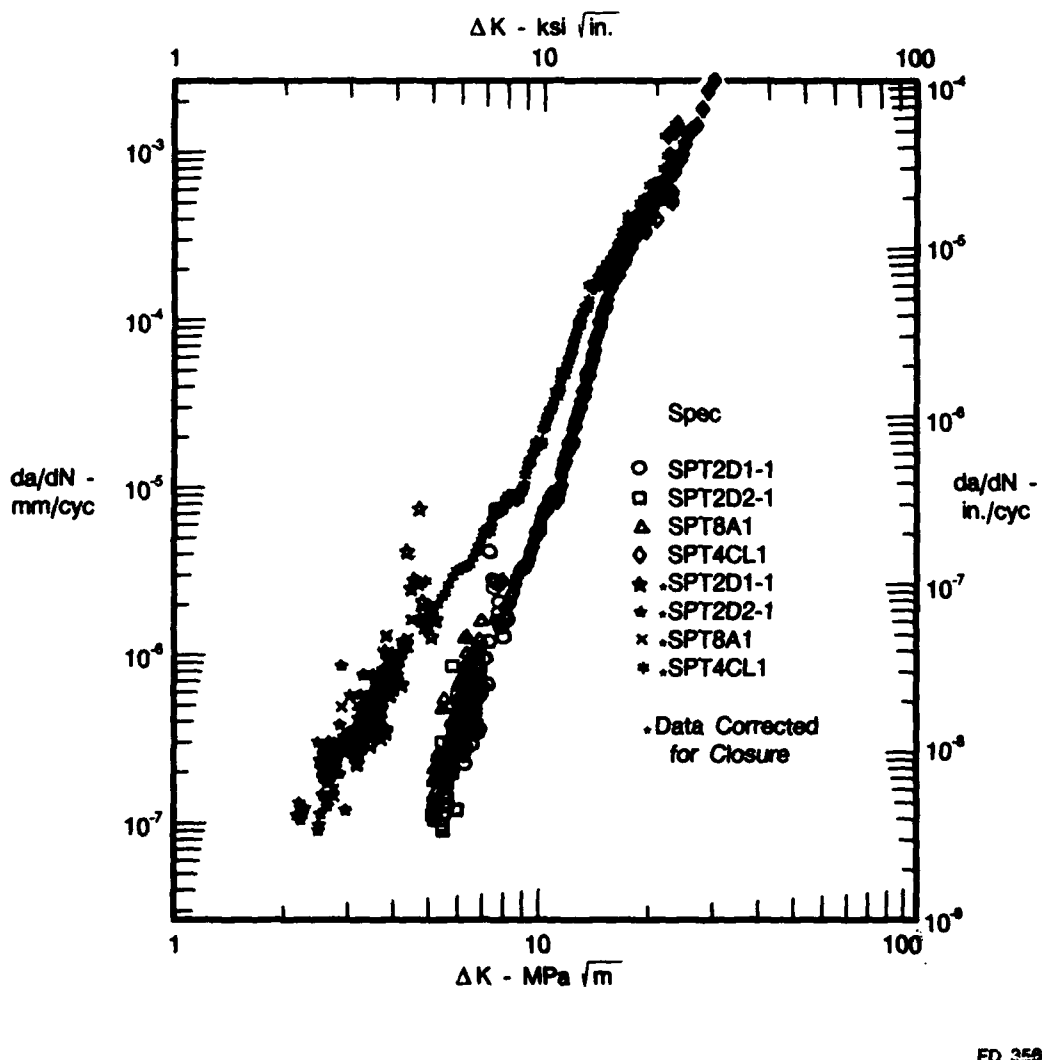
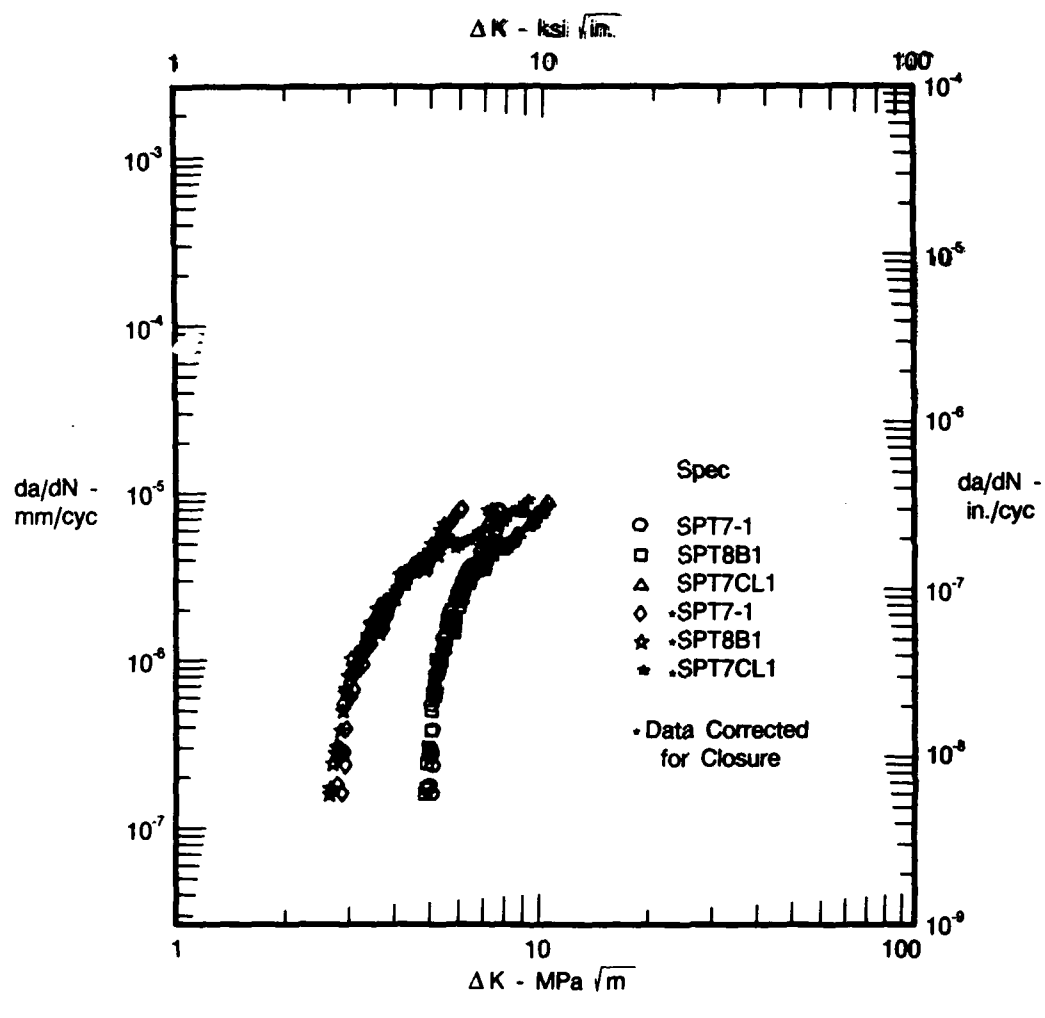
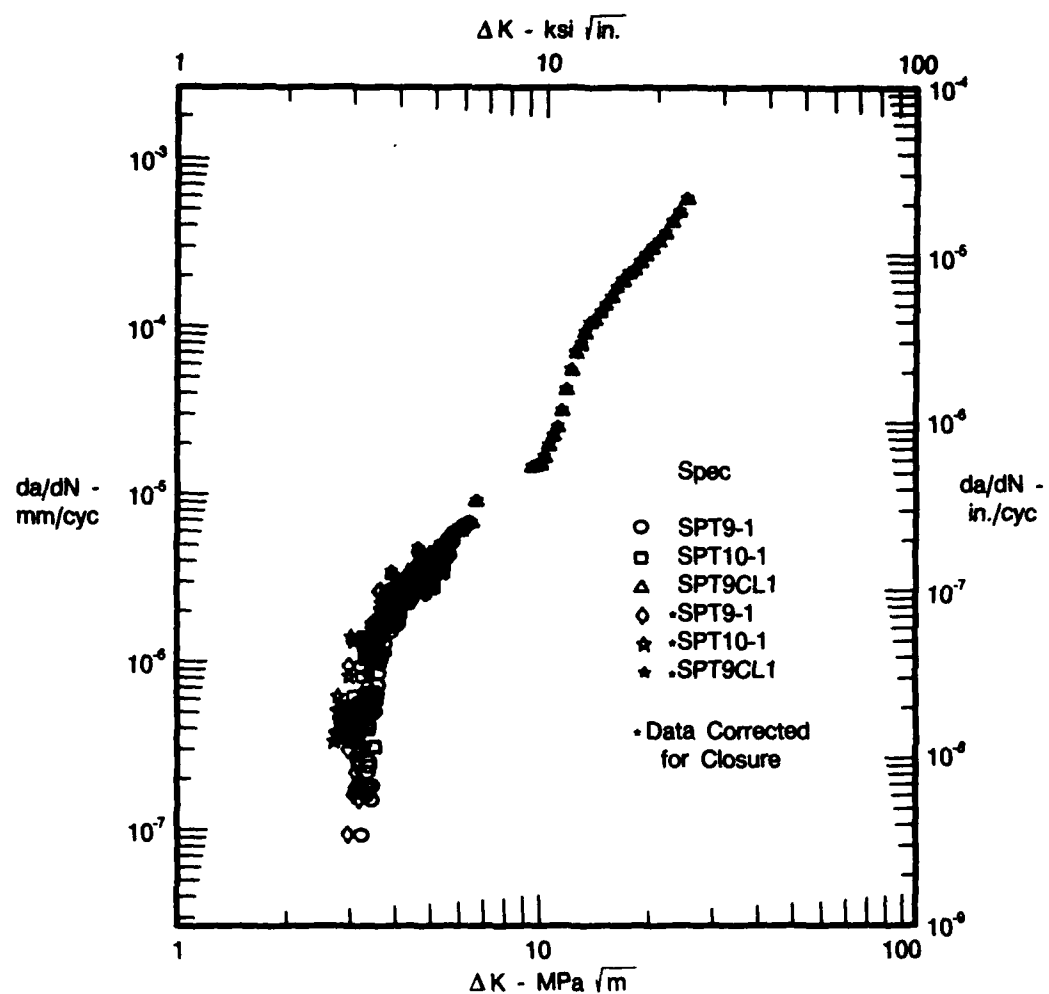


Figure 20. Combined Near-Threshold and Constant Amplitude FCG Data, 27°C, $R=0.1$, 20 Hz



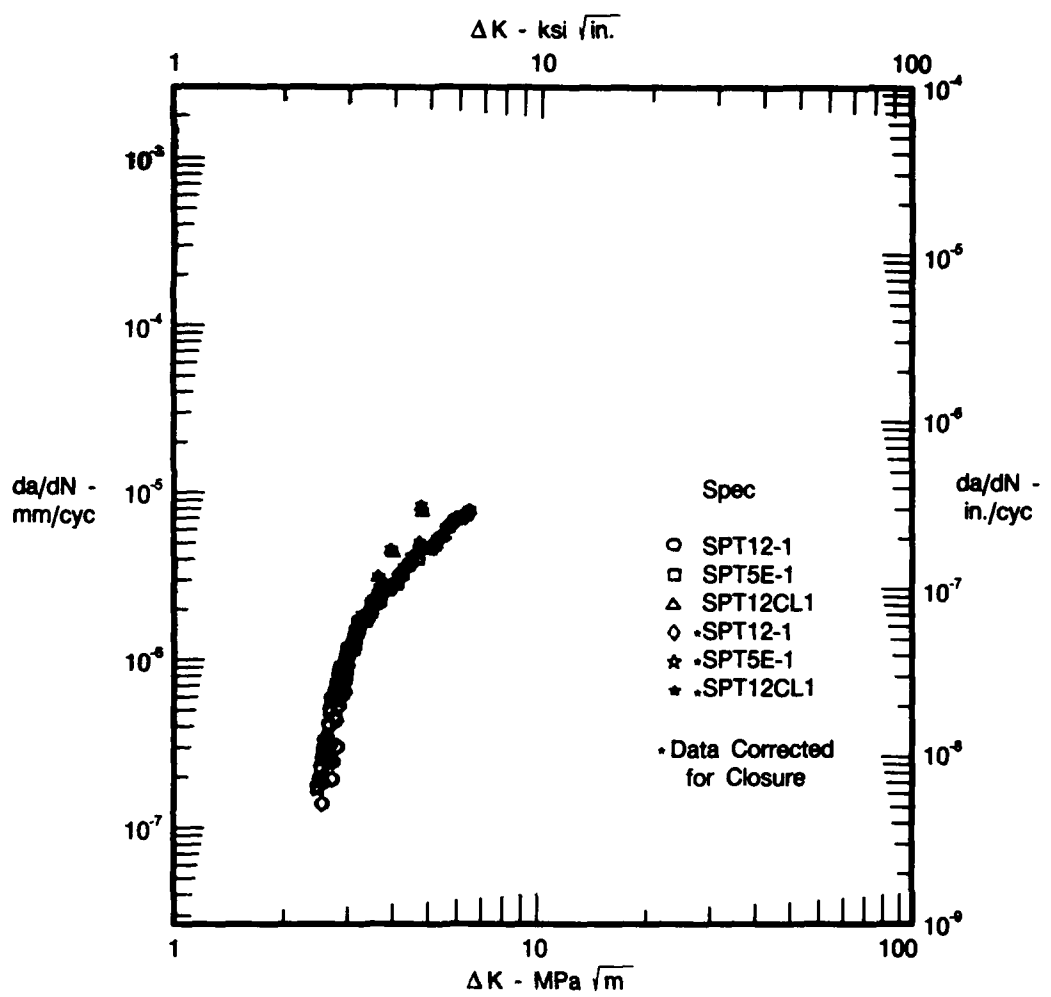
FD 356611

Figure 21. Combined Near-Threshold and Constant Amplitude FCG Data, 260°C, R=0.1, 20 Hz



FD 356612

Figure 22. Combined Near-Threshold and Constant Amplitude FCG Data, 260°C, R=0.5, 20 Hz



FD 356613

Figure 23. Combined Near-Threshold and Constant Amplitude FCG Data, 260°C, R=0.7, 20 Hz

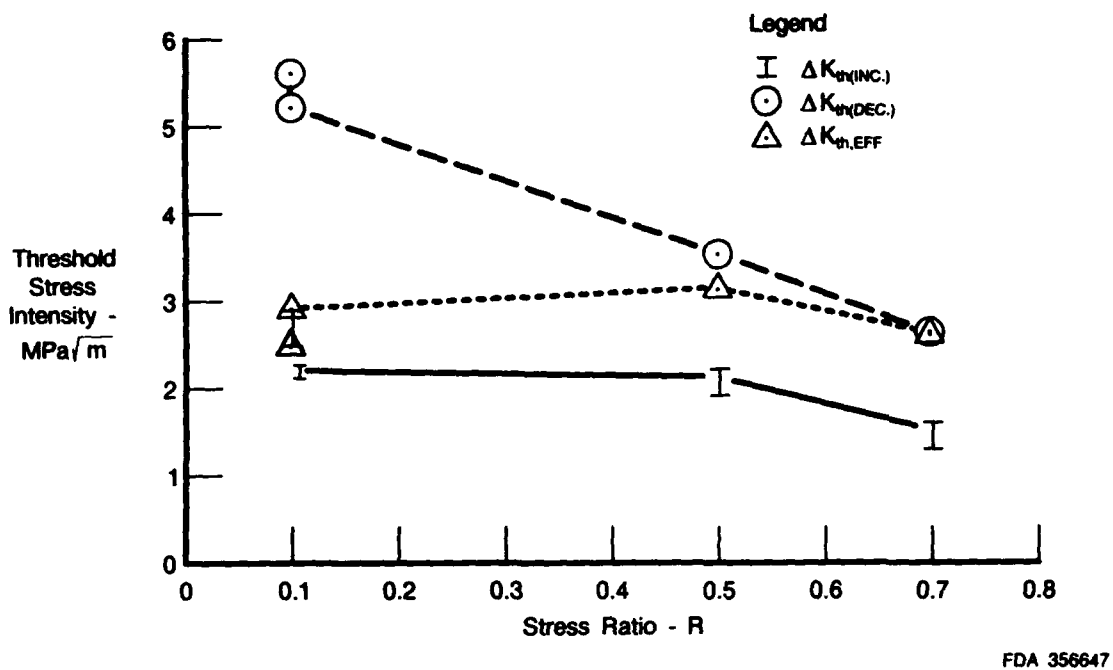
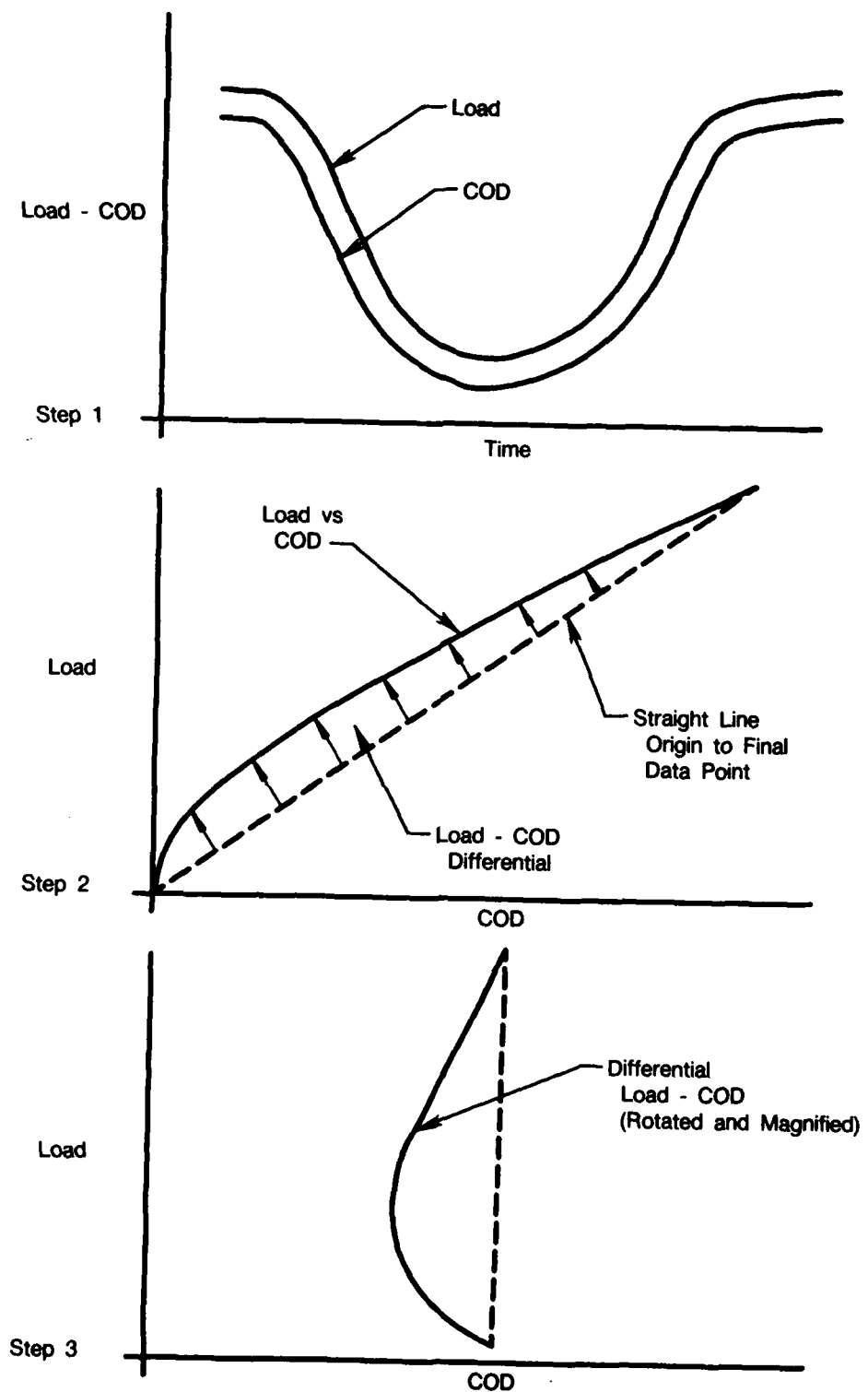


Figure 24. Threshold Stress Intensity Plotted as a Function of Stress Ratio

Closure

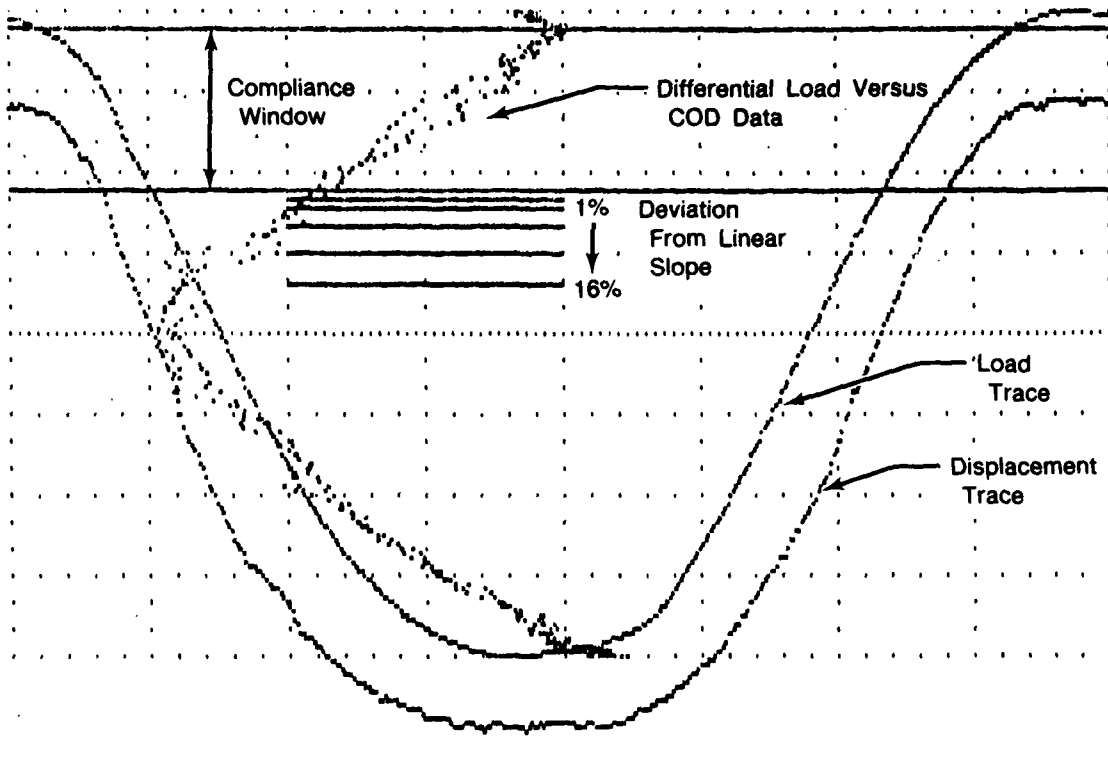
Crack closure can be an important aspect of near-threshold fatigue crack growth. The crack closure load, which corresponds to the point where the load/displacement curve deviates from linearity and the crack is actually closed, is used to determine an effective stress intensity range (ΔK_{eff}) at the crack tip. ΔK_{eff} is the true stress intensity range seen by the crack tip based on the portion of the load cycle in which it is open, and may be significantly less than ΔK calculated from the applied loads. Often, measurement of the crack closure load is essential to accurately determine the behavior of cracks in the near-threshold region. Crack closure loads were recorded during all tests run using the CT specimen. Closure corrected, ΔK_{eff} , crack growth data are compared to non-corrected, ΔK , data in Figures 20 through 23. As indicated by those figures, a significant closure correction is required for the $R = 0.1$ and $R = 0.5$ conditions. No closure loads were measured for the $R = 0.7$ tests. This would be expected since the high minimum loads associated with an $R = 0.7$ cycle hold the crack open at all times.

One method used for making closure measurements is illustrated in Figures 25 and 26. To emphasize the deviations from linear compliance, the load versus crack opening displacement (COD) relationship is plotted as the difference between the actual load-COD curve and a straight line. The procedure for developing those plots is illustrated schematically in Figure 25. The slope of the load-COD curve is then calculated. Finally, closure levels are defined at 1, 2, 4, 8, and 16 percent slope deviation. These calculations are made on both the loading and unloading portion of the cycle. The required load-COD information and the closure level calculations are recorded automatically over the course of a test. Details of the procedure are given in Appendix A. An example of a load-COD trace is given in Figure 26.



FDA 364412

Figure 25. Schematic Representation of Differential Load-COD Trace

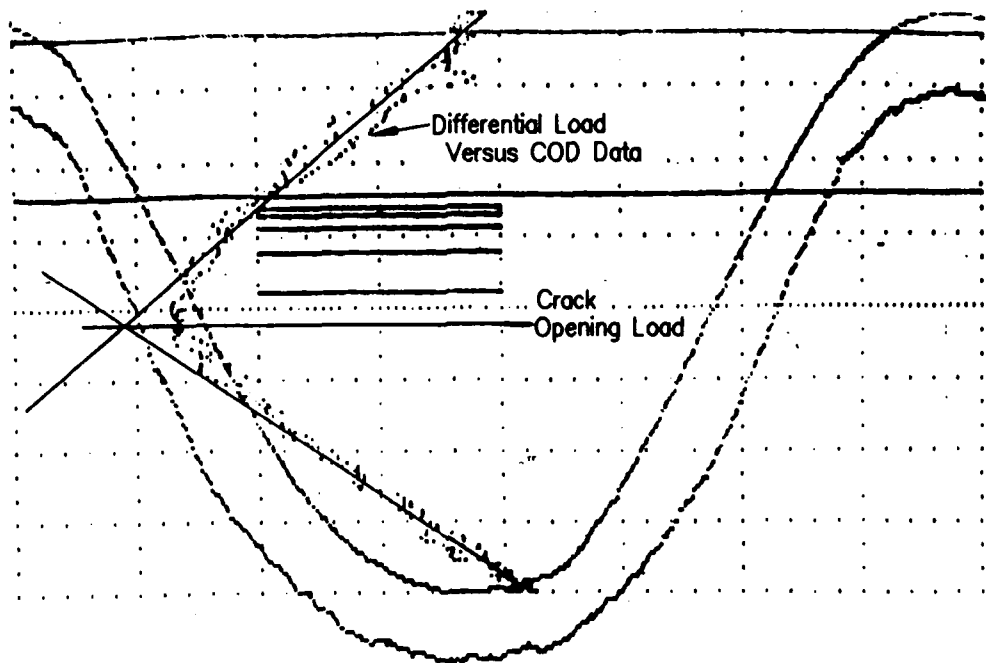


FDA 324776

Figure 26. Load vs COD Trace With Indicated Closure Levels, Testing at RT, R=0.1, 20 Hz

Note that in Figure 26 the deviations of 1-16 percent from a linear load-COD curve occur a considerable distance above the "knee" in the load-COD curve. This is typical of the $R = 0.1$ and 0.5 testing.

To address the apparent discrepancy in measured closure level vs the shape of the load-COD curve, a second method of closure measurement was employed. Figure 27 summarizes the procedure used for this method. Designated the tangent-intercept method, it consists of fitting the upper and lower portions of the differential load displacement curve with straight lines, and defining the crack opening load as the point where the two lines intersect. The lines are fitted manually. This procedure defines a crack opening load which is consistent with the shape of the differential load-COD curve. The method is also effective at collapsing the stress ratio effect observed in the uncorrected crack growth rate data. Figure 28 depicts all the 260°C crack growth rate data without closure correction and shows that the lower stress ratios display lower crack growth rates. Figure 29 shows the same data with closure correction based on the tangent-intercept method. It can be seen that the data for various stress ratios at 260°C collapse to a single curve. Closure corrections using the automated techniques resulted in a greater degree of scatter, even when using the maximum available correction of 16 percent as shown in Figure 30. Based on these observations, the tangent-intercept method was adopted as the basis for closure corrected comparisons, $\Delta K_{\text{th,eff}}$. The data presented in Table 4 reflect that decision.

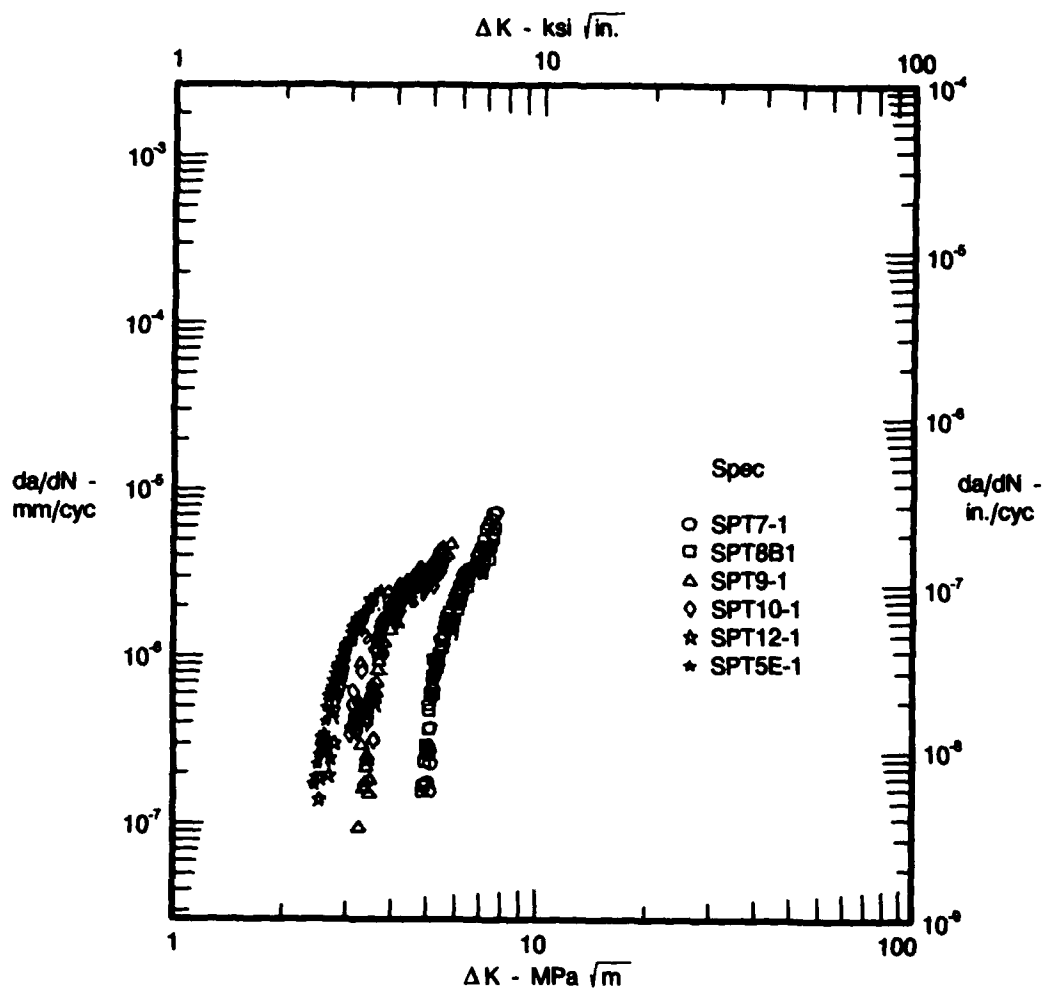


FD 345788

Figure 27. Load-COD Plot Showing the Opening Load Determined by the Tangent-Intercept Method

Several further observations can be made with respect to closure. The levels of closure observed for this material were relatively high, with crack opening loads approaching 60 percent of the maximum load in some cases. No closure was observed in the $R = 0.7$ test as would be anticipated. For the tests which displayed closure, the level of closure as a percentage of maximum load increased with increasing crack length, as illustrated in Figure 31. Similar opening loads occurred at equivalent levels of stress intensity, even with dissimilar crack lengths. Varying crack length did not effect the resulting values of ΔK_{th} or $\Delta K_{th,eff}$. This is confirmed by the test in Figure 32 which shows two threshold tests run sequentially using the same specimen. The resulting crack growth rates are identical even though the ranges of crack lengths were 11.15 to 14.42 mm versus 16.23 to 18.80 mm.

These observations raise the question of closure in the K -increasing bend-specimen tests. If it is assumed that plastic-wake closure is the main operative mechanism, it can be seen that the effects of closure should be minimized in these tests. The test geometry does not lend itself to the development of plastic wake closure. The majority of the precrack is machined off prior to testing, leaving a relatively short crack, (about 0.3 mm). The remaining crack has been exposed to minimal positive stresses, and would therefore experience only small plastic deformations at the crack tip. Finally, the results of this test are based only on the initiation of crack growth. Actual growth rates after the crack has grown a finite amount are not measured. Thus, development of plastic wake closure with crack extension should not affect the test results.



FD 356614

Figure 28. Near-Threshold Fatigue Crack Growth Without Correction for Crack Closure for R=0.1, 0.5, 0.7 at 260°C

Even though these arguments suggest that the effects of closure are minimized in the K-increasing, bend-specimen test technique, that phenomena should not be completely discounted. Attempts to perform closure measurements on this specimen geometry at WRDC were inconclusive. Crack front irregularities and difficulties with gripping fixtures precluded an accurate assessment of closure levels. The data obtained, while questionable, indicated a trend toward lower closure levels than were observed in CT specimens. Further, it appeared that some crack extension was required to fully develop the closure loads. Since these specimens were used only to indicate the onset of crack extension, and not to measure crack growth rates directly, closure levels obtained after significant crack extension would probably not materially affect the final values of ΔK_{th} . In any event, the closure measurements obtained were not judged to be of adequate reliability to warrant their incorporation into the data analysis for this contract.

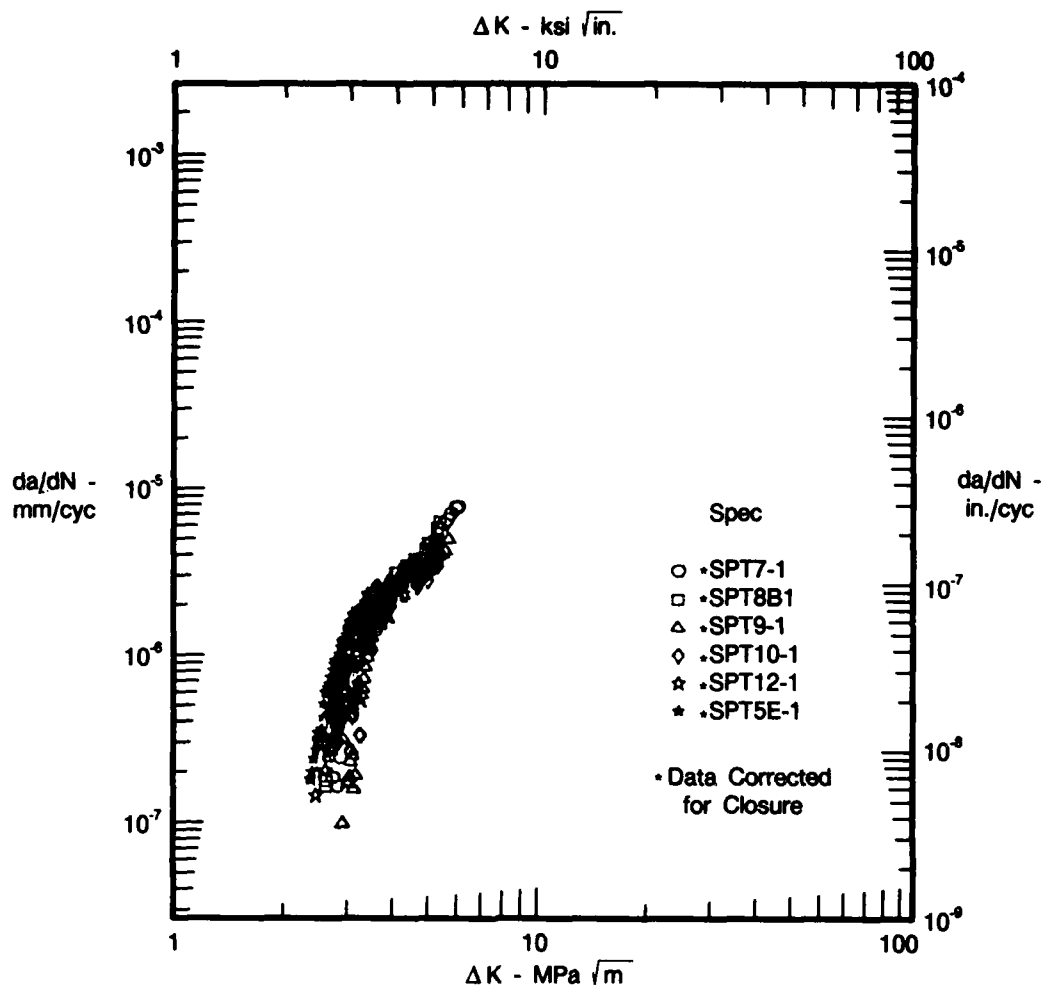
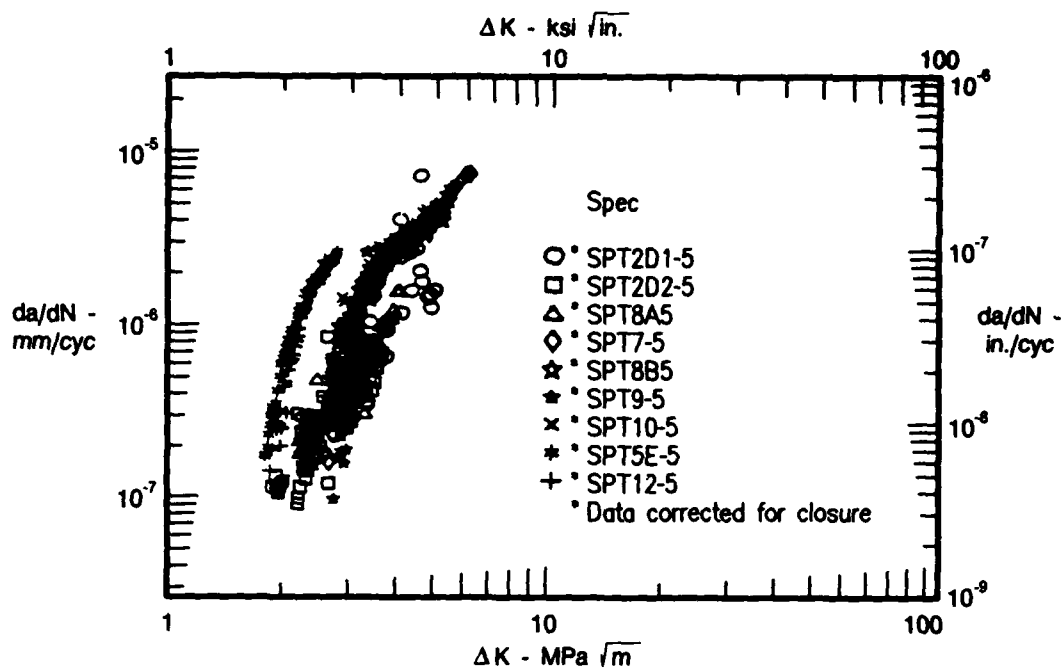


Figure 29. Near-Threshold Fatigue Crack Growth With Correction for Crack Closure for R=0.1, 0.5, 0.7 at 260°C

Effect of Secondary Parameters

The effects of temperature, frequency, and time dependence on ΔK_{th} were examined over limited ranges. For the materials and conditions of interest for this program, it was expected that these parameters would have minor effects on ΔK_{th} , so there were relatively few tests conducted in this context. The results of those tests are summarized below.

Threshold testing was conducted at two temperatures, 27°C and 260°C. The data in Table 3 indicate that a small reduction in ΔK_{th} occurs at elevated temperature. That is consistent with the general trend toward faster crack growth rates at elevated temperatures for higher values of ΔK , seen in standard crack growth rate tests for Ti 8-1-1. It is also consistent with the CT data in Table 4. The constant-load testing, run with CT specimens in conjunction with the K-decreasing tests, indicates that the temperature effect is somewhat larger at crack growth rates above the threshold level.



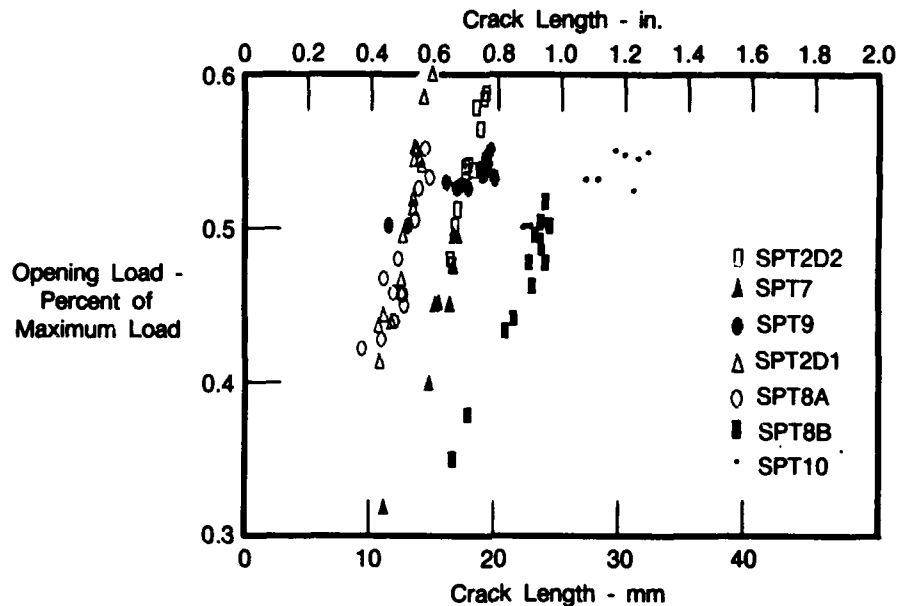
FD 356606

Figure 30. Near-Threshold FCG Curves With Correction for Crack Closure Using 16 Percent Slope Deviation Method to Determine Opening Load

The majority of the testing was done at a frequency of 30 Hz (20 Hz for the CT tests). A series of tests was conducted at 200 Hz, which is representative of blade vibration, to check for effects of frequency. The 200-Hz data indicate that, with a single exception, there is no discernible effect of frequency on ΔK_{th} as compared to the 30-Hz information. Although the 200- and 30-Hz data do not coincide exactly for all conditions, the ΔK_{th} values for both frequencies fall within reasonable experimental limits. Further, where the data do not fall within the same ΔK_{th} ranges, the higher frequency results are not consistently higher or lower than the low frequency results. The exception to those observations are the results at 200 Hz, $R = -1.0$. The ΔK_{th} values at that condition are about 0.55 to 0.66 MPa \sqrt{m} lower than the 30 Hz values. This difference is on the upper limit of the expected experimental error. To confirm the validity of the 200-Hz information, the test equipment was carefully reviewed. No error of sufficient magnitude to account for the observed difference in ΔK_{th} was found. Since the preponderance of data indicates little frequency effect, it appears that this difference in ΔK_{th} at $R = -1.0$ should be attributed to material scatter.

Two conditions were tested to address time-dependent behavior. Those tests are listed in Table 3 as 200-Hz/2-minute dwell. The cycle was intended to represent an intermittent vibration. As shown in Figure 33 the cycle consisted of 200 Hz vibratory loading interrupted by two-minute dwell periods at the mean load. The vibratory segments were also two minutes in duration. The tests were run at high stress ratios to ascertain the effect of high mean stress dwell times on ΔK_{th} . Both conditions were tested at elevated temperature to emphasize any time-dependent behavior. A runout for this cycle was defined as 5×10^6 high frequency cycles (as opposed to 1×10^7 cycles in a standard cyclic test), so the total exposure time at or above the mean stress would be equivalent to a simple cyclic test. At $R = 0.5$, the intermittent hold times appear to have no effect, with ΔK_{th} values roughly equivalent to the 200-Hz cyclic results (and almost exactly equivalent to the 30-Hz results). A different result is seen in the $R = 0.7$ data. The

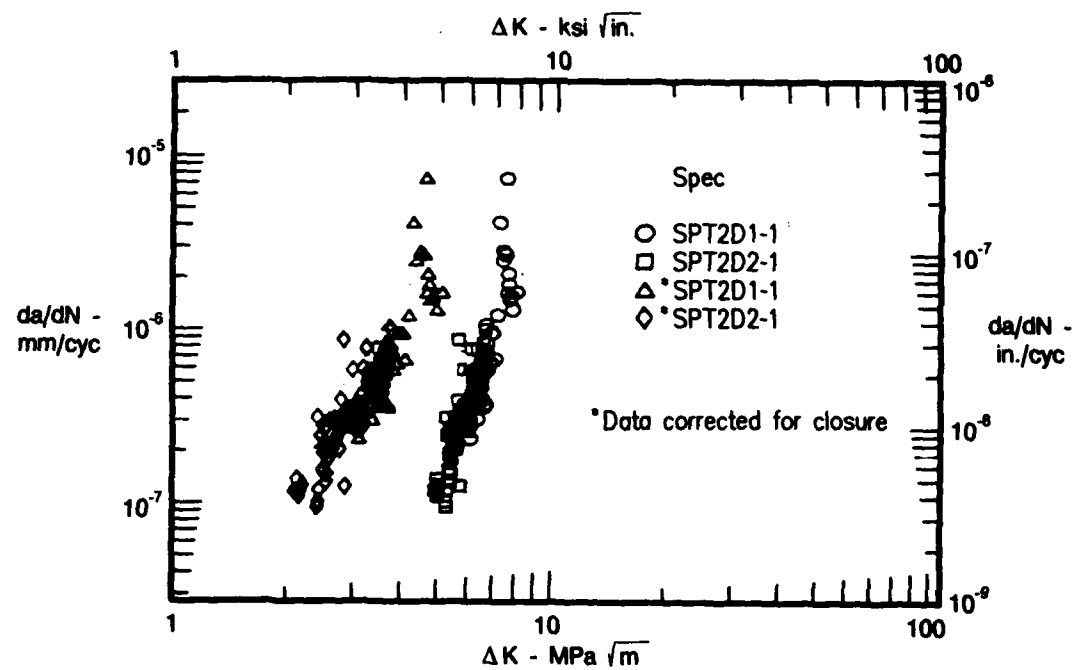
200-Hz/2-minute dwell cycle produced a ΔK_{th} almost 1.1 MPa \sqrt{m} higher than the 200-or 30-Hz cyclic tests. This magnitude of difference is outside what can be explained in terms of material behavior or experimental error. Visual observation of the crack tip disclosed no unexpected behavior, such as an obviously blunted crack.



FD 356607

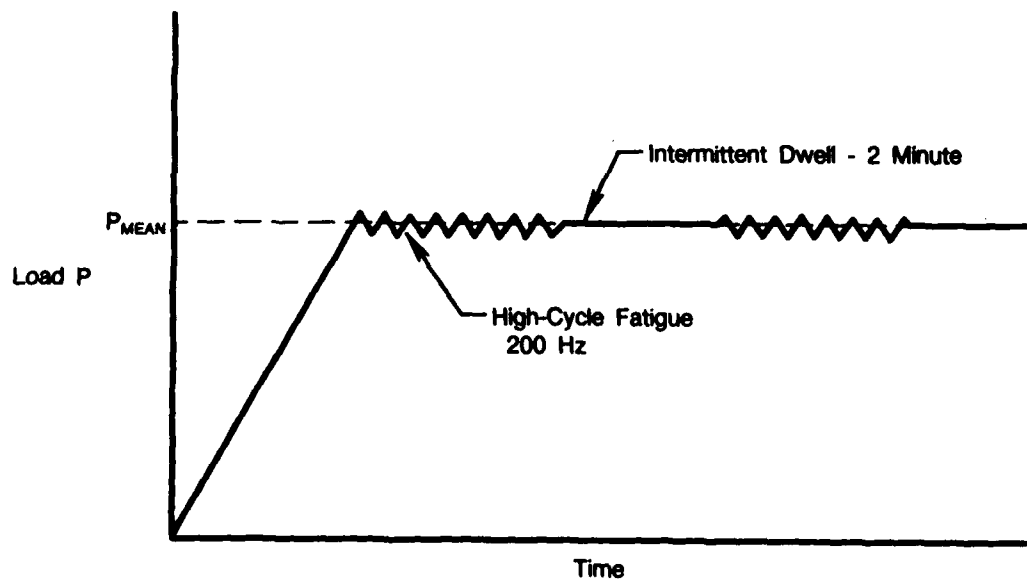
Figure 31. The Effect of Crack Length on the Opening Load for Specimens with Crack Closure

Fracture surfaces from specimens tested at 200 Hz and 200-Hz/2-minute dwell were also compared using scanning electron microscopy (SEM). The specimens examined were those which defined the upper bound of the ΔK_{th} ranges listed in Table 3. Particular attention was paid to the area directly adjacent to the precrack, which should be representative of the lowest crack growth rates. Typical fractographs of those areas are given in Figure 34. The fracture surfaces are similar, dominated by fine cleavage, with the 200-Hz fracture appearing slightly more brittle. This observation is consistent with the lower ΔK_{th} range displayed for that cycle at $R = 0.7$, but does not provide a complete explanation of the difference in ΔK_{th} levels. If there is a difference in fracture mechanism for the two cycle types, it is not readily discernible through SEM fractography. These results lead to one of two conclusions: (1) the vibratory cycles at high stress ratios are considerably more damaging than the mean load dwells, or (2) a time-dependent mechanism is retarding the near-threshold crack growth.



FD 356608

Figure 32. Comparison of the FCG Curves From Sequential Threshold Tests, Demonstrating Negligible Crack Length Effects



FDA 326730

Figure 33. Combined High-Frequency/Hold-Time Cycle for Determining Time Dependence

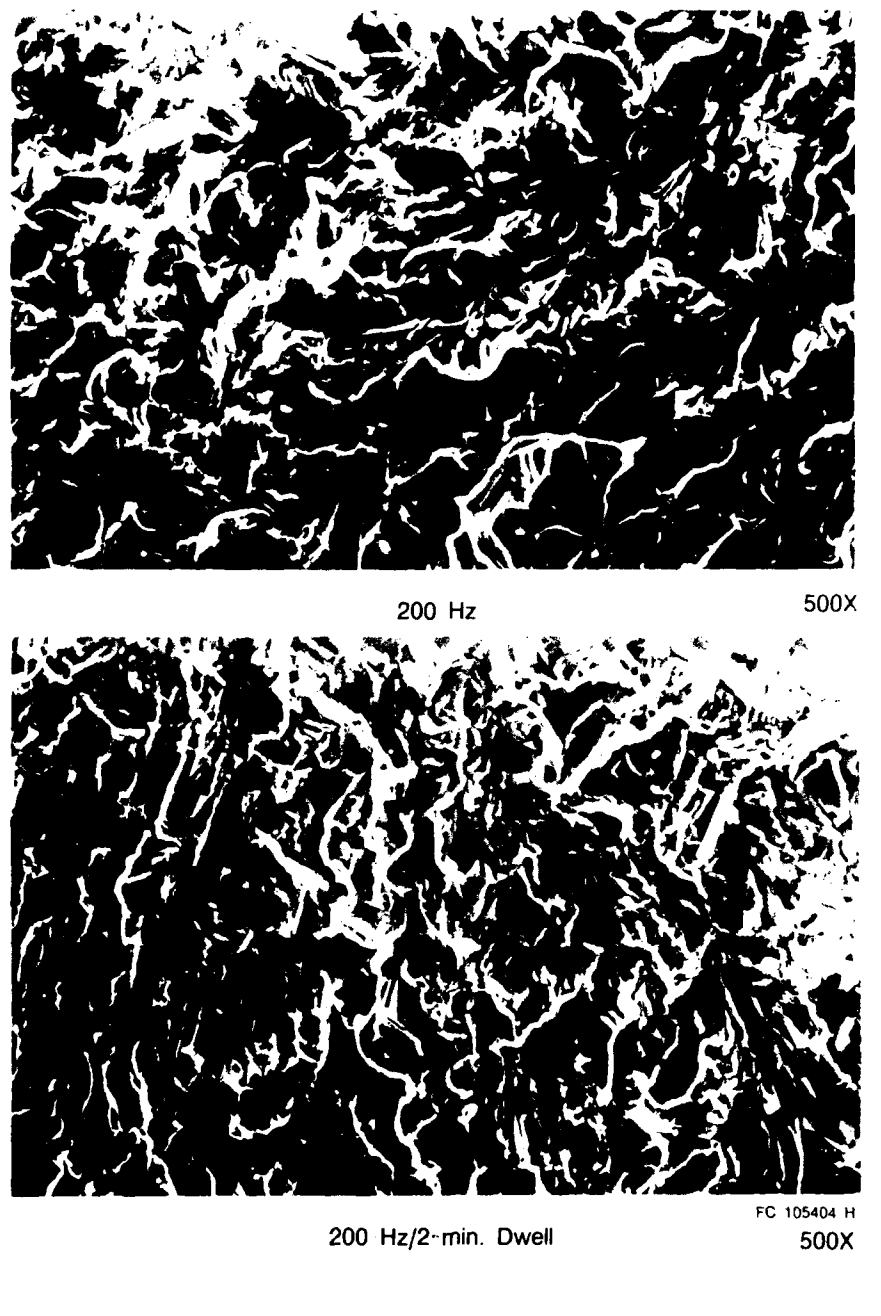


Figure 34. Fracture Surface Comparison of 200 Hz vs 200 Hz/2-Minute Dwell Threshold Tests

Test Method Comparisons

One of the goals of this program was to establish the uniqueness of ΔK_{th} as determined by various test techniques. As described in previous sections, a simple determination of ΔK_{th} using the bend specimen in a K-increasing test does not yield the same values for ΔK_{th} as does the CT specimen in a K-decreasing test.

Application of closure measurements to the CT data to produce $\Delta K_{th,eff}$ values brings closer agreement to the results of the two test techniques. This is not surprising since one might

anticipate a considerable difference in closure behavior in such different geometries. However, this approach is not without its own difficulties. As demonstrated by the previous comparison of the slope-deviation and tangent-intercept methods, the closure measurement technique can affect the final $\Delta K_{th,eff}$ value to a sizeable degree. In addition, using even the most successful closure correction method, the observed differences in the values of ΔK_{th} between test methods was much larger than within a single method. This was also true for $R = 0.7$ where no closure effects were present. Further, in some instances, (such as the bend specimen used for this study) the specimen geometry does not lend itself to straightforward closure measurements. In terms of application, using $\Delta K_{th,eff}$ requires the estimation of closure levels in the component geometry of interest, a not insignificant complication.

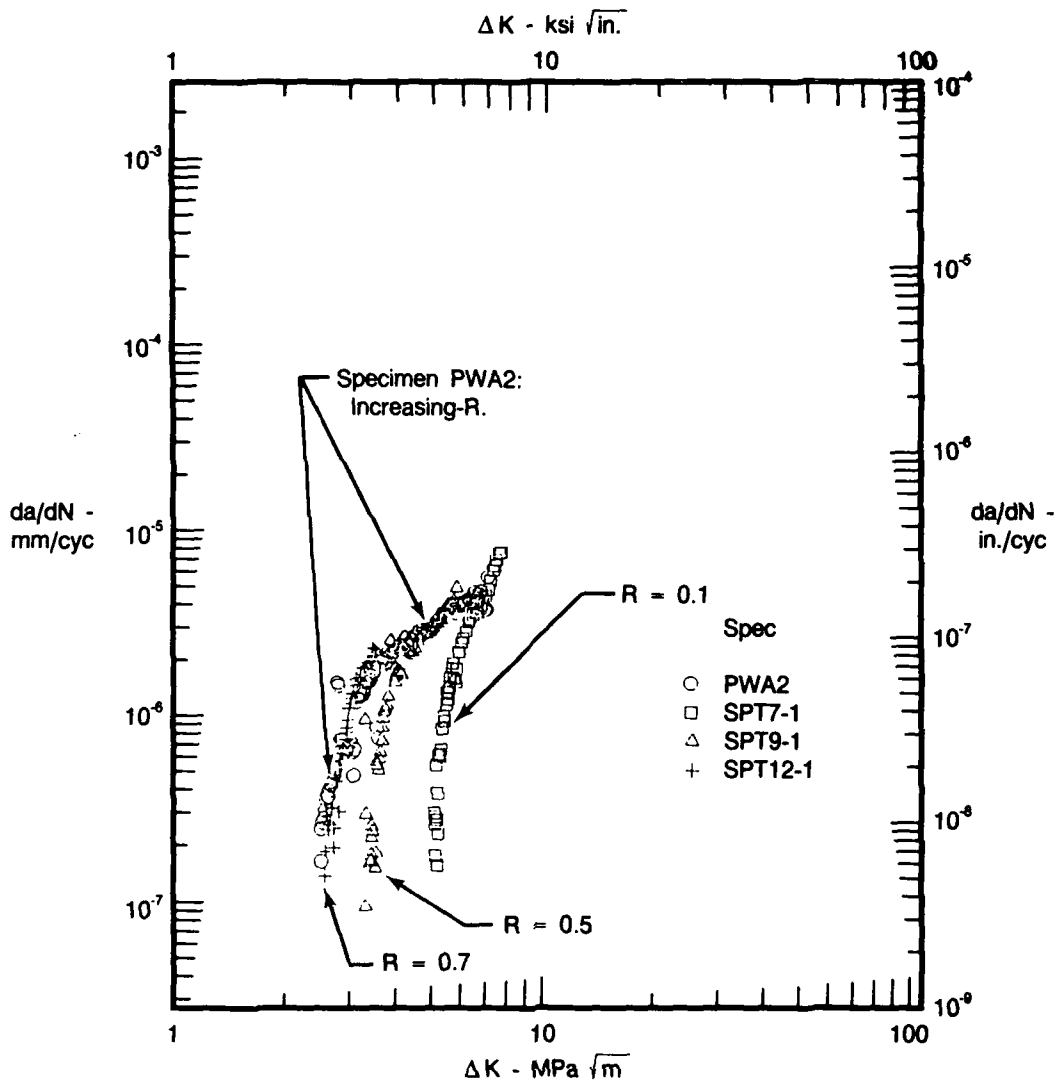
A second type of test using the CT specimen was conducted at FAU. This test cycle holds K_{max} constant, and increases stress ratio to reduce ΔK and decrease crack growth rates. K_{max} is held constant by decreasing the maximum load in a manner similar to the K-decreasing test discussed earlier. One advantage of this test is the ability to reduce the loads rapidly. This is possible since a constant K_{max} results in a constant plastic zone size, thus negating concerns over crack growth retardation due to load shedding rate.

The results of the constant K_{max} , increasing R test are compared to K-decreasing, constant-R tests in Figure 35. The test was started at a stress ratio of $R = 0.1$, and no closure loads were discernible after R had been increased to 0.6-0.65. As shown in Figure 35, the data transitions between the $R = 0.1$ and $R = 0.7$ constant-R curves as the stress ratio is increased. The data merges with the $R = 0.7$ constant-R results at the approximate point where the crack closure level is equal to P_{min} , the minimum load. In general, this test shows excellent agreement with the K-decreasing, constant-R tests.

A second constant K_{max} , increasing-R test was conducted to confirm these results. The second test, specimen PWA1, displayed a slightly lower threshold than the previous test, specimen PWA2. Crack growth rate data from the two tests are compared in Figure 36. Although there is a noticeable difference in crack growth rates, the values of ΔK_{th} calculated from Paris curve fits are nearly equal, $2.28 \text{ MPa} \sqrt{\text{m}}$ vs $2.16 \text{ MPa} \sqrt{\text{m}}$. The lower crack growth rates displayed by specimen PWA1 may be due to material scatter. However, the threshold portion of the test did have to be restarted after the crack was blunted during a power failure. Thus it is possible that prior loading history had some effect on the crack growth rates. To avoid confusion over this point, only specimen PWA2 was included in the comparisons in Figure 35.

Because of the difficulties and expense of obtaining ΔK_{th} data, it is not uncommon to model standard crack growth rate data as a sinh curve and extrapolate into the threshold region to obtain estimates of ΔK_{th} . This has been done with some degree of success at P&W. (Reference 1.) This technique was applied to the Ti 8-1-1 data, and the results are discussed below.

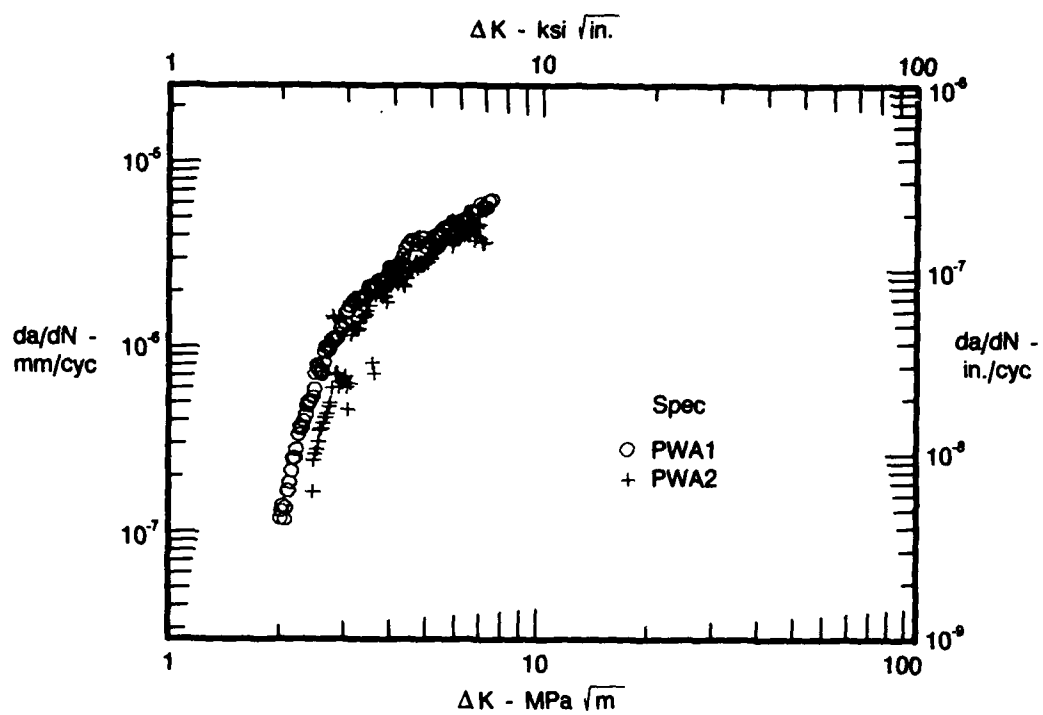
Extrapolation of crack growth data generated using center-cracked-tension (CCT) specimens produces estimates of ΔK_{th} which are higher than those obtained with the threshold-bend-type specimen. Figures 37 and 38 compare threshold results to CCT data at room temperature and 260°C, respectively. In both cases the threshold data was obtained at $R = 0.1$ and 30 Hz, and the CCT data was obtained at $R = 0.05$ and 20 Hz. These small differences will not materially affect the ΔK_{th} comparisons. From these figures, it is apparent that extrapolating CCT data results in ΔK_{th} estimates which are approximately $3.3 \sqrt{\text{m}}$ higher than those obtained from threshold specimens. If not entirely due to extrapolation error, this difference can probably be related to a closure mechanism, as discussed earlier.



FD 356616

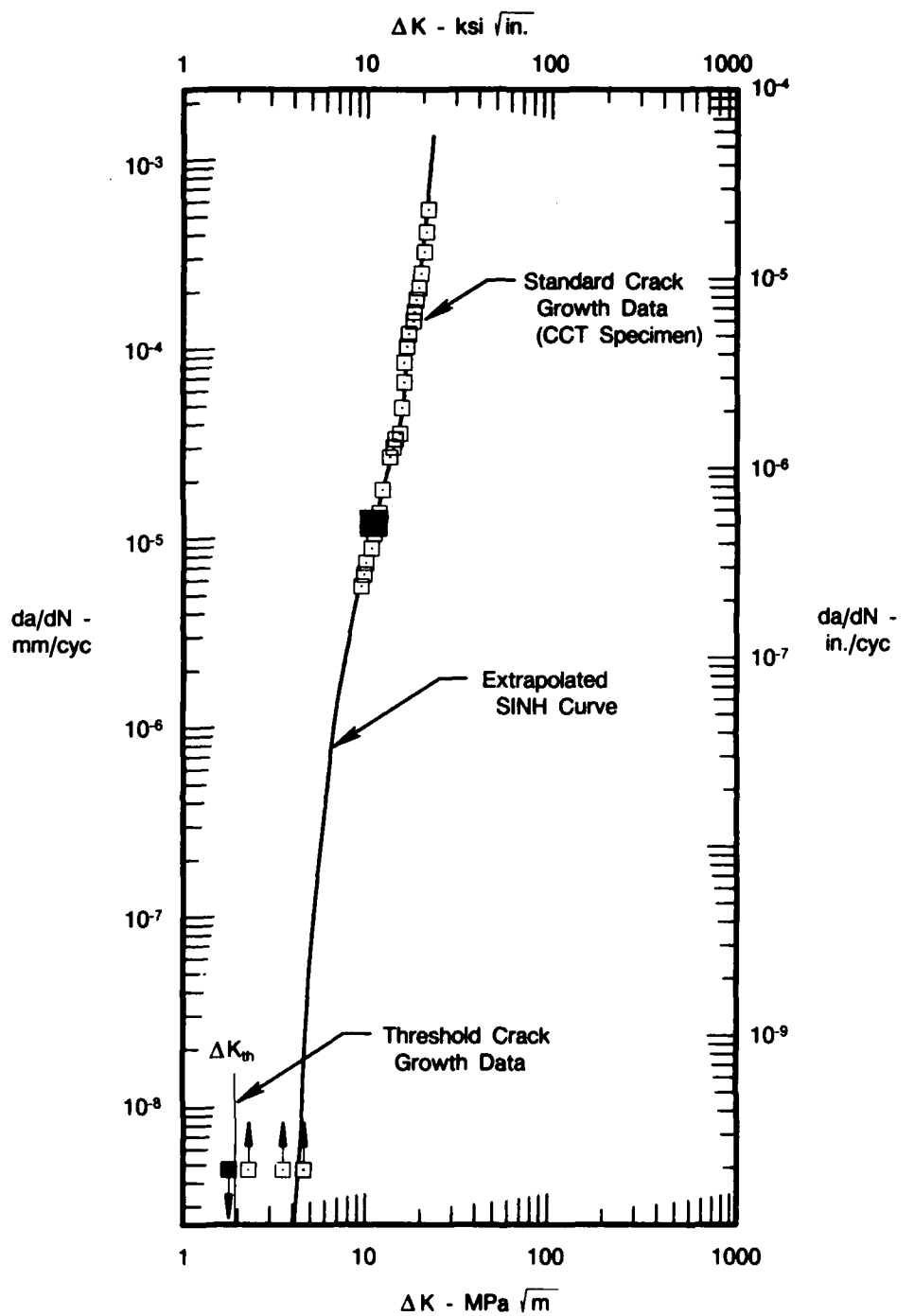
Figure 35. Comparison of Increasing-R and Constant-R Near-Threshold Fatigue Crack Growth Rates at 260°C

In summary, then, while it can be concluded that a closure correction is likely to provide more reproducible values of ΔK_{th} (or $\Delta K_{th,eff}$) between various test methods and geometries, it does not guarantee the generation of unique ΔK_{th} values in all instances. Use of threshold information must then include careful consideration of the respective geometries, test methods, and method of application.



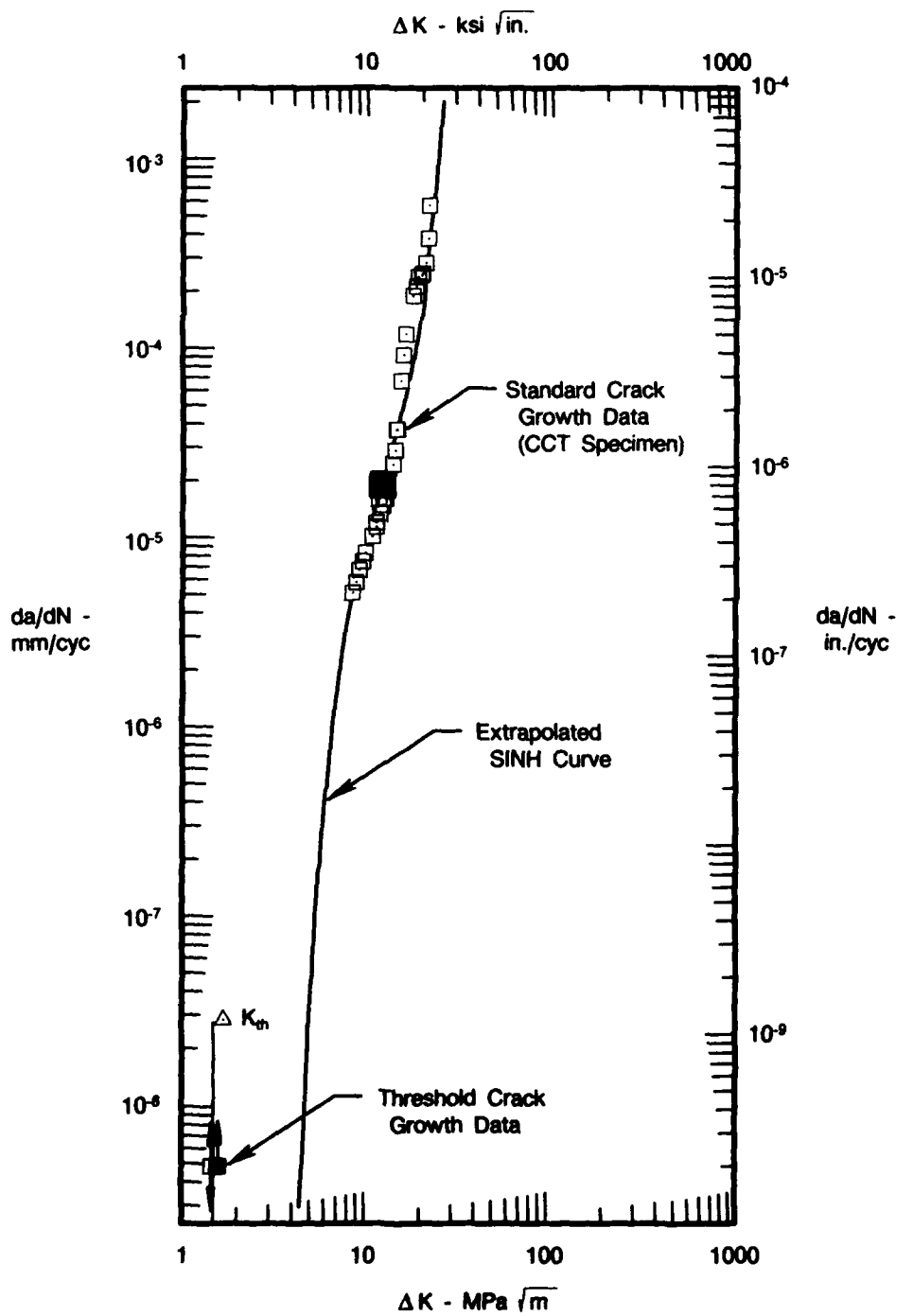
FD 356617

Figure 36. Constant K_{max} Increasing-R Threshold Crack Growth Rates at 260°C, 20 Hz



FDA 356620

Figure 37. PWA 1202 Crack Growth Rate Data, Comparing Methods for Determining ΔK_{th} at 27°C, $R=0.1$, 30 Hz



FDA 356619

Figure 38. PWA 1202 Crack Growth Rate Data, Comparing Methods for Determining ΔK_{th} at 260°C, $R=0.1$, 30 Hz

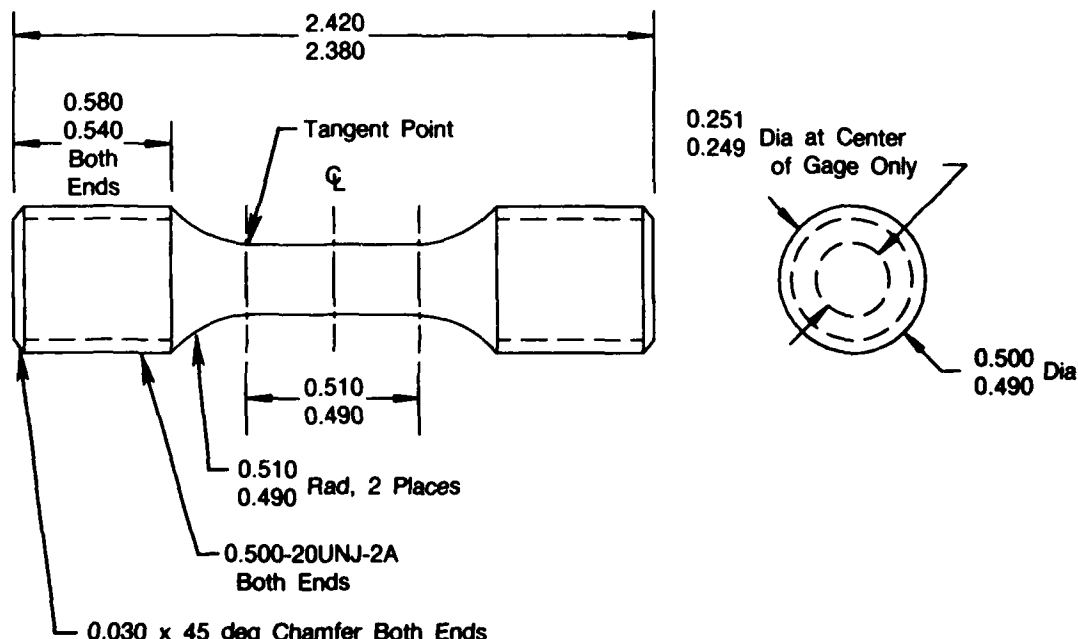
SECTION IV

TASK III — SMOOTH BAR FATIGUE TESTING

The main objective of this task was to produce conventional Goodman diagrams for comparison to the threshold approach described in Tasks II and IV. The testing for this task was divided into two components: (1) Smooth bar baseline tests, representative of material which contains only intrinsic defects, and (2) nominally smooth bars containing extrinsic defects similar to FOD. Goodman diagrams were developed for both these cases. Also included in this task was the fractography required to establish typical initial flaw sizes in the undamaged material and to document the actual sizes of the simulated FOD.

Test Specimens and Procedure

All of the smooth bar tests were axial load-controlled fatigue tests using a smooth ($K_t = 1$) specimen with a polished gage section. Tests were conducted at 30 Hz (sinusoidal waveform) for the basic tests, with stress levels selected to produce S-N curves from about 5×10^4 to a least 10^7 cycles. This required six to eight tests per S-N curve. Temperatures and cycle types are consistent with the threshold tests described in Task II. The specimen used is shown in Figures 39 and 40. Tests were conducted at two temperatures, 27°C and 260°C, and three stress ratios, $R = 1.0, 0.1$, and 0.5 . One additional stress ratio, $R = 0.7$, was tested at 260°C for comparison to cyclic/dwell tests outlined below.



FDA 292179

Figure 39. Smooth HCF Specimen



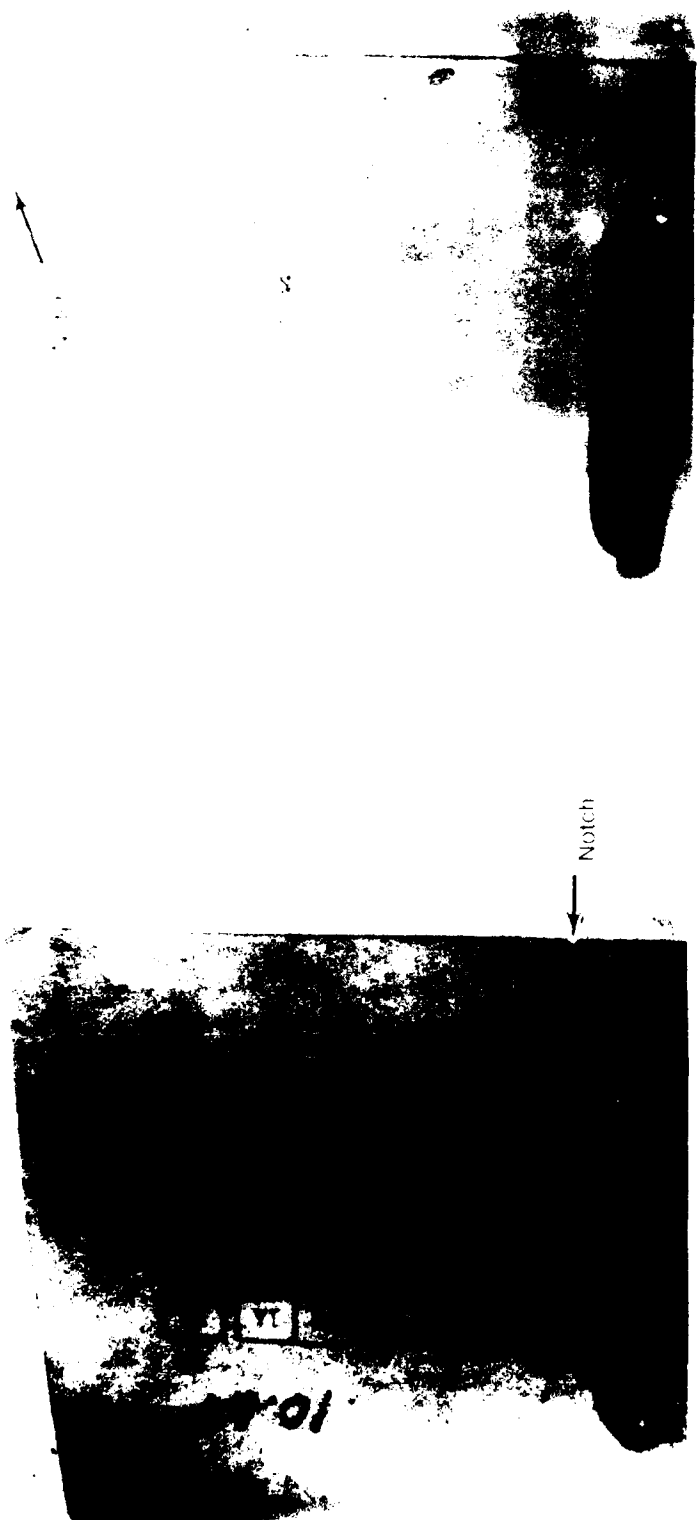
FE 286723

Figure 40. Typical Smooth HCF Specimen

To assess time-dependent effects on HCF behavior, smooth HCF tests were conducted using a cycle interrupted by periodic dwells at mean load similar to that shown in Figure 33. There are two differences in this cycle versus the cycle employed for the threshold test. First, the cyclic portion of the test was run at 30 Hz as opposed to 200 Hz. This frequency was dictated by test machine limitations. Second, a runout was defined as 10^7 cycles, vs 5×10^6 cycles, for consistency with the remainder of the HCF data.

Two defect levels were tested. In light of previous discussions concerning the importance of FOD to blade HCF capability, it was desirable that these defects be representative of FOD. Consequently, the defects represented two levels of FOD damage in the form of sharp nicks. Damage of this type is routinely applied to fan and compressor blades, which are subsequently HCF-tested to measure effects of such damage on fatigue capability. Examples of blades with induced nicks are shown in Figure 41.

For the purposes of this testing, worst case FOD was simulated. That damage consists of sharp notches with minimal residual stress at the base of the notch. The flaws were introduced into the specimens by impacting the center of the gage section perpendicular to the longitudinal axis with a very sharp cutting tool. Each tool is used only once, then resharpened. This procedure produces a sharp notch through shearing action, thereby minimizing compressive residual stresses. A typical notched HCF specimen is shown in Figure 42.



1st Stage Fan Blade Tested in First
Bending Mode of Vibration

1st Stage Fan Blade Tested in First
Bending Mode of Vibration

FD 149020

Figure 41. V-Notch in Ti 8-1-1 1st-Stage Fan Blades

The target sizes for the defects in this program were 0.2 and 0.38 mm in depth. Those sizes are roughly equivalent to the mode of the repairable and non-repairable FOD distributions defined in the following sections.



FC 105400 H

FD 345803

Figure 42. Typical Notched HCF Specimen With a 0.20 mm-Deep, 60-Degree V-Notch

All the defect containing tests were conducted at 260°C and 30 Hz, over the same range of stress ratios as the smooth HCF tests.

The testing in this section was accomplished on closed-loop servohydraulic fatigue machines. Heating was supplied by electrical resistance clamshell furnaces which enclosed the entire specimen. Temperatures were monitored by thermocouples attached to the specimen and were controlled to within $\pm 3^{\circ}\text{C}$. Approximately 30 percent of the testing was done by METCUT Research Associates in Cincinnati, Ohio. The results of that testing were spot-checked at P&W and proved to be indistinguishable from in-house results.

All of the smooth and notched HCF data was plotted in the form of S-N curves, modeled, and converted to Goodman diagrams.

The model selected to represent the S-N data was based on tensile hysteretic energy as proposed by Ostergren (Ref. 6), with simplifications to represent the inelastic strain range (Ref. 7). The relevant cyclic energy and associated damage parameter can be represented as follows:

$$\Delta W = \int \sigma_T d\epsilon \approx \sigma_T \Delta \epsilon_i \quad (3)$$

where ΔW represents the cyclic tensile hysteretic energy, σ_T the maximum stress, and $\Delta \epsilon_i$ the cyclic inelastic strain range. ΔW is then assumed to be related to the number of cycles to failure, N_f , by

$$N_f = A(\Delta W)^B \quad (4)$$

where A and B are constants. Recognizing that the maximum stress σ_T is the sum of the mean stress σ_{mean} and half the cyclic stress range, $\Delta\sigma/2$, gives

$$N_f = A[(\sigma_{\text{mean}} + \Delta\sigma/2)(\Delta \epsilon_i)]^B \quad (5)$$

The inelastic strain range can be presented by the power law relationship:

$$\Delta \epsilon_i = (\Delta\sigma/C)^D \quad (6)$$

where C and D are constants. Combining with equation (5) gives

$$N_f = A[(\sigma_{\text{mean}} + \Delta\sigma/2)(\Delta\sigma/C)^D]^B \quad (7)$$

For use as a regression model, equation (7) can be simplified to:

$$N_f = A'(\sigma_{\text{mean}} + \Delta\sigma/2)^B(\Delta\sigma)^D \quad (8)$$

which represents life as a function of mean and alternating stress, with three unknowns to be determined by regression analyses. For simplicity in the regression, the maximum stress σ_T was used in place of the term $(\sigma_{\text{mean}} + \Delta\sigma/2)$.

Coefficient of correlation and standard error estimates from the regression analyses proved satisfactory where this model was used, which facilitated easy representation of the modified Goodman Diagrams (constant life lines for mean stress vs alternating stress).

TESTING AND FRACTOGRAPHY RESULTS

Testing

The baseline Goodman diagrams generated from smooth bar testing are shown in Figures 43 and 44. The Goodman diagrams are based on the S-N behavior illustrated in Figures 45 through 50. The specific stresses called out on the Goodman diagrams are the fatigue limit stresses from the individual S-N curves corresponding to 10^7 cycles. Both mean and minimum curves are included on the Goodman diagrams and S-N curves.

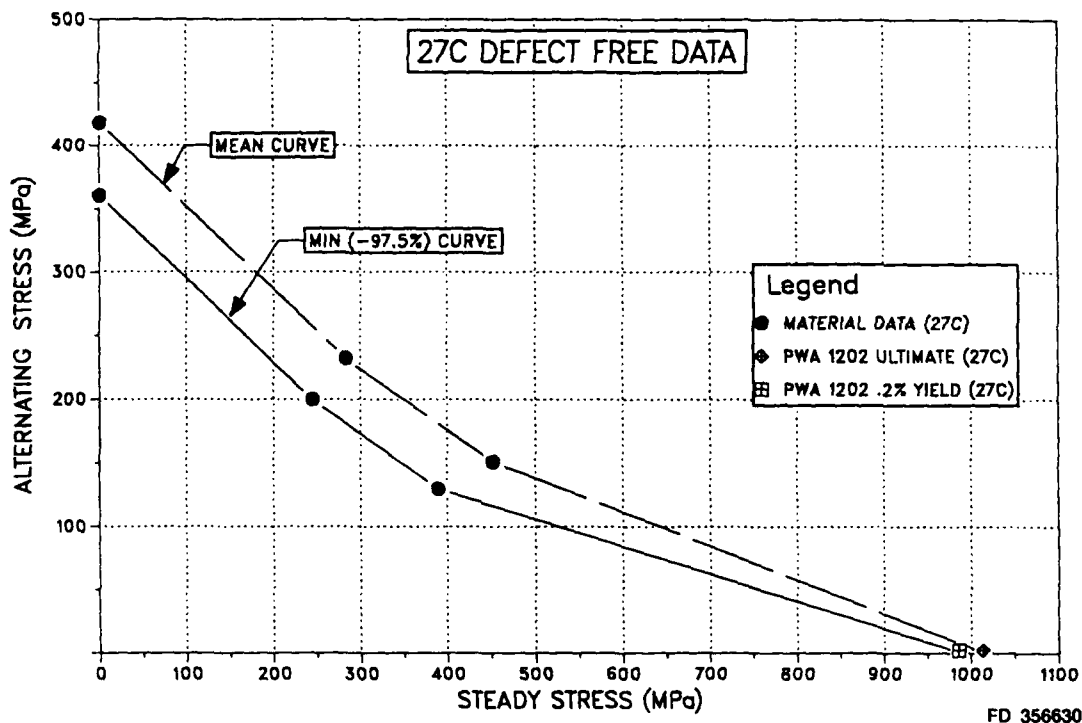
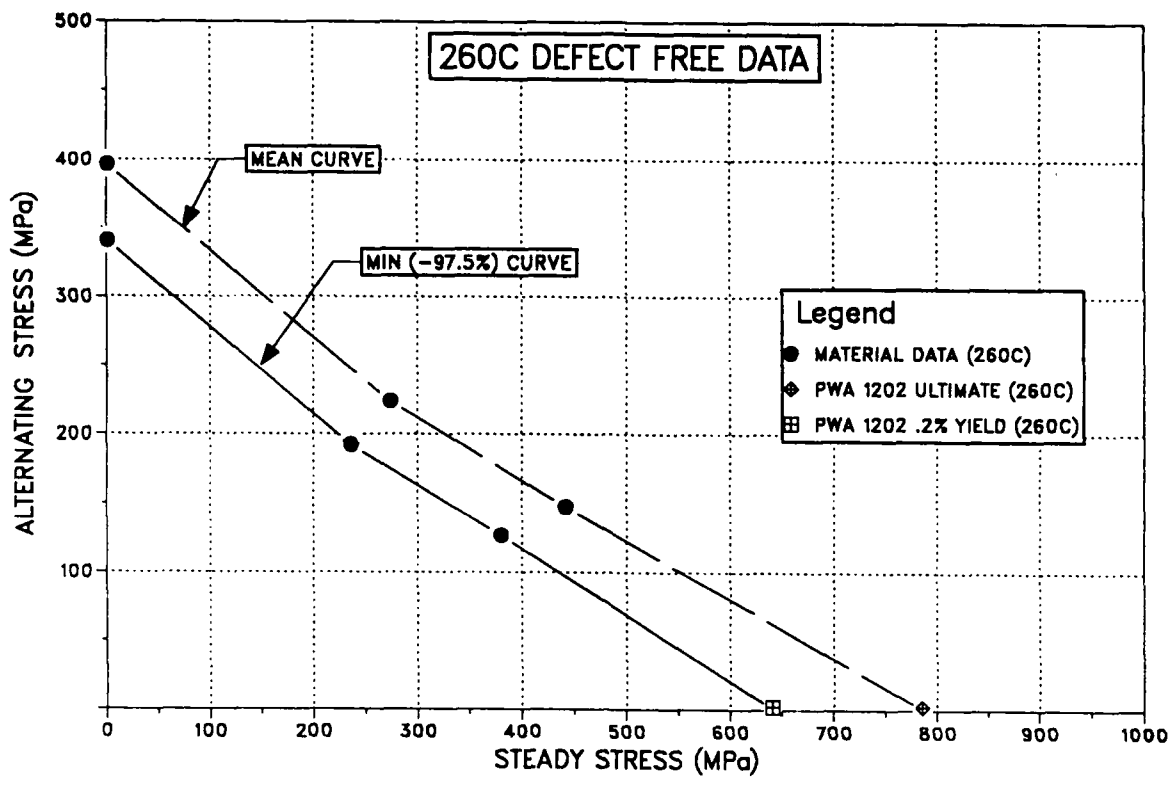


Figure 43. Modified Goodman Diagram For PWA 1202 at 27°C

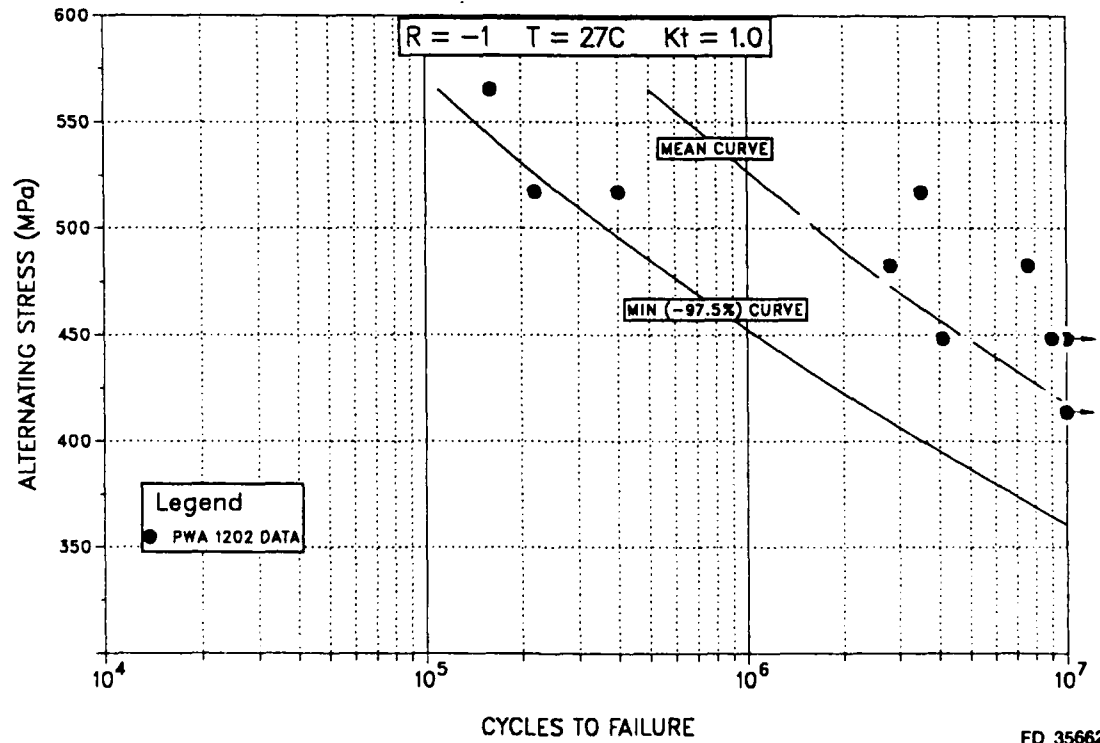
All the stress ratio data for a given temperature were regressed simultaneously according to equation (8), to generate the mean S-N curves. The minimum curves represent a -97.5 percent lower bound, which is commonly used for HCF design. The values of mean stress at zero alternating stress are defined as the material's monotonic ultimate and yield strengths, for the mean and lower bound curves, respectively. All of the test data used to generate the baseline Goodman diagrams are listed in Appendix C, Tables 1 and 2.

Two levels of damage were examined for the defect related Goodman diagrams, 0.20 mm and 0.38 mm. All damage testing was conducted at 260°C. The results of that testing are compared to the baseline Goodman diagram in Figure 51. The S-N behavior used to generate the defect related Goodman curves are given in Figures 52 through 54 for 0.2-mm defects, and Figures 55 through 57 for 0.38-mm defects. Specific test results are listed in Appendix C, Tables 3 and 4. Review of the defect related Goodman diagrams and S-N curves indicates that the HCF behavior is significantly degraded due to the presence of a notch, as would be anticipated. The 0.38 mm damage reduced the HCF capabilities to a greater degree than did the 0.20 mm damage.



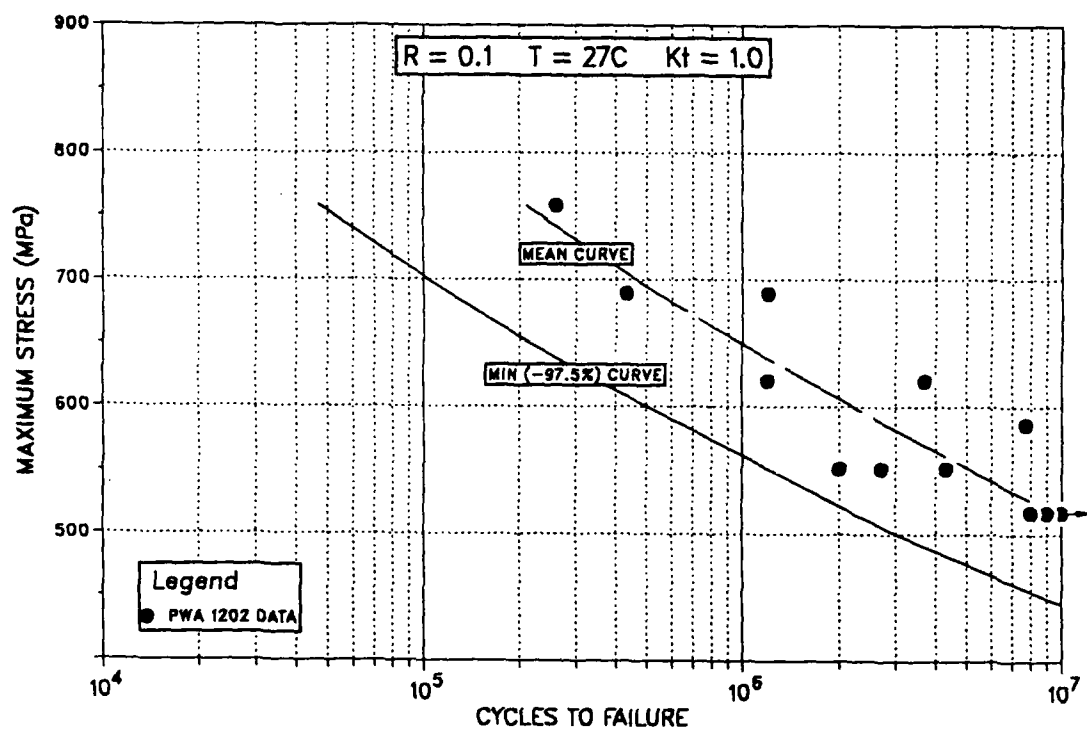
FD 356631

Figure 44. Modified Goodman Diagram For PWA 1202 at 500°C



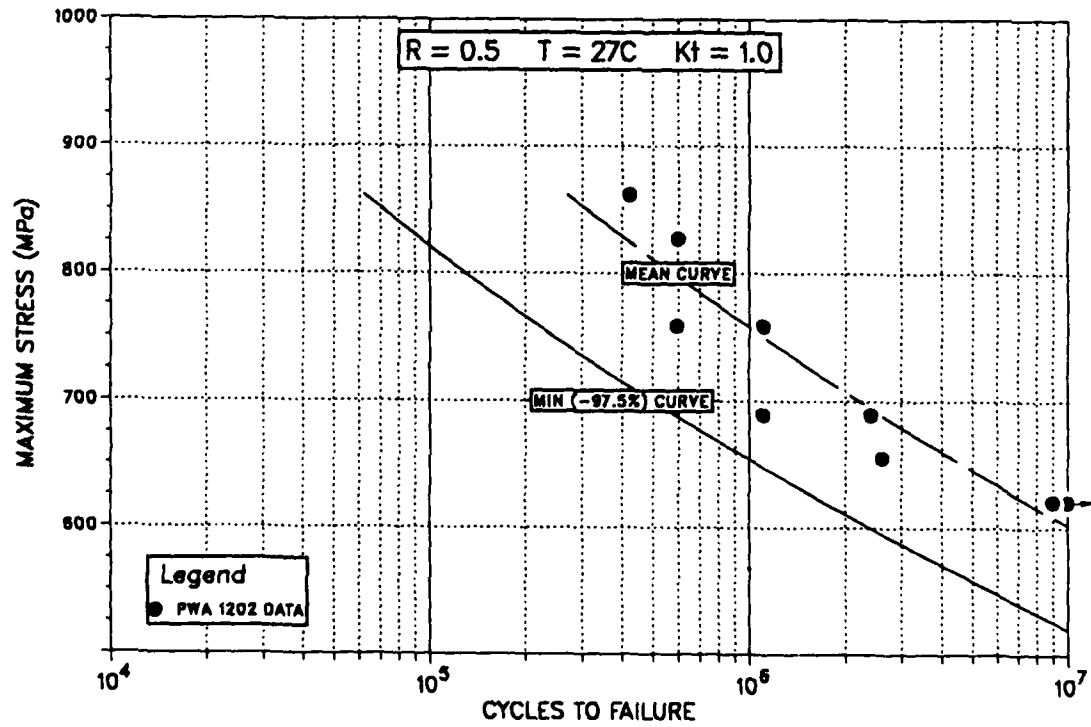
FD 356624

Figure 45. Axial High Cycle Fatigue Results for PWA 1202 at 27°C, $R = -1.0$, $K_t = 1.0$



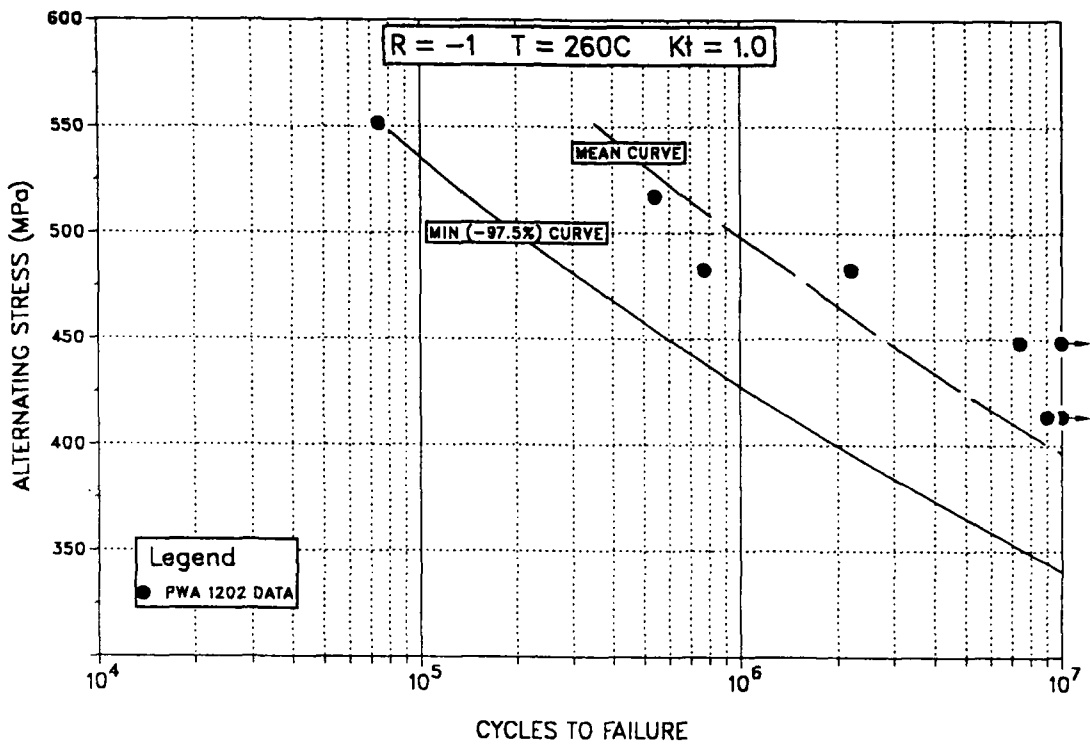
FD 356625

Figure 46. Axial High Cycle Fatigue Results for PWA 1202 at 27°C , $R=0.1$, $K_t = 1.0$



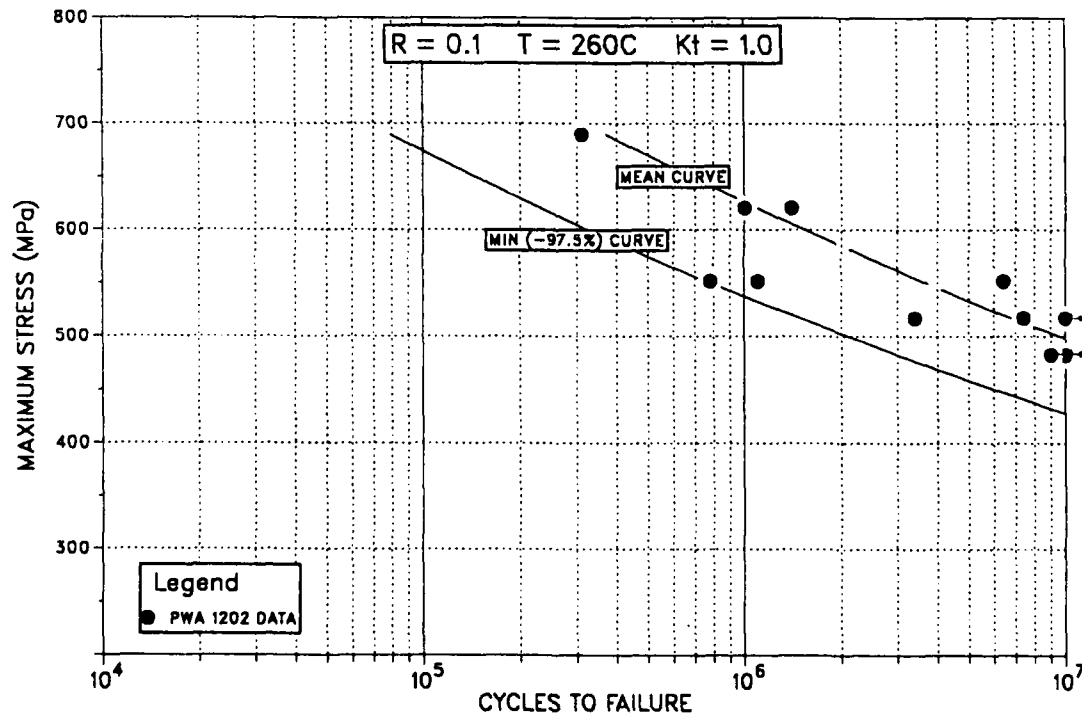
FD 356626

Figure 47. Axial High Cycle Fatigue Results for PWA 1202 at 27°C , $R=0.5$, $K_t = 1.0$



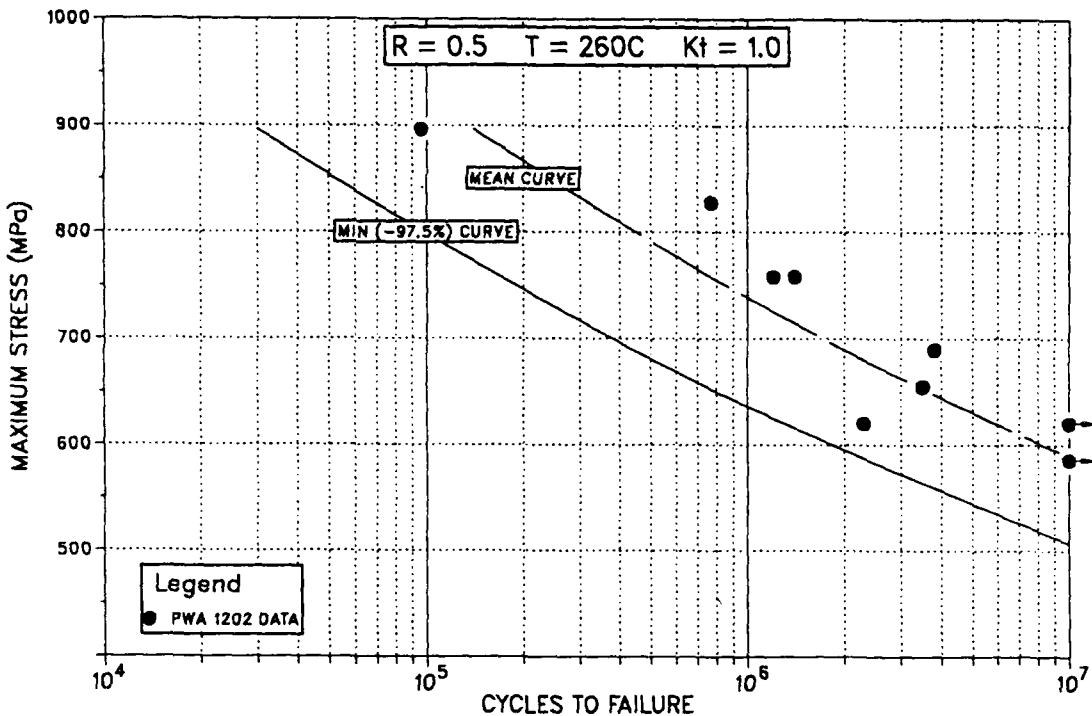
FD 356627

Figure 48. Axial High Cycle Fatigue Results for PWA 1202 at 260°C, $R=-1.0$, $K_t = 1.0$



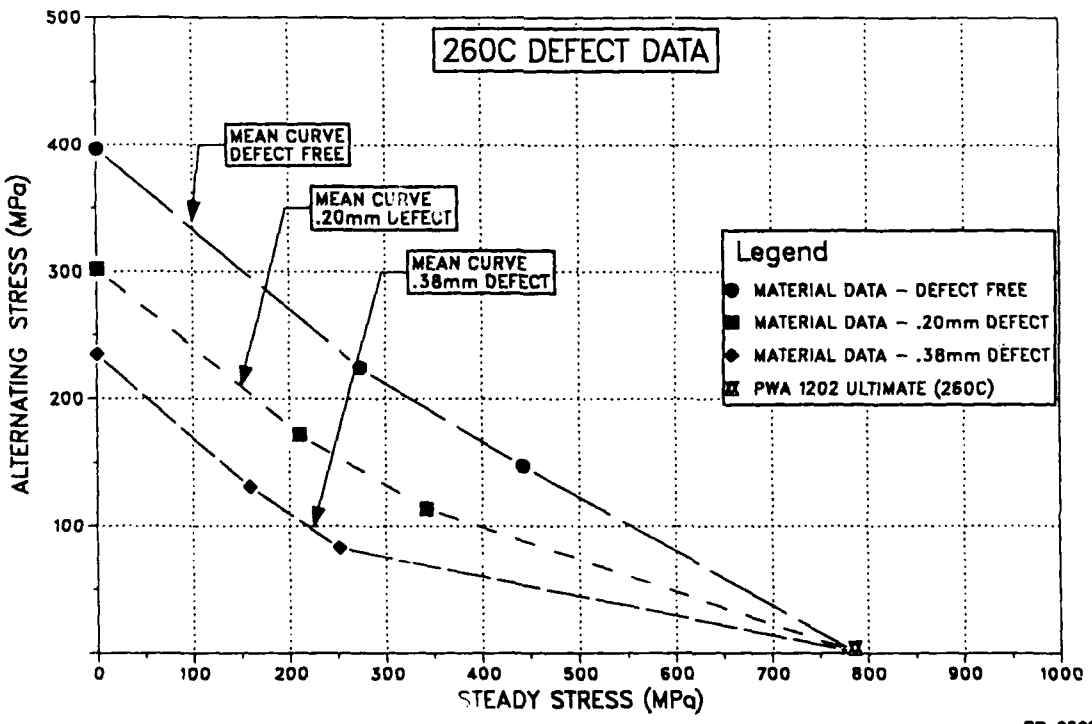
FD 356628

Figure 49. Axial High Cycle Fatigue Results for PWA 1202 at 260°C, $R=0.1$, $K_t = 1.0$



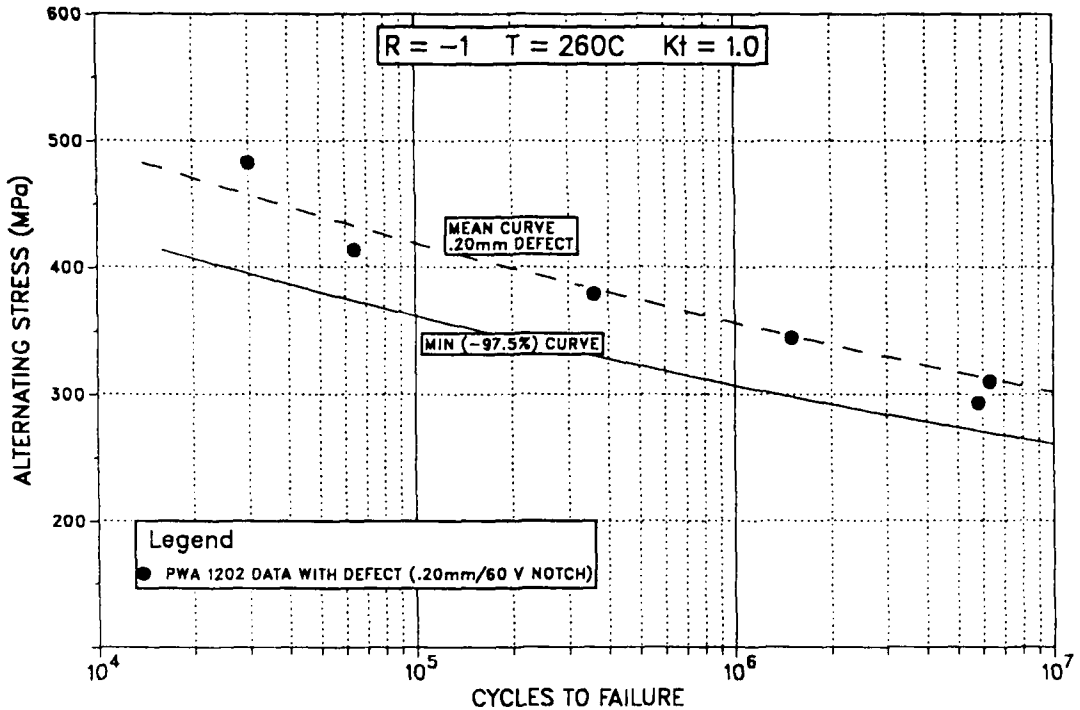
FD 356629

Figure 50. Axial High Cycle Fatigue Results for PWA 1202 at 260°C, $R=0.5$, $K_t = 1.0$



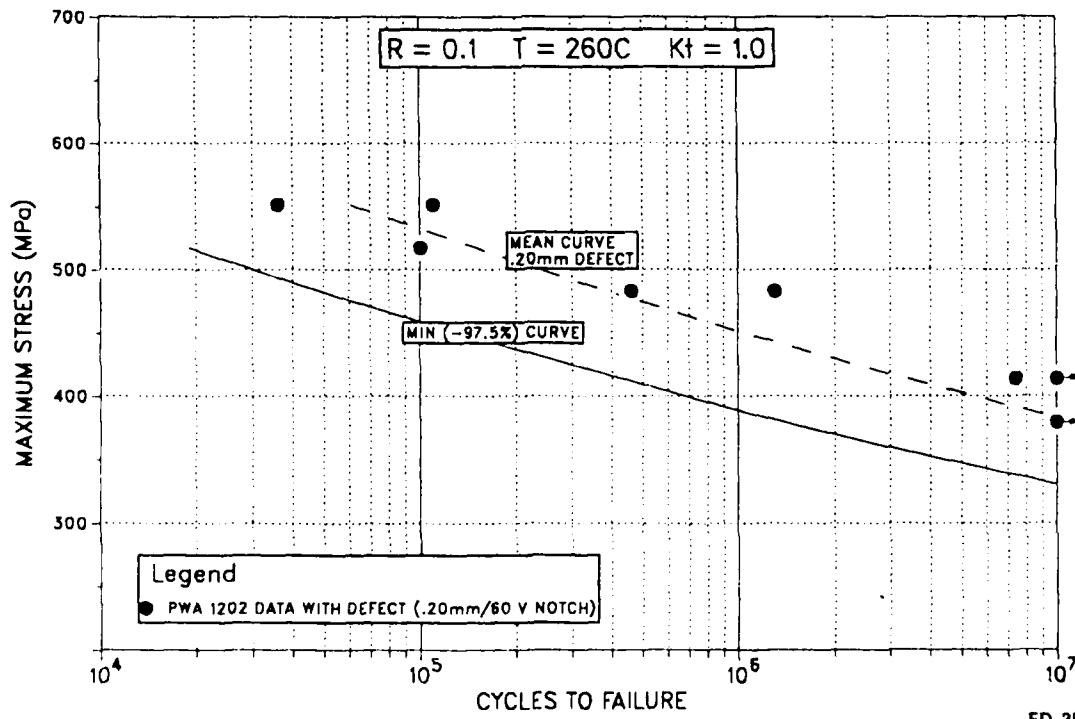
FD 356640

Figure 51. Modified Goodman Diagram for PWA 1202 at 260°C, Comparing Smooth, 0.2 mm Defect, and 0.38 mm Defect Specimens



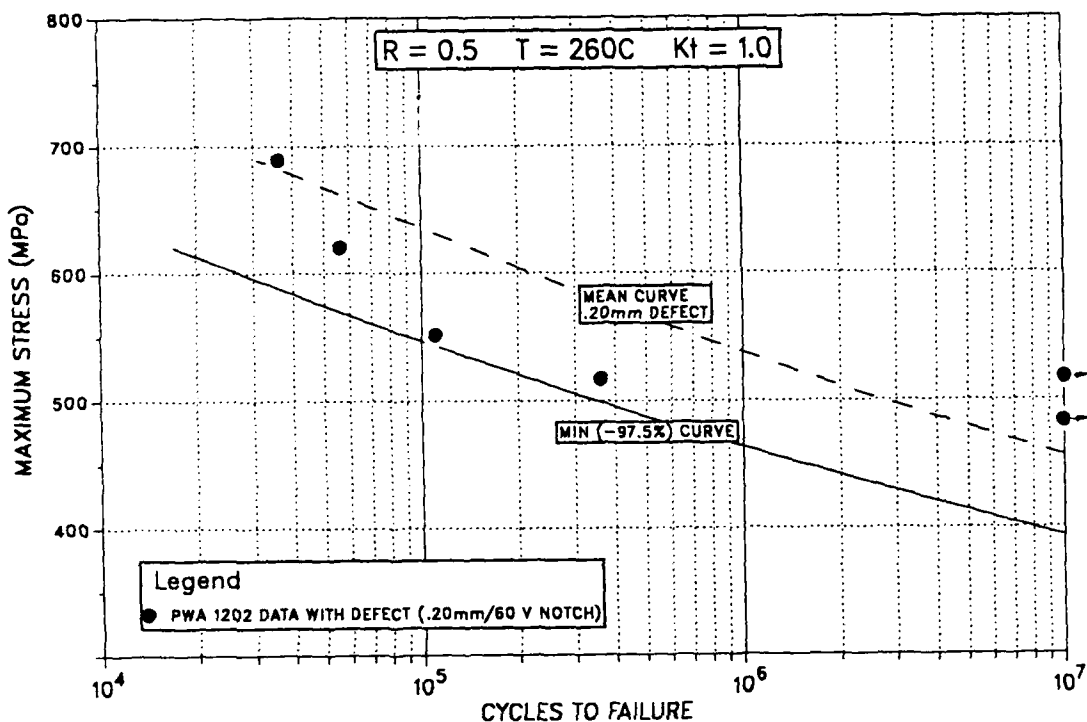
FD 356632

Figure 52. Axial High Cycle Fatigue Results for PWA 1202 at 260°C, $R=-1.0$, 0.2-mm Defect



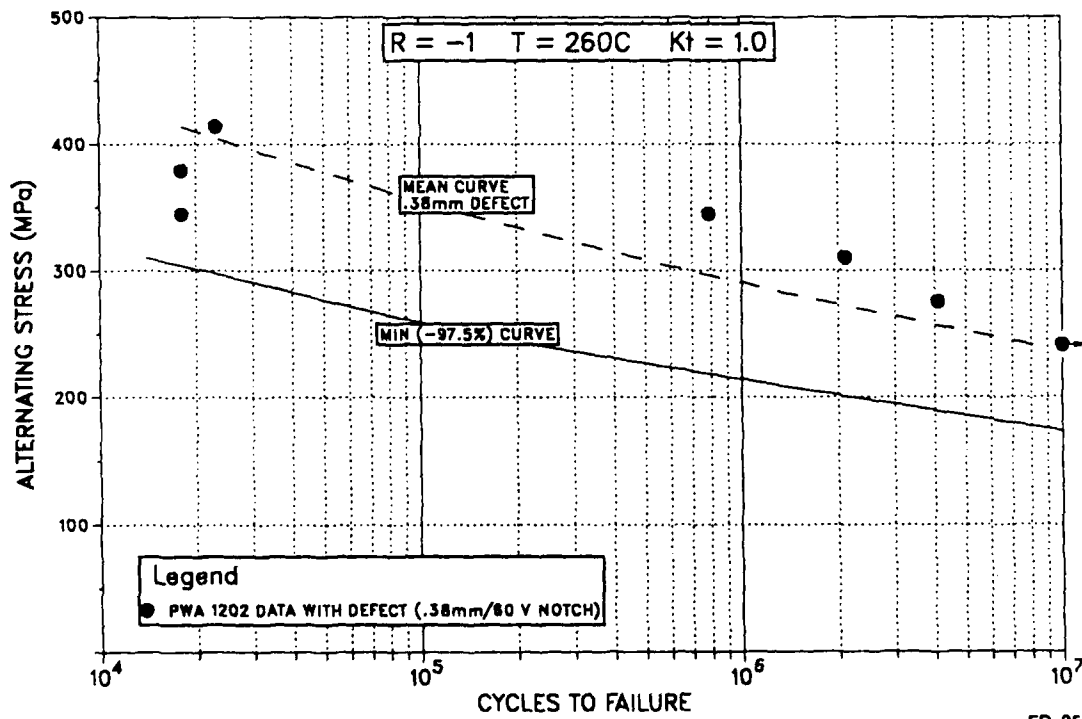
FD 356633

Figure 53. Axial High Cycle Fatigue Results for PWA 1202 at 260°C, $R=0.1$, 0.2-mm Defect



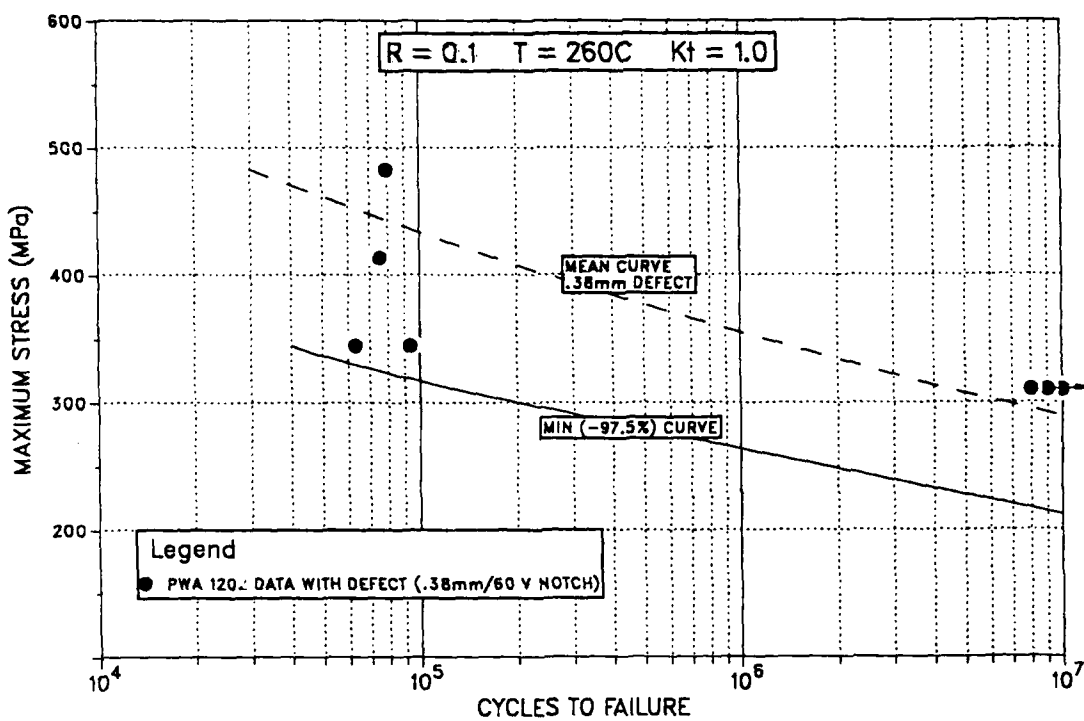
FD 356634

Figure 54. Axial High Cycle Fatigue Results for PWA 1202 at 260°C, $R=0.5$, 0.2-mm Defect



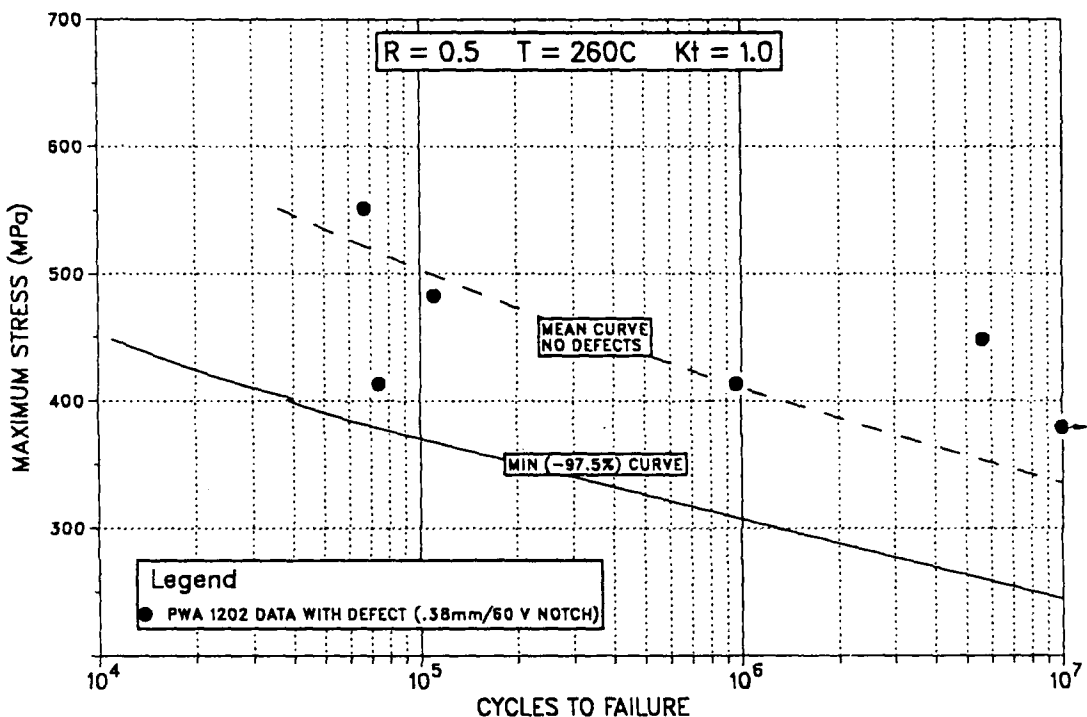
FD 356635

Figure 55. Axial High Cycle Fatigue Results for PWA 1202 at 260°C, $R=-1.0$, 0.38-mm Defect



FD 356636

Figure 56. Axial High Cycle Fatigue Results for PWA 1202 at 260°C, R=0.1, 0.38-mm Defect



FD 3556637

Figure 57. Axial High Cycle Fatigue Results for PWA 1202 at 260°C, R=0.5, 0.38-mm Defect

The 0.38-mm damage S-N data display a greater degree of scatter than either the 0.20-mm damage or the undamaged data. It appears that the larger scatter is due not to material behavior, but to notch reproducibility. Although these data have been reported as 0.20- and 0.38-mm notches, there is some variation in size associated with the notches. Included in Tables C3 and C4 are the actual notch depths measured on the fracture surfaces. As seen by those measurements, the 0.20-mm notches were more accurately reproduced than the 0.38-mm notches. It appears that the variation in the 0.38-mm notches was due, at least in part, to breaking the tip of the tool used to create the notches at impact. This is illustrated in Figures 58 through 61, which show typical notch geometries. The 0.20-mm notches are uniform and straight, similar to Figures 58 and 59. The 0.38-mm notches are straight in some cases, Figure 60, and irregular in others, Figure 61. If notch depth vs HCF life is compared for the 0.38 mm, a rough correlation can be established. However, since the final S-N curves appeared to be satisfactory. No attempt was made to segregate the test data by notch size.

HCF testing was also conducted using a cycle which included an intermittent dwell at mean load. Two stress ratios, $R = 0.5$ and $R = 0.7$, and one temperature, 260°C , were tested. The results of that testing are compared to baseline HCF behavior in Figures 62 and 63. The actual dwell data is given in Appendix C, Table C5. As indicated by those S-N comparisons, no change in HCF behavior is observed due to the introduction of the hold time. For $R = 0.5$, this is in agreement with the threshold data. At $R = 0.7$, however, the intermittent dwell cycle resulted in an increased ΔK_{th} . It may be that this increase in threshold is not apparent in the HCF data because the propagation life is a minor fraction of the total HCF life.



(a)

10X

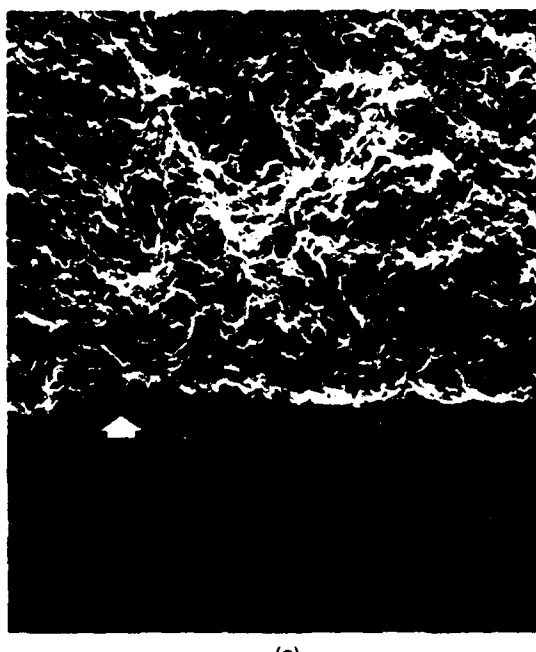


(b)

EC 10540 E II
10X

FD 345804

Figure 58. PWA 1202 HCF Fracture Surface, Tested With 0.20-mm Deep Sharp Notch at 260°C, R = 0.1, 30 Hz, and (a) 552 MPa or (b) 414 MPa



(a)

100X



(b)

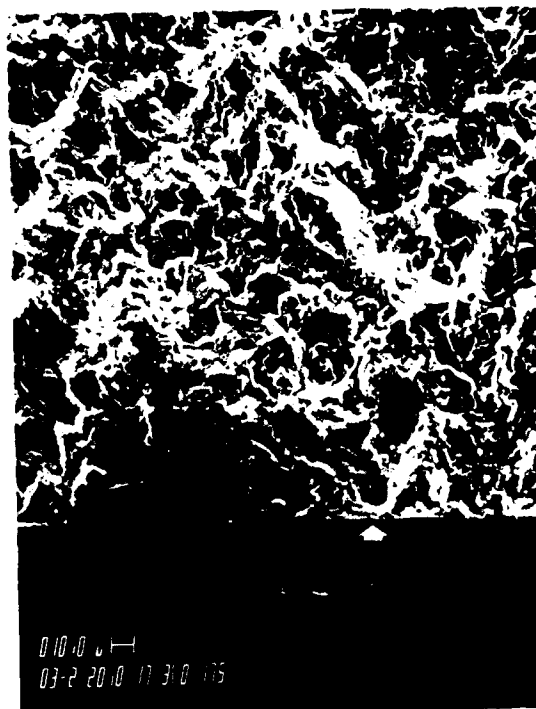
FC 105402 H
3000X

FD 345805

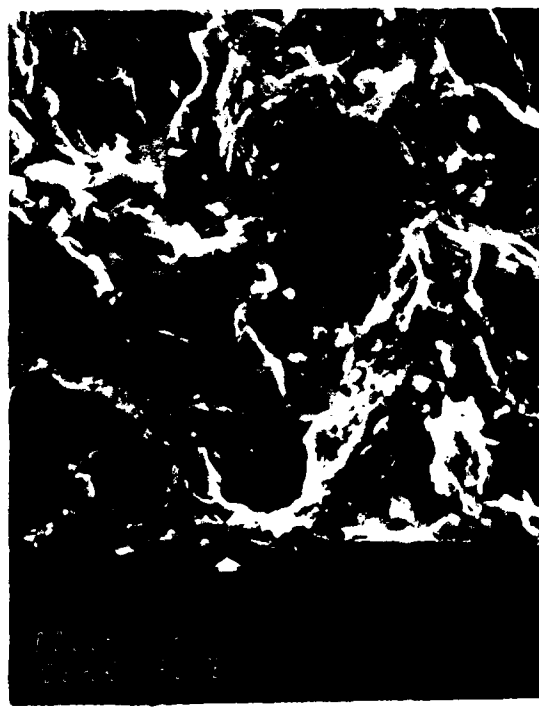
Figure 59. PWA 1202 HCF Fracture Surface, Tested at 260°C, R=0.1, 30 Hz, and 552 MPa, Arrow Indicates Probable Initiation Site at Notch



10X



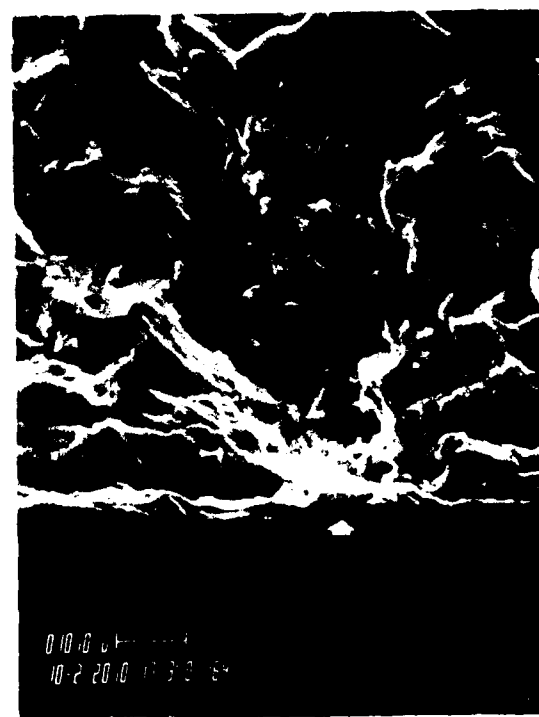
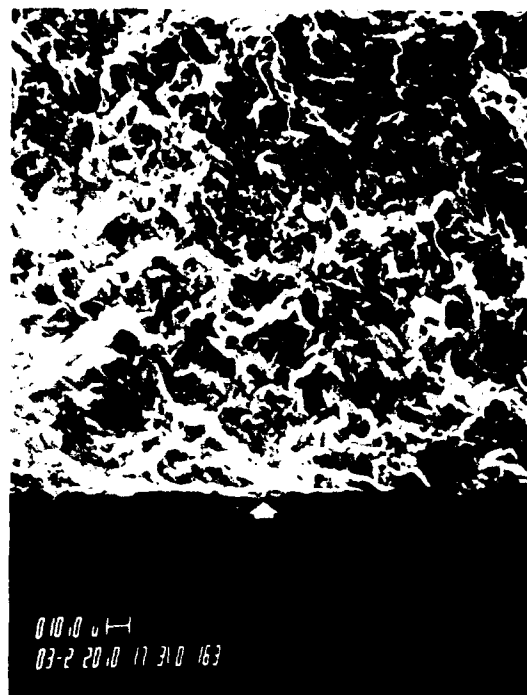
300X



1000X

FD 356648

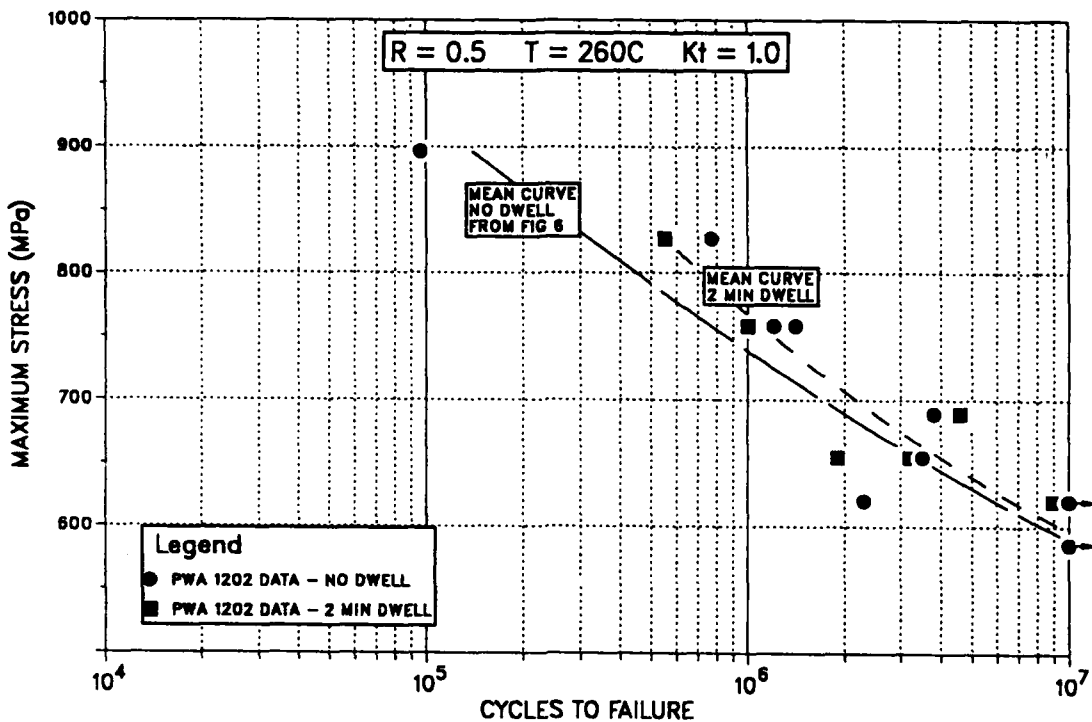
Figure 60. Notched HCF Specimen Fracture Surface. Tested At 260°C, R=0.1, σ_{max} = 414 MPa. Notch Depth Is 0.46 mm. Arrow Indicates Initiation Site At Base of Notch



1000X

FD 356649

Figure 61. Notched HCF Specimen Fracture Surface. Tested At 260°C, $R=0.1$, $\sigma_{max} = 483$ MPa. Notch Depth Is 0.28 mm. Arrow Indicates Initiation Site At Base of Notch



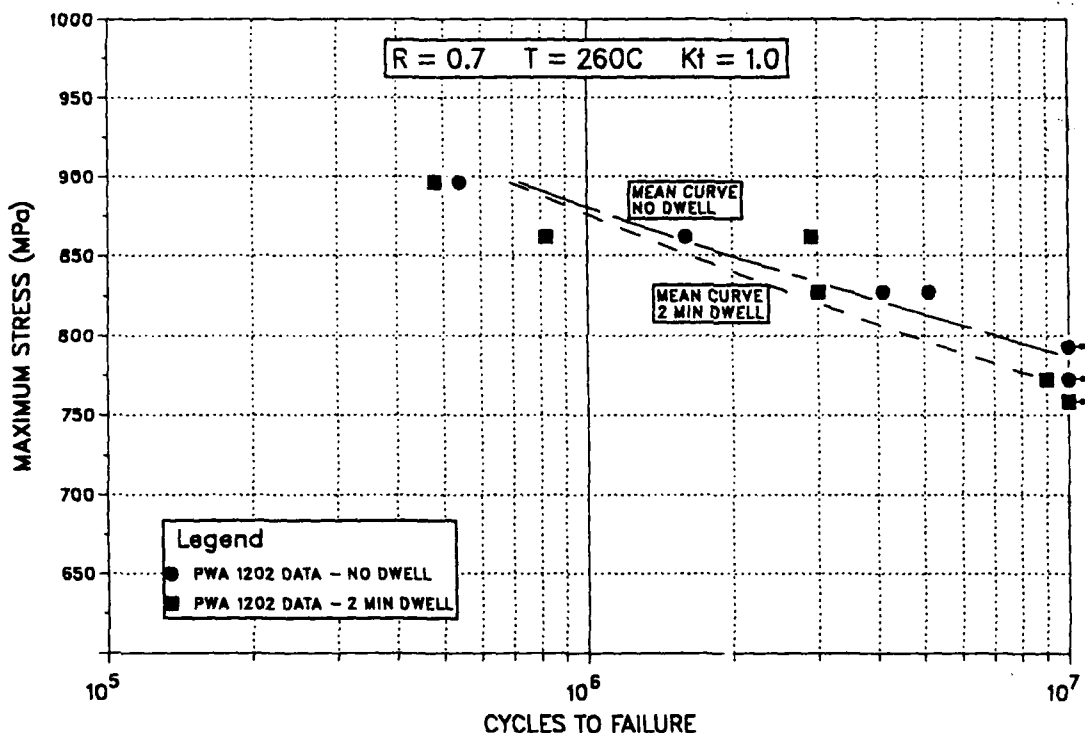
FD 356649

Figure 62. Axial High Cycle Fatigue Results For PWA 1202 at 260°C, R=0.5, K_t = 1.0, 30 Hz vs 30-Hz/2-min.-Dwell

Fractography

Scanning electron microscopy (SEM) and optical microscopy were used to examine the fracture surfaces of the failed HCF specimens. This study was conducted to identify and quantify the failure origins. That information was used to establish the defect distributions required in the analytical modeling task.

Fractographic examination of 27°C and 260°C HCF specimens revealed that specimens failed from surface connected origins. No particular material or machining defects were found at the initiation sites. Typical initiation sites for 27°C and 260°C specimens are shown in Figures 64 and 65, respectively. Generally, a small area of crystallographic, i.e., Mode I, cracking can be seen directly adjacent to the specimen surface. The fracture then transitions to a typical PWA 1202 HCF fracture surface dominated by cleavage of alpha particles. In the higher ΔK regions, striations can be observed, as indicated by Figures 65 and 66. The 260°C fracture surfaces displayed some degree of oxidation, but no heavy oxidation or oxide debris was in evidence. It was also observed that the low ΔK regions of the HCF fracture surfaces were quite similar to the low ΔK regions of the threshold specimens. Typical threshold specimen fracture surfaces are shown in Figure 67 for comparison.



FD 356639

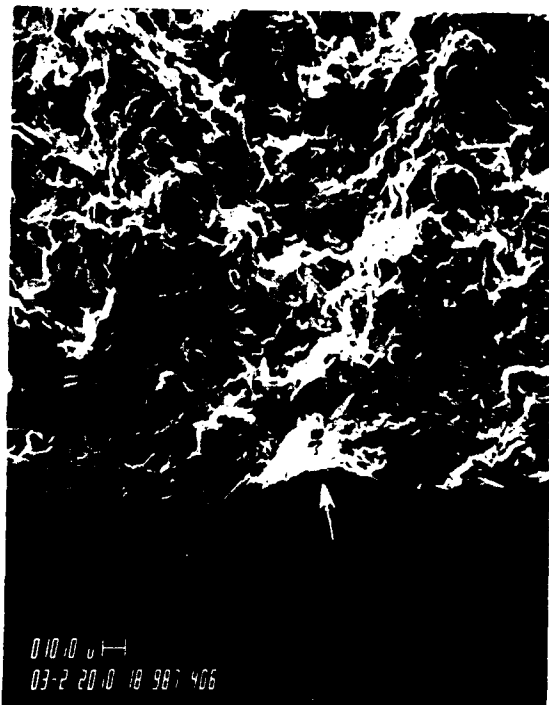
Figure 63. Axial High Cycle Fatigue Results For PWA 1202 at 260°C, $R=0.7$, $K_t = 1.0$, 30 Hz vs 30-Hz/2-min.-Dwell

The only exceptions to the surface initiations were HCF tests conducted at $R = 0.7$, both cyclic and cyclic/dwell. More than half the specimens tested at $R = 0.7$ initiated subsurface. However, none of the subsurface initiations was traceable to a specific defect. Much like the surface initiations, the fatigue cracks appear to emanate from crystallographically fractured alpha particles. The fracture surfaces shown in Figures 68 and 69 are representative of this behavior. Subsurface initiations were an unanticipated result, one that is thought to be atypical of actual blades. One possible explanation is small surface residuals from specimen machining. If these residuals are, in fact, present, the alternating stress at $R = 0.7$ may be insufficient to wash them out, as would occur at lower stress ratios. No attempt to validate that explanation was made. Since this behavior appeared to be nonrepresentative of engine components, the $R = 0.7$ data was not included in the Goodman diagrams.

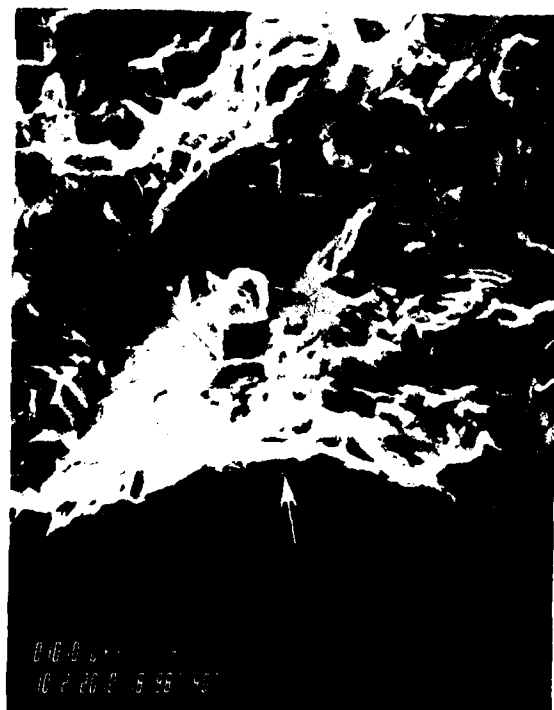
Fracture surfaces of notched specimens were reviewed to confirm the defect size and fracture mode. Typical fracture surfaces are shown in Figures 58 through 61. Review of the fracture surfaces in the immediate vicinity of the notch indicates that the notch was not behaving as a single crack during the initial cycles of the test. Although the initiation sites are not as obvious as in a smooth section test, it appears that there are one or more initiation sites along the bottom of the notch. Suspected initiation sites are shown in Figures 59 through 61. As was the case in the baseline tests, there are crystallographically fractured alpha particles at or near the point of initiation. Moving to a point further from the notch, the fracture surface is typical of HCF failures and displays fine striations as seen in Figure 70.



10X



300X



1000X

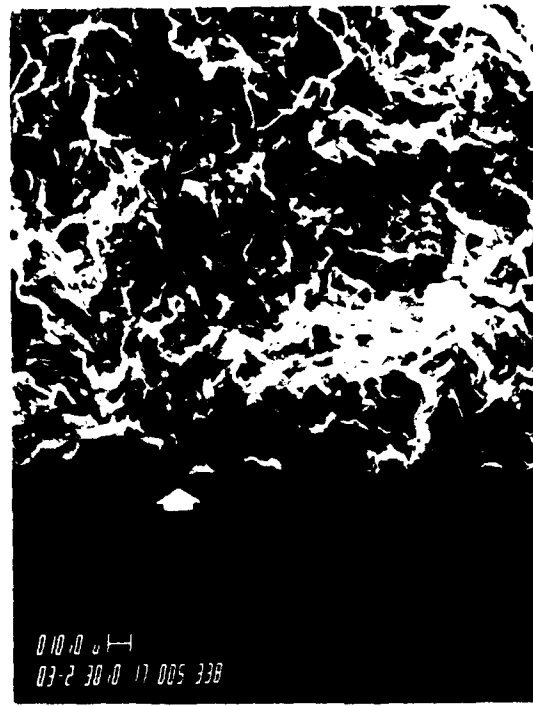
FD 324777

Figure 64. HCF Failure Origin Tested at RT, R=0.1, 548 MPa, Arrow Indicates Origin



a.

10X



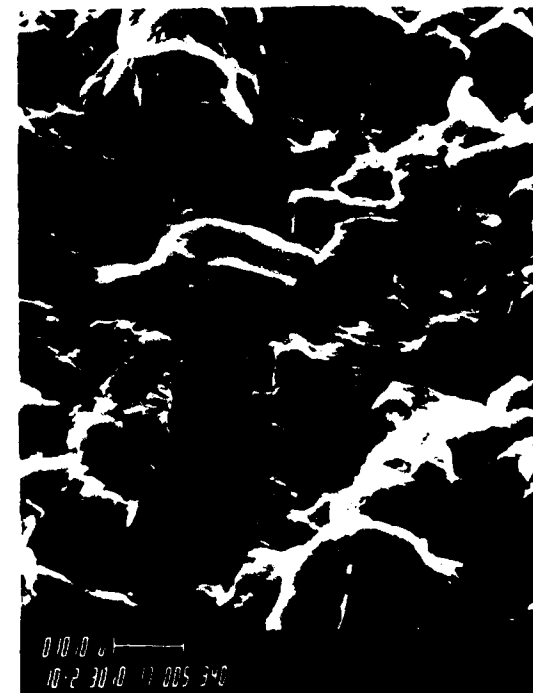
b.

300X



c.

1000X



d.

3000X

FD 324627

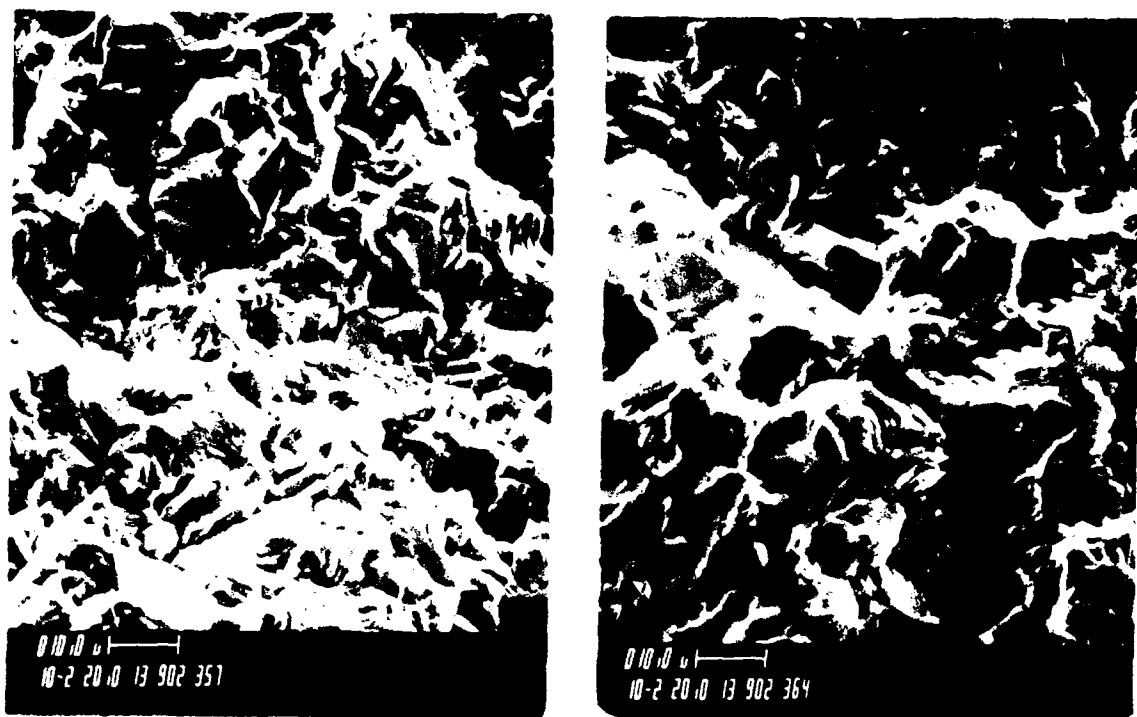
Figure 65. Smooth HCF Fracture Surface Tested at 260°C, R=0.1, $\sigma_{max} = 552$ MPa. For a-c, Arrows Indicate Fracture Origin; d shows Striations in High ΔK Region



2000X

FD 324629

Figure 66. HCF Fracture Surface Showing Fatigue Striations in High ΔK Region Tested at 27°C, 480 MPa



27°C

1000X

260°C

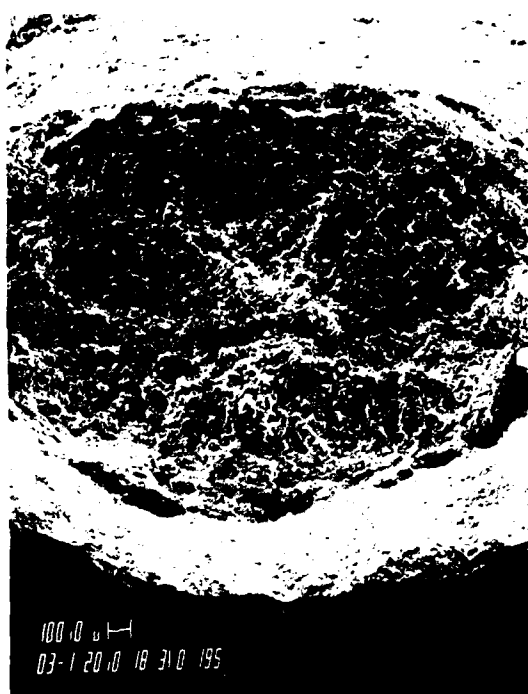
1000X

FD 324628

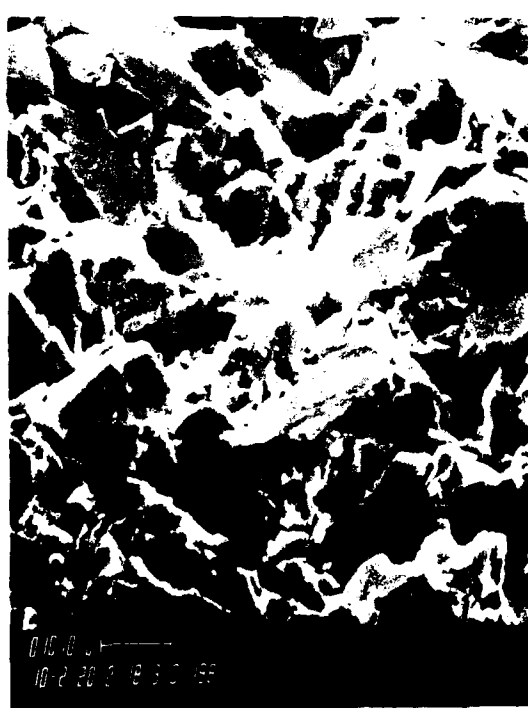
Figure 67. Threshold Specimen Fracture Surfaces; Area Adjacent to Pre crack



10X



30X



1000X

FD 356650

Figure 68. HCF Fracture Surface With Subsurface Initiation Tested at 260°C, R=0.7, 30 Hz, 828 MPa



10X



30X



1000X

FD 357451

Figure 69. HCF Fracture Surface With Subsurface Initiation Tested at 260°C, R=0.7, 30 Hz/2 Min-Dwell, 828 MPa



FC 105401 H
3000X

FD 345806

*Figure 70. HCF Fracture Surface: Area Removed From Notch Showing Fine Striations.
Tested at 260°C, R=0.1, 30 Hz, 552 MPa*

SECTION V

TASK IV — ANALYTICAL MODELING

1. MODEL DESCRIPTION

The methodology employed in this program is based on replacing fatigue limit stresses with fracture mechanics considerations in defining a Goodman diagram. The underlying assumption is that the crack propagation life from ΔK_{th} to failure will approximate the total fatigue life of the material. Using fracture mechanics tenets, ΔK_{th} , measured at varying stress ratios, can be related to allowable stress range through a simple stress intensity expression.

Raju and Newman (Ref. 8) provide a stress-intensity expression for a surface flaw in a cylindrical cross section which will be used in the form:

$$\Delta K_{th} = \Delta\sigma \sqrt{\pi a_i/Q} F \quad (9)$$

where:

- ΔK_{th} = threshold stress intensity range
- $\Delta\sigma$ = allowable stress range = $\sigma_{max} - \sigma_{min}$
- a_i = initial flaw size
- Q = shape factor = $1.0 + 1.464 (a/c)^{1.65}$
- a/c = crack aspect ratio
- F = boundary correction factor.

Raju and Newman define F in tabular form. A polynomial curve was fitted to that data to facilitate calculations, resulting in the expression:

$$F = 1.00851 + 3.85675 (a/D)^3 \quad (10)$$

where:

- D = specimen diameter.

The crack size, a_i corresponds to either intrinsic damage, IMQ, or extrinsic damage, FOD. However, this damage is not single valued. There exist statistical distributions of sizes, which will be discussed in the following sections. Since a_i can vary over a prescribed range, as dictated by the statistics of the distributions, so must the stresses vary, according to equation (9), such that the resulting ΔK_{th} remains constant.

A simple Monte Carlo simulation, described in Appendix D, samples from the defect distribution and computes the mean, σ_m , and alternating, σ_{alt} stresses as follows:

Rearranging equation (9):

$$\Delta\sigma = \Delta K_{th} / \sqrt{\pi a_i/Q} F$$

$$(1-R) \sigma_{max} = \Delta K_{th} / \sqrt{\pi a_i/Q} F$$

$$\sigma_{\max} = \frac{\Delta K_{th}}{(1 - R)} \frac{1}{\sqrt{\pi a_i/Q F}} \quad (11)$$

$$\sigma_m = (\sigma_{\max} + \sigma_{\min})/2 \quad (12)$$

$$\sigma_{alt} = \Delta\sigma/2. \quad (13)$$

Using the applicable defect distributions, and the measured values of ΔK_{th} at various stress ratios, these calculations can be performed to generate fracture mechanics-based Goodman diagrams.

As mentioned above, a probabilistic approach is used to define the required initial flaw sizes. This approach uses defect distributions in place of a single characteristic damage size. Three distributions have been quantified: one representing initial material quality, IMQ, for Ti 8-1-1, and two representing different levels of foreign object damage (FOD), likely to be experienced by fan and compressor blades. The IMQ information was obtained from fractographic examination of failure origins on HCF specimens. FOD data were obtained from hardware inspections during engine teardowns at the San Antonio Air Logistics Center, SA-ALC and were supplemented with FOD information from ongoing programs at P&W.

2. RESULTS

A number of fan and compressor blades were inspected at the F100 engine overhaul facility at SA-ALC. The purpose of the inspections was to review and quantify blade FOD in field hardware. The FOD data could then be used to establish initial damage criteria for blade life calculations. Approximately 900 2nd- through 7th-stage fan and compressor blades were examined. All the blades inspected were Ti 8-1-1, PWA 1202, except for the 7th-stage blades which were Ti 6-2-4-6. One hundred sixty-two occurrences of FOD were found and documented on 14 fully bladed disks. This FOD commonly ranged in depth between 0.076 mm and 1.27 mm, and was considered to be repairable in all cases. To quantify more severe levels of damage, 30 non-repairable blades were randomly selected for inspection. These blades were not associated with one particular engine or rotor set. They all displayed heavy FOD, up to a depth of 5.1 mm. A total of 104 FOD occurrences were documented for those blades.

The FOD information collected on repairable and non-repairable blades is summarized in Tables 5 and 6, respectively. All observations are based on simple visual inspection of 2nd- through 7th-stage blades. Since the damage levels appeared to be roughly equivalent for all stages, no attempt was made to segregate FOD by stage.

The FOD information in Tables 5 and 6 has been analyzed to produce the cumulative distribution functions shown in Figures 71 and 72, respectively. As indicated by those figures, the repairable blade FOD is represented by a Weibull distribution and non-repairable blade FOD by a lognormal distribution. Those particular distribution functions have also been used successfully in other probabilistic life analyses requiring descriptions of initial material quality.

TABLE 5. FOD Size Distributions for Repairable Blades

FOD Depth (mm)	Number of Occurrences
0.051	28
0.076	11
0.102	6
0.127	20
0.152	6
0.178	14
0.203	11
0.229	1
0.254	18
0.279	6
0.305	11
0.330	4
0.356	1
0.381	13
0.406	0
0.432	1
0.457	1
0.483	1
0.508	2
0.533	0
0.559	0
0.584	1
0.610	0
0.635	2
0.660	0
0.686	0
0.711	0
0.737	0
0.762	1
0.787	0
0.813	1
1.016	1
1.270	1

R20431/1

TABLE 6. FOD Size Distributions for Non-Repairable Blades

FOD Depth (mm)	Number of Occurrences
0.076	4
0.076 to 0.254	17
0.279 to 1.270	55
1.295 to 2.540	14
2.565 to 5.080	6
5.080	8

R20431/1

The FOD distributions described above address only damaged blades. A complete life prediction model must also consider undamaged blades. For the purposes of this model, the HCF specimens will be considered representative of undamaged blade material. Testing has indicated that the vast majority of the HCF specimens fail from surface-connected origins, with no indication of material or machining defects. As discussed earlier, the fracture appears to originate from an alpha particle that fractures crystallographically. Therefore, the size of these particles will be used to estimate an initial flaw size. An SEM examination of the failed HCF specimens, confirmed by optical metallography, indicates that the nominal size of these particles is 8 to 12

microns. Further, the size distribution appears to be skewed right, with some particles as large as 20 microns. A lognormal distribution shown in Figure 73 provides a reasonable description of those sizes. That distribution is used for an approximation of initial flaw sizes for the case of undamaged material.

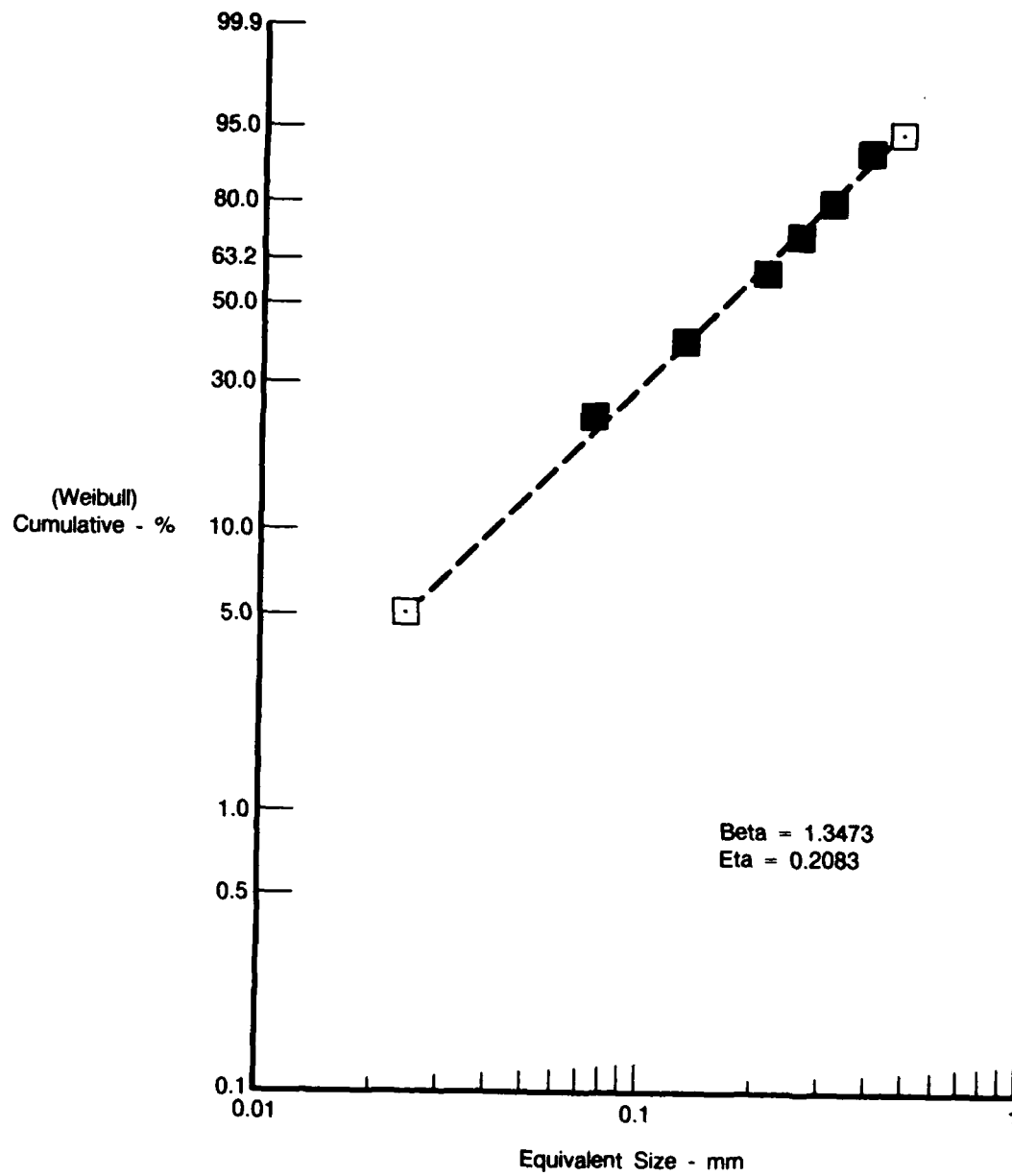


Figure 71. Repairable FOD Distribution

FDA 357477

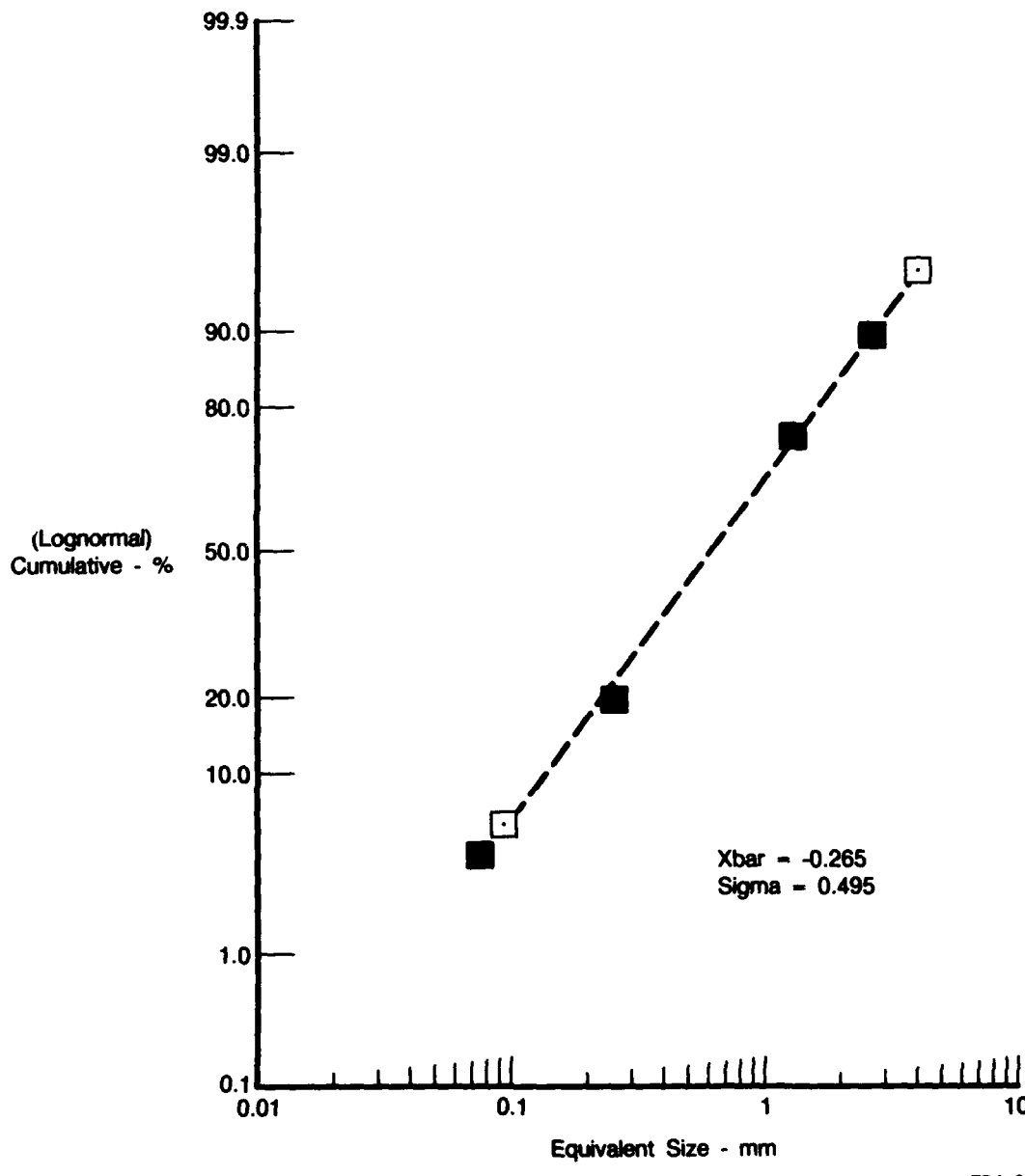


Figure 72. Non-Repairable FOD Distribution

The relative frequency of sampling between the damaged and undamaged material distributions has been established by examining the number of FOD occurrences in the total number of blades inspected at SA-ALC. This analysis includes a large inspection data base generated for the Manufacturing Technology for Advanced Propulsion Materials program, AFWAL/MLTM Contract No. F33615-85-C-5152. Seventy-seven compressor rotors were examined, and data were obtained from nearly 33,000 blades. Although specific size measurements were not made, the FOD was divided into two groups: (1) those less than 0.076 mm deep, and (2) anything larger. This grouping allows the data to be used with the FOD defect distribution required for this contract. A summary of these findings is presented in Table 7.

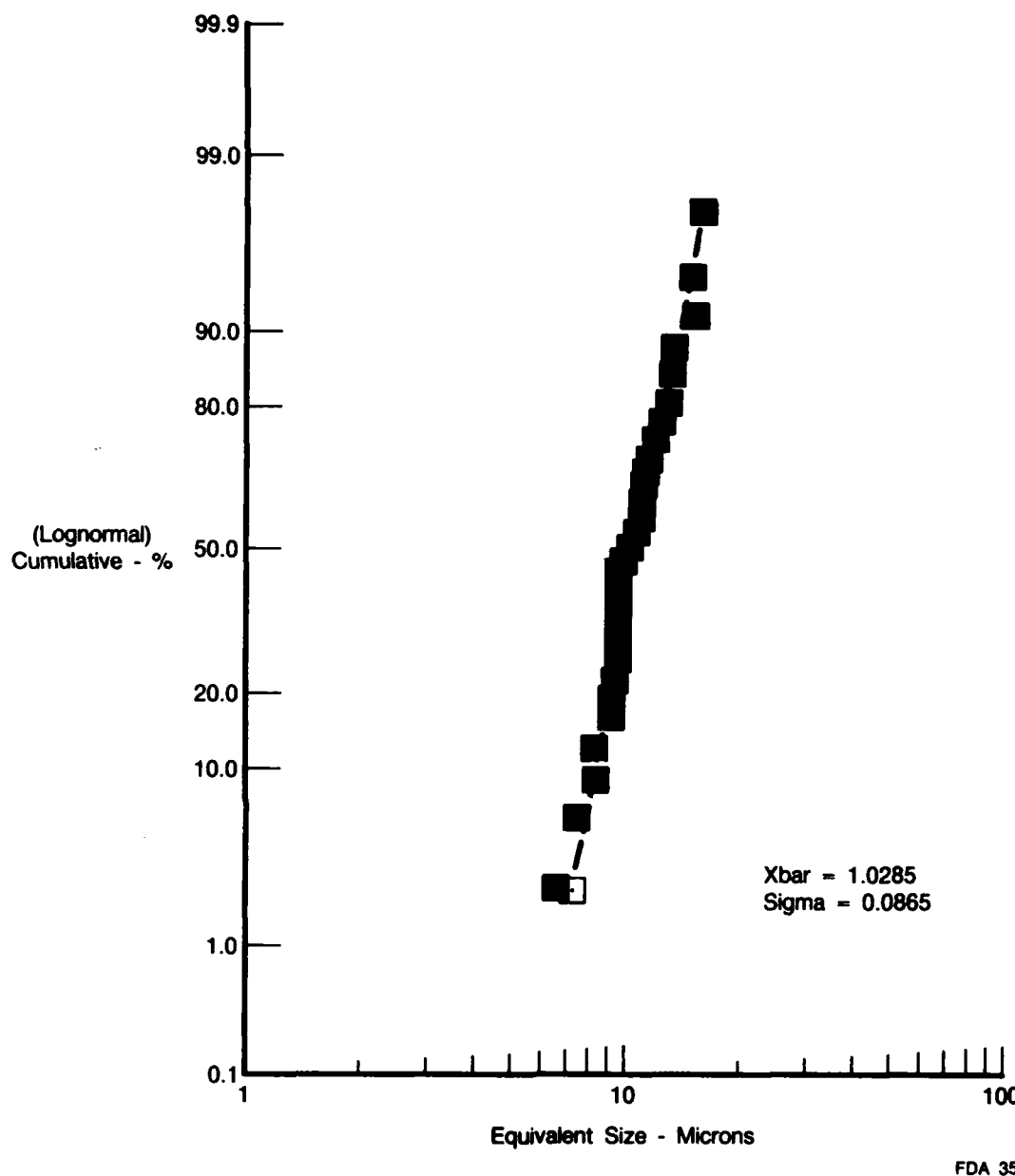


Fig 73. Ti 8-1-1 IMQ Distribution

TABLE 7. Summary of FOD Sampling

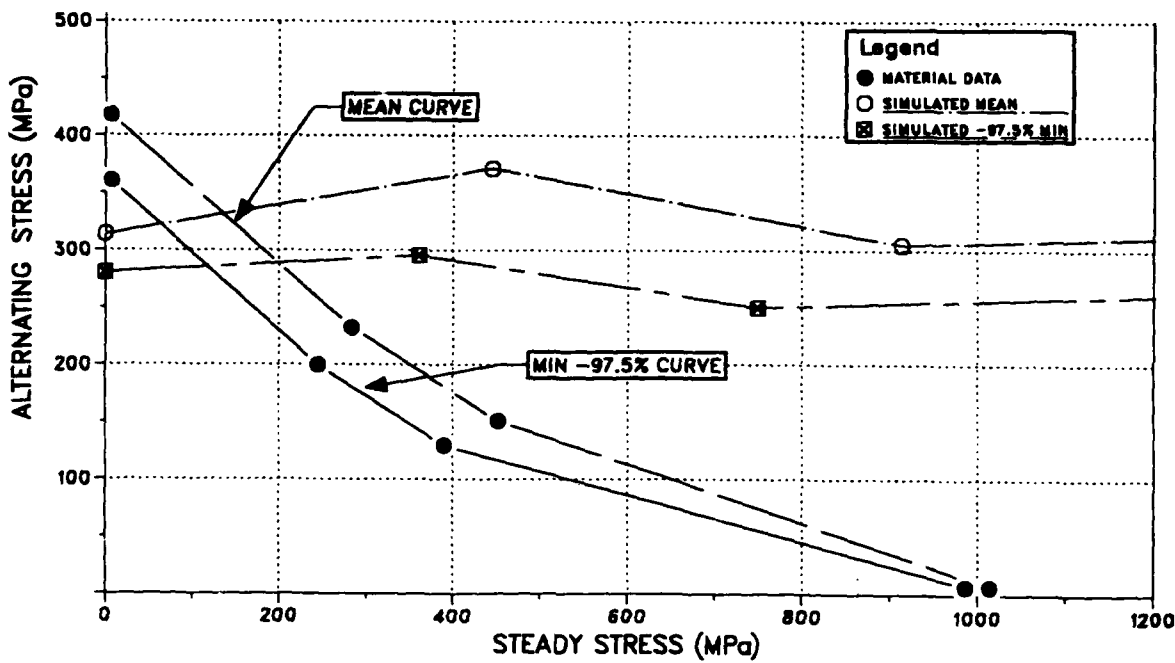
	5th Stage	6th Stage	7th Stage	8th Stage	9th Stage	Total
Damaged Blades	336	365	366	94	159	1,320
Blades Inspected	5,250	6,450	6,600	7,200	7,050	32,550

Notes: 1. 77 rotors were evaluated. Two of which were completely destroyed.
 2. On the 75 remaining rotors, only four blades were beyond repair.

R20431/1

Using equations (11) through (13), the IMQ defect distributions, and the mean values for ΔK_{th} from the K -increasing tests, allowable stresses were calculated for an estimated Goodman

diagram. In the stress intensity expression, a/c was assumed equal to 1.0. This assumption is supported by the IMQ fractography presented earlier, and by the observation that this calculation is relatively insensitive to small changes in a/c . The results of those calculations are shown in Figures 74 and 75.



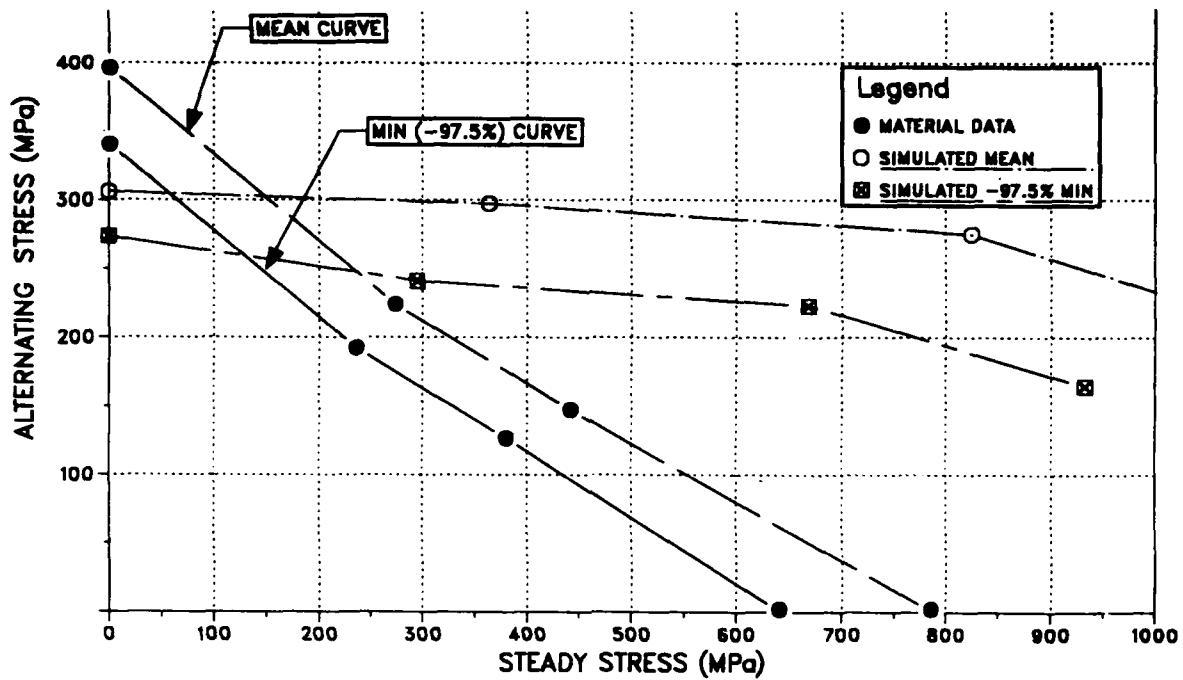
FDA 357480

Figure 74. Fracture Based Goodman Approximation vs HCF Test Data at 27°C

It is immediately evident from Figures 74 and 75, that this approach is unsuccessful in approximating the Goodman relationships. The fracture-based Goodman line is nearly horizontal. This results from the near constant value of ΔK_{th} versus stress ratio. Further, the 'allowable' stresses differ in magnitude from those generated with smooth HCF specimens.

The lack of stress ratio effect on ΔK_{th} poses a major problem in producing Goodman diagrams from threshold information. It is readily apparent from equation 11, that repeating these calculations using the ΔK_{th} values generated from CT specimens, (which are larger in magnitude but display a stress ratio trend), would result in higher calculated allowable stresses and larger errors for positive stress ratios. At least the stress ratio trend would appear to be more representative of the HCF data. On a Goodman diagram, curves further from the origin correspond to lives smaller than those closer. In this instance the implication is that lives associated with ΔK_{th} behavior are less than 10^7 cycles, yet the definition of threshold (as a value of applied stress intensity below which no crack advance occurs) would indicate infinite life.

Clearly there is a difficulty here. Now, if the total life of the smooth specimen consists of both the crack growth stage previously discussed and some initiation time prior to the existence of a crack-like defect, then the gross disagreement of the smooth specimen HCF results, and the pseudo-Goodman line can be explained, at least in part.



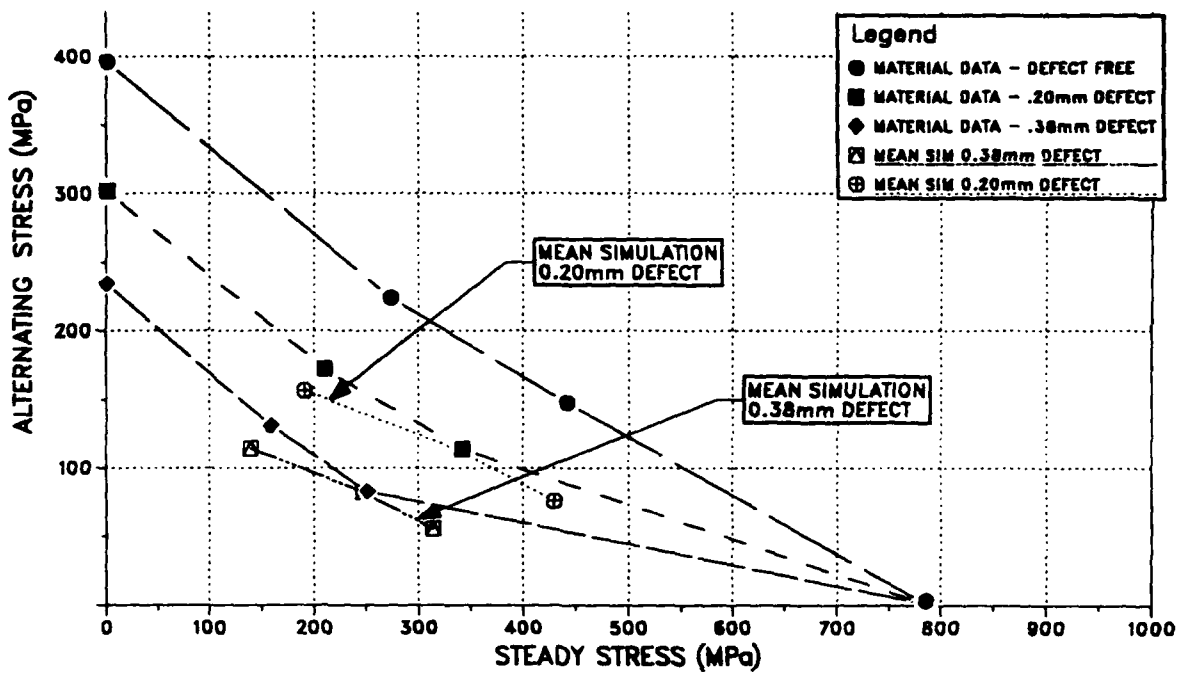
FDA 357481

Figure 75. Fracture Based Goodman Approximation vs HCF Test Data at 260°C

If initiation time is a major source of error, then the behavior of specimens subjected to extrinsic damage should agree more closely with the corresponding fracture based calculations. In these instances the distributions of crack size, a_i , correspond to sizes associated with repairable FOD and non-repairable FOD described previously.

Figure 76 compares results of specimens subjected to a 0.20-mm sharp notch, with threshold-based calculations using a Weibull distribution of sizes centered about that size, (and therefore representative of repairable FOD). Figure 76 makes the same comparison for a nominal notch size of 0.38 mm and the non-repairable FOD distribution. In both instances, the distributions were sampled in such a manner as to reproduce a mean flaw size equivalent to the appropriate notch depth. ΔK_{th} data from CT specimens were used to impart a reasonable stress ratio trend to the estimates. (Using $\Delta K_{th,eff}$ or ΔK_{th} from bend specimens would flatten the curve and reduce the allowable stresses.)

As indicated by these figures, the Goodman approximations for the notched geometry are improved as compared to the undamaged material. However, they still cannot be considered accurate representations of the actual HCF behavior. One interpretation of these observations is that the diminished contribution of initiation to total life in the damaged specimens allows a more accurate representation by threshold modeling.



FDA 357482

Figure 76. Simulated Goodman Diagrams vs HCF Test Data for Defect Containing Specimens at 260°C

Another possible source of error is the initial crack size. This is particularly true of the undamaged material since it is not possible to ascertain directly when the damage/defect is behaving as a fatigue crack. (Recall that the alpha particle size was chosen as a transition point between crystallographic (Stage I) and fatigue (Stage II) crack growth.) In an attempt to segregate sources of error, back calculations of crack propagation life into the near-threshold region were performed. Obviously, the basic calculation employed was an integration of a crack growth rate model. An HCF specimen was used as a model geometry. The crack growth rate data were taken from the CT tests described earlier. The stress range was held constant at the fatigue limit. The life was calculated based on an integration between ΔK_i and ΔK_c (estimated from crack growth rate data), with the actual numerical integration being performed on increments of crack length, a . Crack length and stress were related to stress intensity through the Raju and Newman K-solution detailed above. Crack aspect ratio was held constant at 1.0, except for the notched cases where it was allowed to vary, starting at $a/c = 0.33$. Integrations were performed using both ΔK and ΔK_{eff} . In most instances, the crack growth rate model employed was a SINH curve, although some ΔK_{eff} data was represented by two-piece Paris equations. The integrations were performed using Simpson's rule with a subregion in the near-threshold region broken into fine increments, since that area represents the majority of the cyclic life. For the cases requiring variable a/c , a cycle-by-cycle integration was performed.

The results of the calculations are summarized in Table 8. That table contains several variations on the life estimation schemes. First, lives and initial flaw sizes were calculated by integrating between ΔK_i and ΔK_c at a stress equal to the fatigue limit. This was done for crack growth rate data with and without correction for closure. In all cases, the life estimates were far below the anticipated value of 10^7 cycles. The closure corrected crack growth rate data gave reasonable estimates of the initial crack size, a_i which was established by fractography to be about 0.01 mm. The uncorrected crack growth rate gave much larger estimates of a_i .

TABLE 8. Integrated Life Summary

Test Condition and Integration Parameters	σ_{max} (MPa)	ΔK_i (MPa \sqrt{m})	ΔK_c (MPa \sqrt{m})	a_i (mm)	N (cycles)
27°C, R=0.1	517.				
ΔK		5.6	33.	0.1118	4.1×10^5
ΔK_{eff}		2.1	24.	0.0152	1.5×10^5
260°C, R=0.1	496.				
ΔK		5.2	27.	0.1041	2.3×10^5
ΔK_{eff}		2.2	27.	0.0178	2.3×10^5
ΔK_{eff} (Forced 10^7 life)		1.4	27.	0.0076	1.0×10^7
260°C, R=0.5	607.				
ΔK		3.5	27.	0.1041	3.1×10^5
ΔK_{eff} (Bend)		2.1	27.	0.0356	8.7×10^7
ΔK_{eff} (CT) (8% Closure)		2.9	27.	0.0686	2.1×10^5
ΔK_{eff} (Forced 10^7 life)		2.3	27.	0.0432	1.0×10^7
260°C, R=0.7	648.				
ΔK		2.5	22.	0.1295	6.0×10^5
ΔK_{eff} (Forced 10^7 life)		2.1	22.	0.0838	1.0×10^7
<i>Notch Data</i>					
260°C, R=0.1					
ΔK	380.	7.4	27.	0.2	1.2×10^5
ΔK	290.	7.9	27.	0.38	1.4×10^5
ΔK_{eff}	380.	7.4	27.	0.2	5.5×10^4
ΔK_{eff}	290.	7.9	27.	0.38	5.8×10^4
260°C, R=0.1					
ΔK	462.	5.0	27.	0.2	1.9×10^5
ΔK	331.	5.1	27.	0.38	3.0×10^5
ΔK_{eff}	462.	5.0	27.	0.2	1.4×10^4
ΔK_{eff}	331.	5.1	27.	0.38	2.1×10^4

R20431/1

The second set of calculations forced the life to 10^7 cycles, and produced estimates of a_i and ΔK_{th} . For this case the estimates of a_i were fairly close to the expected value in most instances, and the estimates of ΔK_{th} were uniformly lower than the experimentally determined values.

A comparison was made between the lives obtained using ΔK_{th} from the bend specimen vs the CT specimen. Although the ΔK_{th} values were fairly close, 2.1 vs 2.9 MPa \sqrt{m} , they resulted in life estimates almost three orders of magnitude apart. This is almost certainly a result of the nearly vertical crack growth rate curve in the near threshold region and the deterministic nature of the calculation. It follows that small errors in ΔK_{th} can cause huge life variations.

Finally, cyclic life estimates were made for the notched geometries. Again, fatigue limit stresses were used, but in this case, the ΔK_i was calculated assuming that the notch was acting as a crack. Calculations were made using both ΔK and ΔK_{eff} as integration parameters. In both instances, the life estimates were shorter than the 10^7 fatigue limit life demonstrated by the HCF specimens.

A few tentative conclusions can be made from these calculations. The life estimates were generally very low, pointing to an incubation or initiation time prior to the existence of an active crack. This is in agreement with the fractographic evidence presented earlier. The life estimates were extremely sensitive to ΔK_{th} , with very large life differences resulting from changes in ΔK_{th} .

that were within the experimental scatter. Thus, deterministic calculations of this type can be subject to large errors in cyclic life. It can also be observed that both these problems could be exacerbated by small crack behavior, which is certainly a possibility considering the crack sizes in question. Finally, it should be noted that these conclusions do not address another underlying problem in producing fracture based Goodman diagrams — the lack of stress ratio effect on ΔK_{th} .

SECTION VI

TASK V — VALIDATION TESTING

This task was originally intended to perform a series of HCF tests at varying conditions to verify the capabilities of the model generated in Task IV. It is readily apparent from the results discussed in Task IV that modeling of Ti 8-1-1 HCF behavior based strictly on threshold stress intensities and fracture mechanics tenets is not feasible. It was further concluded that performing a series of validation tests would not be productive if simple cyclic behavior could not be modeled. Therefore, the validation test program was modified to produce information which would be more useful to the objectives of the program. The first two sections of the modified program have already been discussed. Smooth bar HCF tests were conducted at 500°F, R=0.7 for comparison to cyclic/dwell results. Those tests were reported in Section IV. The additional analyses required in the analytical modeling section were also part of the change. The life assessments made through integrating crack growth rate curves were not originally scheduled, but were useful in evaluating the role of initiation in HCF lives.

Finally, a series of tests was conducted which was aimed at substantiating the incubation times required to generate a crack-like defect in a smooth HCF specimen. The tests were conducted in the same manner as the testing in Task III, but were inspected at regular intervals for crack initiations.

The majority of these tests were conducted at 27°C, R=0.1, and 621 MPa, a condition which consistently produced surface connected initiations. The surface of the specimens was examined at regular cyclic intervals using both fluorescent penetrant inspection and acetate replicas. Prior experience with these techniques showed them capable of resolving flaws in the range of 0.025 – 0.050 mm surface length. However, considerable difficulty was encountered in locating flaws prior to failure of the specimens. This is probably related to a relatively short fatigue crack propagation life as compared to the total fatigue life. An estimate of the crack propagation life from 0.025 mm to failure yields about 5×10^4 cycles. This is a relatively short interval if one considers that the scatter in fatigue life at this condition is in excess of 2.5×10^6 cycles. Cyclic intervals between inspections were reduced over the course of the testing to 2.5×10^4 . The number of inspections required by these conditions severely limited the number of tests conducted.

Although not entirely successful, these tests gave further credence to the supposition of a relatively long initiation life. Five tests were conducted at 27°C. The number of cycles between the final inspection, and specimen failure are listed in Table 9. These intervals vary between 1.82×10^5 cycles and 7.5×10^3 cycles. All of these are much shorter than the fatigue lives which vary from 5×10^6 to 2.55×10^6 cycles. A crack was located on only one specimen prior to failure. A crack of 0.86 mm surface length was located on specimen B52 on the final inspection prior to failure. As indicated by Table 9, the specimen survived only 7500 cycles after that inspection. A single test was conducted at 260°C with similar results. All the failures displayed surface connected origins. This is strong evidence that the fatigue crack propagation life is a minor fraction of the total fatigue life for Ti 8-1-1.

TABLE 9. HCF Tests with Inspections

<i>Specimen S/N</i>	<i>Cycles to Failure</i>	<i>Cycles Between Final Inspection and Failure</i>
B41	2.55×10^6	5.4×10^4
B42	4.09×10^6	1.82×10^5
B44	2.67×10^6	6.9×10^4
B48	3.17×10^6	2.1×10^4
B52	5.25×10^6	7.5×10^3
B53 (260°C)	4.58×10^6	1.0×10^5

R20431/1

SECTION VII

DISCUSSION

1. MEASUREMENT OF ΔK_{th}

It is apparent from the results of this contract that ΔK_{th} is dependent on test method. Varying the test specimen geometry and test technique can result in different values for ΔK_{th} . This finding is in accordance with other studies (Ref. 9-12). Other investigators have also found that loading history can affect ΔK_{th} (Ref. 9,11,13). This investigation did not specifically identify loading history as the cause of changes in ΔK_{th} , but there were several indications that this was the case. Retesting an unfailed bend specimen at a higher ΔK level generally resulted in inconsistent values of ΔK_{th} . This procedure was not used in any of the reported results. FAU also experience some difficulties in obtaining repeatable results after a specimen had been inadvertently overloaded. Both of these occurrences support the premise that ΔK_{th} is sensitive to loading history.

It is obvious that the ΔK_{th} results obtained from the two test techniques employed by this program cannot be reconciled without some type of correction. Using either closure correction to produce a $\Delta K_{th,eff}$ or a test technique which avoids closure, constant- K_{max} increasing- R , with the CT specimen, brings the data into reasonable concurrence. These procedures also eliminate the effect of stress ratio on threshold stress intensity. Again, these results are consistent with the findings of other investigators (Ref. 5,13-15,30). It has also been suggested that closure can be used to account for the effect of temperature on ΔK_{th} (Ref. 16,17). This was not found to be the case for Ti 8-1-1, perhaps due to a differing closure mechanism.

It appears that closure correction, or avoidance, is a necessary technique for generating consistent ΔK_{th} data. The problem with this is the closure measurements themselves. To date, no generally accepted method has been established for the measurement of closure levels. As indicated by the two closure measuring procedures evaluated, $\Delta K_{th,eff}$ can vary considerably depending on the analysis method used. In this investigation, the ability to collapse R -data was used as a criterion for selecting a closure measuring technique. Unfortunately, this amount of data is seldom available. Further, not all specimen geometries lend themselves readily to obtaining closure measurements: witness the bend specimen used in this program. If closure is to become a requirement for threshold stress intensity testing, a standardized measurement technique must be established.

Application of this information can also raise difficulties. For example, how well can closure levels be predicted in a component geometry, particularly if faced with alternate or mixed closure mechanisms? In this investigation it can be reasonably assumed that the overriding closure mechanism was plastic wake closure, after Elber (Ref. 18). Ti 8-1-1 has a fine microstructure, flat fracture surfaces, and relatively large cracks were employed. Thus, asperity-induced closure should have been minimized. It is also unlikely that the minimal oxidation observed at 260°C was sufficient to cause oxide related closure. This straightforward situation does not always exist in components, which employ notches, are fabricated from damage tolerant microstructures, and often operate in hostile environments. Problems such as these are beginning to be addressed, notably by Newman (Ref. 19,31,32).

Arguments related to threshold crack growth behavior inevitably include discussions of small flaws. Small flaws cannot be avoided in this connotation since by their very nature, growth rates associated with them usually occur in the threshold regime. It is generally accepted that crack growth rates for small and large cracks are not always equal, especially near threshold. It has also been observed that the difficulties discussed above are exaggerated when dealing with

small flaws. That problem has been examined in exhaustive detail in the literature, a good review of which is given by Miller (Ref. 20-21).

Some investigators have been successful in obtaining repeatable ΔK_{th} information with large and small cracks by employing closure corrections (Ref. 5). However, this has not always proved to be the case (Ref. 22). In fact, it is questionable whether a unique value of ΔK_{th} can even be defined for small cracks. This is particularly true in relation to microstructurally small flaws, where features such as grain boundaries and crystallographic orientations can impact crack growth rates.

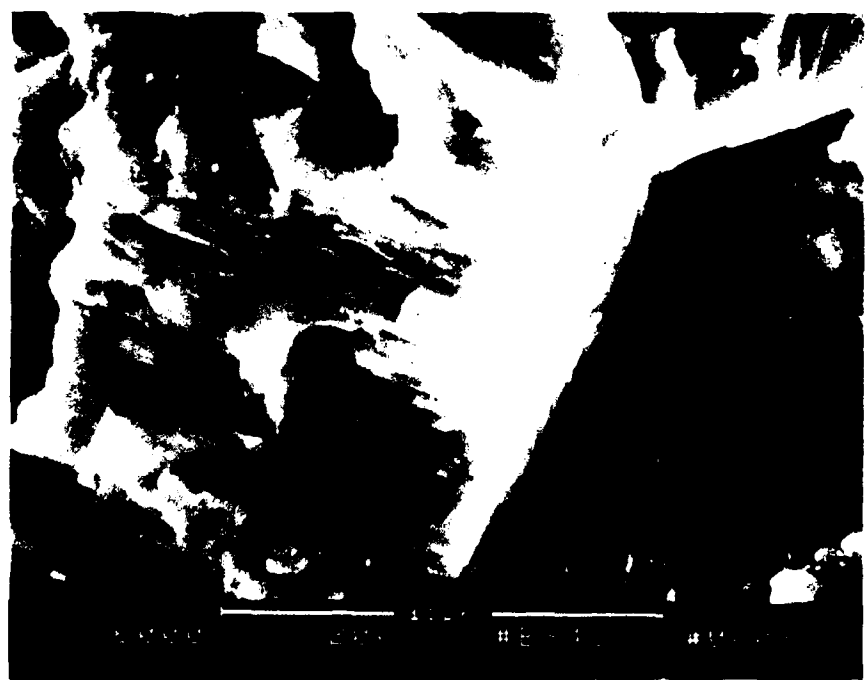
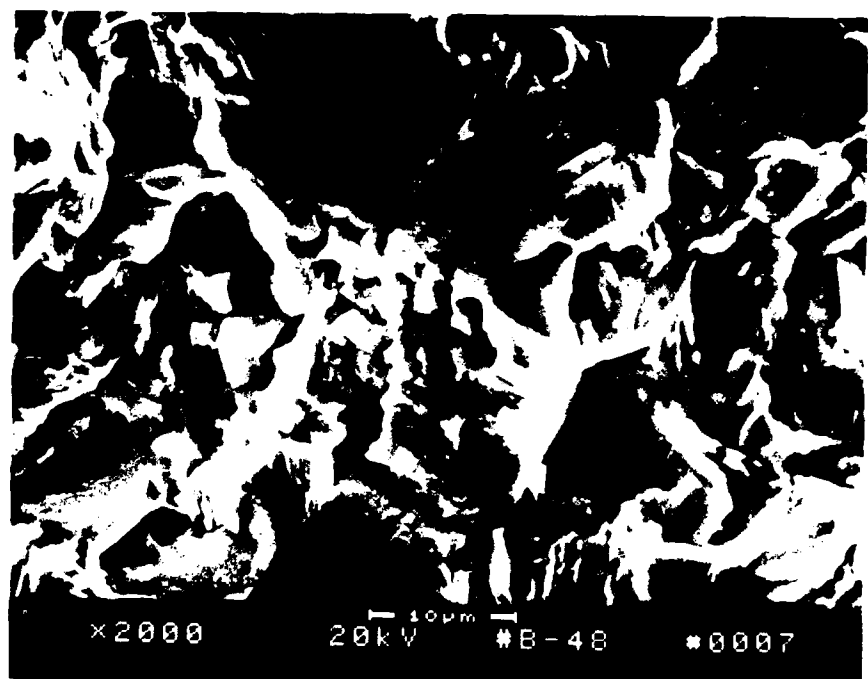
In applying ΔK_{th} to small flaws, the question of when a flaw can be treated as a crack must be addressed. Numerous definitions of this condition have been recommended, in most instances relating crack size to a physical feature such as grain size, typical asperity size, or plastic zone size. Obviously, most of these definitions are highly material dependent. Since small flaw investigations on a fine grained titanium alloy (Ref. 23) imply that the variation in growth rates due to crack size for Ti 8-1-1 would be minimal, a useful definition might be the point at which the flaw is demonstrably propagating as a fatigue crack. An earlier investigation on titanium indicated that the transition point between crystallographic slip and ductile, i.e., striated, fatigue crack advance occurs when the cyclic plastic zone size is approximately equal to the alpha grain size (Ref. 24). Performing that calculation at a stress level equal to the fatigue limit yields a crack size of about 0.5 mm. This is rather larger than most small flaw definitions would suggest and is vastly larger than the crack sizes used for the calculations in this program. Detail SEM fractography was capable of resolving striations on HCF fracture surfaces at crack depths of 0.2-0.4 mm, see Figure 77. This is in rough agreement with the calculated transition point of 0.5 mm and would probably provide a conservative starting point for crack propagation calculations.

Clearly, by any of the definitions discussed above, small crack behavior would be expected to impact the HCF modeling calculations performed herein. This too would have to be considered as a potential source of the inaccuracies in those calculations.

2. ANALYTICAL MODELING CONSIDERATIONS

The analytical modeling efforts point to the conclusion that the HCF behavior of Ti 8-1-1 cannot be simply modeled using ΔK_{th} data and fracture mechanics principles. There appear to be two main obstacles to the success of that procedure: (1) obtaining a consistent measurement of ΔK_{th} requires the use of closure corrections, or a test technique which minimizes the effect of closure. However, the threshold stress intensities measured in this fashion display little or no stress ratio effect, such as that observed in HCF data; and (2) Ti 8-1-1 does not appear to contain intrinsic defects of any significant size, as do many engineering materials. Without the presence of such defects, a considerable number of cycles is required to generate a defect which will propagate as a fatigue crack. Being essentially a stochastic process, this initiation life is difficult, if not impossible, to predict using simple, largely deterministic, fracture mechanics models.

It can be speculated that these two phenomena are related. The cyclic fatigue crack growth calculations discussed earlier and the inspection tests on HCF specimens indicate that the propagation life can be a small fraction of the total HCF life in a smooth section. Since mean stress demonstrates a strong effect on initiation life and mechanisms (for example, note the subsurface initiations for the R=0.7 HCF tests), it is conceivable, perhaps even likely, that the stress ratio effect on HCF life is largely tied up in the cycles required for crack initiation.



FD 357483

Figure 77. HCF Fracture Surface Showing Fine Striations Approximately 0.4 mm from Origin; Tested at 27°C, R=0.1, T_{max} σ = 620 MPa

Additionally, the impact of small flaw behavior must be considered. Although not specifically demonstrated by the results of this program, small crack behavior would almost certainly affect modeling of the type being attempted for Ti 8-1-1, as discussed above.

The obvious question arising from these discussions is, "What can be done to make the models work?". The simple answer is to model both the initiation and propagation portions of the lives. Solutions, unfortunately, are not so straightforward. The problem can be approached in several ways. For example, approaches based on damage accumulation at the initiation site and extrapolation of an effective $\Delta K = \Delta K - K_{th}$ have been suggested (Ref. 25-27). The applicability of these models remains to be proven. Pratt and Whitney has used a probabilistic approach to the initiation and transition regions of crack development (Ref. 28). This technique has proven successful for low cycle fatigue, and there are no immediately obvious reasons why a similar approach could not be applied to HCF behavior. However, these techniques require more information than is necessary for the simple models explored in this program. It might also be possible to obtain a more complete characterization of small flaws in the near threshold region, thus allowing for accurate life assessments using traditional fracture mechanics approaches. What would constitute a complete characterization of small crack behavior or even how to define ΔK_{th} for small flaws remains an open question. From this admittedly biased viewpoint, the probabilistic approach appears to hold the most short-term promise.

The ΔK_{th} modeling in this contract did present some promise for situations in which an initial flaw is more readily defined. The models were able to assess to some degree the behavior of Ti 8-1-1 containing relatively large extrinsic damage. This suggests that a similar model could predict HCF behavior in a material which contains either crack-like initial material defects, or which is subject to the rapid formation of fatigue cracks. A study by Majumdar and Kwasny (Ref. 29), on PWA 1480, a single crystal nickel alloy, demonstrated that in the presence of large inclusions (100-200 microns) conventional fracture mechanics and ΔK_{th} data can provide reasonable estimates of HCF behavior. Also, some advanced materials, such as titanium-aluminides, have relatively low ductilities, correspondingly low tolerance of initial defects, and may therefore lend themselves to HCF life predictions based on ΔK_{th} , even in the absence of large defects.

Some overall conclusions may be drawn from these discussions. First, the ΔK_{th} modeling of HCF behavior, as presented here, is not appropriate for ductile materials such as Ti 8-1-1. Second, the application of a damage-based HCF life prediction system for that class of materials would require assessment of the initiation life as well as crack propagation life. That assessment would require the consideration of small flaw effects, particularly in component applications. Third, and last, HCF modeling based on ΔK_{th} behavior may be applicable to materials with low defect tolerance, or materials which contain large initial defects.

SECTION VIII

CONCLUSIONS

1. The following conclusions are based on threshold test results for Ti 8-1-1:
 - ΔK_{th} is slightly decreased at elevated temperature.
 - ΔK_{th} is insensitive to frequency above 30 Hz.
 - The addition of an intermittent dwell to high frequency cycling causes a small increase in ΔK_{th} at high mean stresses, R=0.7.
 - Threshold stress intensity remains approximately constant as a function of stress ratio after correction for closure, or when the test technique minimizes closure. In the absence of these conditions, ΔK_{th} decreases with increasing stress ratio.
2. ΔK_{th} measurements vary with test specimen and procedure.
3. Obtaining reproducible values for threshold stress intensity requires closure correction, or a test technique which minimizes closure.
4. HCF behavior of Ti 8-1-1 is degraded by the presence of FOD in those size ranges observed in fan and compressor blades. The degradation is not as severe as would be expected based strictly on crack growth behavior. (In actual practice, such FOD is removed by blending and polishing during engine overhauls.)
5. HCF behavior in Ti 8-1-1 cannot be accurately predicted using simple fracture mechanics models and ΔK_{th} data. These models can predict rough trends for HCF behavior of material containing relatively large damage.
6. A successful damage based HCF life prediction system for the class of materials similar to Ti 8-1-1 would require the assessment of both crack initiation and propagation lives and would likely require consideration of small flaw behavior.
7. HCF modeling based on ΔK_{th} behavior may be applicable to materials containing large initial defects or materials with low defect tolerance.

REFERENCES

1. Harris, J.A. and R. White, "Engine Component Retirement for Cause," Pratt & Whitney Interim Technical Report FR-17519, August 1983, AFWAL Contract No. F33615-80-C-5160.
2. Engsberg N., C.G. Annis, Jr., and B.A. Cowles, "Effects of Defects in P/M Superalloys," Report No. AFWAL-TR-81-4191, Final Report for Contract F33615-79-C-5074, February 1982.
3. Standard Test Method for Measurement of Fatigue Crack Growth Rates, E647-88, *Annual Book of ASTM Standards*, Vol. 03.01, Metals-Mechanical Testing; Elevated and Low Temperature Tests; Metallography; American Society for Testing and Materials, pp. 636-654, 1988.
4. Saxena, A., S.J. Hudak, Jr., J.K. Donald, and D.W. Schmidt, "Computer Controlled Decreasing Stress Intensity Technique for Low Rate Fatigue Crack Growth Testing," *Journal of Testing and Evaluation*, JTEVA, Vol. 6, No. 3, pp. 167-174, 1978.
5. Jira, J.R., T. Nicholas, and J.M. Larsen, "Fatigue Thresholds in Surface Flaws in Ti 6Al-2Sn-4Zr-6Mo" *Fatigue*, 1987.
6. Ostergren, W.J. "A Damage Function and Associated Failure Equations for Predicting Hold Time and Frequency Effects in Elevated Temperature, Low Cycle Fatigue," *Journal of Testing and Evaluation*, No. 5, Sept. 1976.
7. Pejsa, P.N. and B.A. Cowles, "Thermal Mechanical Fatigue Life Prediction for Advanced Anisotropic Turbine Alloys," *Transactions of the ASME, Journal of Engineering for Gas Turbine and Power*, Vol. 108, July 1986, pp. 504-506.
8. Raju, I.A. and J.C. Newman, "Stress-Intensity Factors for Circumferential Surface Cracks in Pipes and Rods Under Tension and Bending Loads," *Fracture Mechanics: Seventeenth Volume, ASTM STP 905*, J.H. Underwood, R. Chait, C.W. Smith, D.P. Wilhelm, W.A. Andrews, and J.C. Newman, eds., American Society for Testing and Materials, Philadelphia, pp. 789-805, 1986.
9. Vaidya, W.V., "Near Threshold Fatigue Crack Propagation Behaviour of a Heterogeneous Microstructure," *Fatigue Fracture Engineering Materials & Structures*, Vol. 9, No. 4, pp. 305-317, 1986.
10. Taylor, D., "A Compendium of Fatigue Thresholds and Growth Rates," *Engineering Materials Advisory Services Ltd.*, London, U.K., 1985.
11. Backlund, J., A.F. Blom, and C.J. Beevers, eds., *Fatigue Thresholds*, Volume I, *Engineering Materials Advisory Services Ltd.*, London, U.K., 1982.
12. Tokaji, K., Z. Ando, and K. Nagae, "The Effect of Sheet Thickness on Near-Threshold Fatigue Crack Propagation and Oxide and Roughness Induced Crack Closure," *Transactions of the ASME*, Vol. 109, January 1987, pp. 86-91.
13. Taylor, D., "Fatigue thresholds: their applicability to engineering situations," *Fatigue Review*, No. 2 (1988), pp. 67-79.

14. Liaw, P.K., W.A. Logsdon, "Crack Closure: An Explanation for Small Fatigue Crack Growth Behavior," *Engineering Fracture Mechanics*, Vol. 22, No. 1, pp. 115-121, 1985.
15. Liaw, P.K., "Overview of Crack Closure at Near-Threshold Fatigue Crack Growth Levels," presented at International Symposium on Fatigued Crack Closure, 1986.
16. Liaw, P.K., "Mechanism of Near-Threshold Fatigue Crack Growth in a Low Alloy Steel" *Acta Metall.* (August 1985): 1489-1502.
17. Liaw, P.K. and Logsdon, W.A., "The Influence of Load Ratio and Temperature on the Near-Threshold Fatigue Crack Growth Rate Properties of Pressure Vessel Steels," *Trans. of ASME*, 107 (January 1985): 26-33.
18. Elber, W., "Fatigue Crack Closure Under Cyclic Tension," *Engineering Fracture Mechanics*, 1970, Vol. 2, pp. 37-45.
19. Newman, J.C., "A Crack Closure Model for Predicting Fatigue Crack Growth under Aircraft Spectrum Loading," *ASTM STP 748*, 1981, pp. 53-84.
20. Miller, K.J., "The Behaviour of Short Fatigue Cracks and Their Initiation," Part I — A Review of Two Recent Books, *Fatigue Fracture Engineering Materials & Structures*, Vol. 10, No. 1, pp. 75-91, 1987.
21. Miller, K.J., L.H. Larsson, "The Behaviour of Short Fatigue Cracks and Their Initiation," Part II — A General Summary, *Fatigue Fracture Engineering Materials & Structures*, Vol. 10, No. 2, pp. 93-113, 1987.
22. Larsen, J.M., T. Nicholas, A.W. Thompson, and J.C. Williams, "Small Crack Growth in Titanium-Aluminum Alloys," presented at the Second International (Engineering Foundation) Conference on Small Fatigue Cracks, Santa Barbara, CA, Jan 5-10, 1986.
23. Larsen, J.M., J.R. Jira, and T. Weerasooriya, "Crack Opening Displacement Measurements on Small Cracks in Fatigue," presented at the ASTM 18th National Symposium on Fracture Mechanics, Boulder, CO, June 1985.
24. H. Yuen, S.W. Hopkins, G.R. Leverant, and C.A. Rau, "Correlations Between Fracture Surface Appearance and Fracture Mechanics Parameters for Stage II Fatigue Crack Propagation in Ti-6Al-4V," *Metallurgical Transaction*, Vol. 5, August 1974, pp. 1833-1842.
25. Chalant, G. and L. Remy, "Model of Fatigue Crack Propagation by Damage Accumulation at the Crack Tip," *Engineering Fracture Mechanics*, Vol. 18, No. 5, pp. 939-952, 1983.
26. Tokarsky, B., "Fatigue Failure Model Including Both Initiation and Propagation of the Crack," *Engineering Fracture Mechanics*, Vol. 25, No. 1, pp. 103-109, 1986.
27. Xiulin, Zheng, "A Simple Formula for Fatigue Crack Propagation and a New Method for The Determination of ΔK_{th} ," *Engineering Fracture Mechanics*, Vol. 27, No. 4, pp. 465-475, 1987.
28. Watkins Jr., T. and C.G. Annis, Jr., "Engine Component Retirement for Cause: Probabilistic Life Analysis Technique," Pratt & Whitney Interim Technical Report FR-18618, June 1985, AFWAL Contract No. F33615-80-C-5160.
29. Majumdar, S. and R. Kwasny, "Effects of a High Mean Stress on the High Cycle Fatigue Life of PWA 1480 and Correlation of Data by Linear Elastic Fracture Mechanics," Argonne National Laboratory Report, ANL-85-74, November 1985, NASA/CR-175057.

30. Matsuoka, S., Takeuchi, E., Kosuge, M., Shimodaira, M., Ohta, A., and Nishijima, S., "A Method for Determining Conservative Fatigue Threshold While Avoiding Crack Closure," *Journal of Testing and Evaluation*, JTEVA, Vol. 14, No. 6, Nov. 1986, pp. 312-317.
31. Newman, J.C., "Prediction of Fatigue Crack Growth under Variable Amplitude and Spectrum Loading Using a Closure Model," ASTM STP 761, 1982, pp. 255-277.
32. Newman, J.C., "A Crack Opening Stress Equation for Fatigue Crack Growth," *Journal of Fracture* 24, 1984, R131-R135
33. Foster, R.L., S. P. Wnuk, Jr., "High Temperature Capacitive Displacement Sensors," Proceedings of The 31st International Symposium, Instrumentation in The Aerospace Industry, Vol. 31, Instrument Society of America, Paper No. 85-0123, 1985.

APPENDIX A

FLORIDA ATLANTIC UNIVERSITY AUTOMATED FATIGUE-CRACK GROWTH TEST SYSTEM

Near-threshold fatigue-crack growth tests were conducted by the Materials Laboratory in the Department of Mechanical Engineering at Florida Atlantic University. These tests were performed with compact tension specimens of Ti-8Al-1Mo-IV material according to ASTM standard E647 (Reference 3).

The Materials Laboratory is equipped with an MTS Model 810 closed-loop servo-hydraulic test machine with a 89KN capacity. Computer control is provided by a Fracture Technology Associates Automated Fatigue-Crack Growth System monitoring compliance for crack length determination. A standard MTS clip gage is used for displacement measurements at room temperature, while a HITEC Products, Inc. capacitive displacement gage is used for the elevated temperature test measurements. Crack length is also monitored visually with a Gaertner traveling microscope. A clamshell type resistance furnace is used for the elevated temperature tests with a capability of 1100°C.

COMPUTER CONTROLLED FATIGUE-CRACK GROWTH TESTING

The Automated Fatigue-Crack Growth System consists of an IBM PC-XT computer with 256K memory and two double-density, double-sided disk drives. An Amdek 300 monochrome monitor and a Texas Instruments 855 printer are included. Fracture Technology Associates builds the interface between the IBM PC and the MTS test machine. This console-mounted unit provides all of the input/output connections necessary for operation. The IBM PC is modified to include the waveform generator circuit board, the analog/digital interface board, and the graphics display board. The waveform generator currently provides a sinusoidal or triangular signal.

The software for the system is also provided by Fracture Technology Associates. It allows the operator to control the test in either a constant load, a constant stress intensity (K), or a K -gradient condition. The software is interactive and requires input of the specimen dimensions and material properties, along with the coefficients for the compliance calibration for the particular location of the crack mouth opening displacement (COD) gage. The constant load (or the initial load in the case of the K control tests) and the frequency of loading are selected by the operator. The range of crack length to specimen width ratio (a/W) over which the crack will be allowed to propagate is also specified along with the desired data acquisition parameters that control data storage rate. The software allows the operator to monitor or update any of the test parameters, vary test frequency, monitor test system status, and control start-up and shut-down of the test machine. It also provides a graphic display of the load/displacement trace used to determine compliance, and a display of the stored fatigue-crack growth rate (da/dN) versus stress intensity range (ΔK) data.

The computer monitors load and COD to calculate the compliance and determine crack length. Specimen compliance is calculated by taking a specified number of data points at the upper end of the load/displacement curve for each cycle of loading. Linear regression is then performed on these data to determine the slope. The slopes from successive loading cycles are averaged to reduce the variability associated with determining the crack length based on just one cycle of the load/displacement record. The software allows a choice in the linear regression analysis of using data from the loading portion, unloading portion, or both, of the load/displacement cycle. Once the slope is determined, the specimen compliance (inverse slope) is used to calculate the crack length based on the expressions published by Saxena, et al

(Reference 4). This crack length along with the compliance value are printed by the plotter. Fatigue-crack growth rate and stress intensity range are calculated and stored only at operator specified intervals. Fatigue-crack growth rate is based on the secant method of analysis. Stress intensity range is calculated in accord with ASTM E647.

Crack closure is an important aspect of near-threshold fatigue crack growth. The crack closure load, which corresponds to the point in the load/displacement curve where there is a change in slope and the crack is actually closed, is used to determine an effective stress intensity range (ΔK_{eff}) at the crack tip. ΔK_{eff} is the true stress intensity range seen by the crack tip based on the portion of the load cycle in which it is open, and may be significantly less than ΔK calculated from the applied loads. Often, measurement of the crack closure load is essential to accurately determine the behavior of cracks in the near-threshold region. An option in the software permits measurement of the crack closure load. When this option is selected, the computer calculates the 1, 2, 4, 8, and 16 percent deviations in load/displacement slope from the slope used for the compliance calculation during a particular load cycle. These deviations are displayed on the graphics screen that presents the load/displacement curve used to determine compliance. The operator must select the appropriate load level to use as the crack closure load. The stored values of ΔK can then be adjusted based on the crack closure load to give ΔK_{eff} .

CRACK MOUTH OPENING DISPLACEMENT (COD) MEASUREMENT AT HIGH TEMPERATURE

A HITEC Products, Inc. capacitive displacement gage is used to measure COD at elevated temperatures. This gage is a cylindrical sensor approximately one inch long and 0.375 inch in diameter that acts as one plate of a capacitor with a ground target as the other plate. The sensor and target fit completely inside the furnace and are mounted across the notch of the compact tension specimen using the same machined screw holes required for mounting of knife edges for the MTS clip gage. A small gap is left between the sensor and the target, the size of which is adjusted to be in the middle of the particular gage sensitivity range selected. A separate amplifier supplied for the gage has a digital readout of displacement on the front face, along with an output jack on the rear that provides the displacement signal to the computer. The gage has two sensitivity ranges (0 to 2.54 mm and 0 to 0.254 mm) and is capable of being used to 650°C. It is not frequency limited and therefore near-threshold fatigue-crack growth tests can be conducted up to the capability of the frequency response of the MTS machine. Reference (33) provides a complete description of the theory of operation of the gage.

RESISTIVE FURNACE SYSTEM

A clamshell type resistive furnace wraps completely around the compact tension specimen to provide a constant elevated temperature environment. Test temperature is controlled by a Barber Coleman Company 560 Series Digital Controller with a Model CB41 Single Phase Power Controller. The system operates on 120 vac and uses a Type K (Chromel-Alumel) thermocouple for feedback from the furnace. The digital controller has adjustable upper and lower interlocking alarms to control overshoot and undershoot of the set point temperature. The furnace has a maximum capability of 1100°C. Openings have been built into the front and back of the furnace to allow visual readings of crack length using a traveling microscope.

APPENDIX B**THRESHOLD TESTING****TABLE B-1. LOW FREQUENCY THRESHOLD TESTING**

<i>Specimen I.D.</i>	<i>Temperature °C</i>	<i>Stress Ratio</i>	<i>Frequency Hz</i>	<i>Delta K (MPa √m)</i>	<i>Fail Yes or No</i>
3679	27	0.1	30	2.51	No
3680	27	0.1	30	2.80	Yes
3676	27	0.1	30	4.29	Yes
3675	27	0.1	30	6.89	Yes
3705	27	0.5	30	1.36	No
3707	27	0.5	30	1.74	No
3711	27	0.5	30	1.75	No
3712	27	0.5	30	1.99	No
3706	27	0.5	30	2.48	Yes
3702	27	0.5	30	3.11	Yes
3677	27	0.7	30	2.03	No
3684	27	0.7	30	2.22	No
3683	27	0.7	30	2.68	Yes
3681	27	0.7	30	3.41	Yes
3701	27	-1.0	30	2.13	No
3698	27	-1.0	30	3.07	Yes
3699	27	-1.0	30	3.70	No
3700	27	-1.0	30	5.03	Yes
3714	260	0.1	30	1.20	No
3685	260	0.1	30	2.17	Yes
3718	260	0.1	30	2.25	No
3686	260	0.1	30	2.37	Yes
3694	260	0.5	30	1.43	No
3695	260	0.5	30	1.49	No
3696	260	0.5	30	1.83	No
3697	260	0.5	30	2.20	Yes
3689	260	0.7	30	1.34	No
3688	260	0.7	30	1.67	Yes
3687	260	0.7	30	2.27	Yes
3692	260	-1.0	30	2.70	No
3690	260	-1.0	30	4.11	No
3693	260	-1.0	30	4.14	Yes
3691	260	-1.0	30	4.75	Yes

R20431/21

TABLE B-2. HIGH FREQUENCY THRESHOLD TESTING

<i>Specimen I.D.</i>	<i>Temperature °C</i>	<i>Stress Ratio</i>	<i>Frequency Hz</i>	<i>Delta K (MPa √m)</i>	<i>Fail Yes or No</i>
3719	27	0.5	200	1.75	No
3722	27	0.5	200	1.80	No
3721	27	0.5	200	2.30	No
3724	27	0.5	200	2.88	Yes
3720	27	0.5	200	2.98	Yes
3725	27	0.5	200	3.31	Yes
3768	260	-1.0	200	1.47	No
3770	260	-1.0	200	1.74	Yes
3769	260	-1.0	200	2.04	Yes
3728	260	0.1	200	1.21	No
3768	260	0.1	200	1.47	No
3726	260	0.1	200	1.88	No
3767	260	0.1	200	1.96	Yes
3727	260	0.1	200	2.96	Yes
3771	260	0.5	200	1.88	No
3772	260	0.5	200	1.97	No
3773	260	0.5	200	2.27	No
3775	260	0.5	200	2.51	Yes
3778	260	0.7	200	1.19	No
3776	260	0.7	200	1.54	No
3777	260	0.7	200	1.64	Yes
3780	260	0.5	200/2MD	2.02	No
3783	260	0.5	200/2MD	2.09	Yes
3779	260	0.5	200/2MD	2.37	Yes
3784	260	0.5	200/2MD	1.45	No
3785	260	0.5	200/2MD	1.63	No
3786	260	0.5	200/2MD	1.97	No
3787	260	0.5	200/2MD	2.11	No
3789	260	0.5	200/2MD	2.52	No
3791	260	0.5	200/2MD	2.66	Yes

R20431/21

TABLE B-3. TESTS CONDUCTED AT FAU-CT GEOMETRY

Specimen	<i>Near Threshold Tests</i>				
	K-Grad (mm ⁻¹)	R	Temp (°C)	ΔK _{th} (MPa √in)	ΔK _{th,eff} (MPa √m)
SPT2D1	-0.08	0.1	27	5.77	2.49
SPT2D2	-0.08	0.1	27	5.60	2.53
SPT8A	-0.06	0.1	27	5.23	2.60
SPT7	-0.06	0.1	260	5.26	2.93
SPT8B	-0.06	0.1	260	5.11	2.78
SPT9	-0.06	0.5	260	3.58	3.30
SPT10	-0.06	0.5	260	3.25	2.91
SPT5E	-0.06	0.7	260	2.51	2.51
SPT12	-0.06	0.7	260	2.64	2.64
PWA1	-0.08	VAR	260	2.15	N/A
PWA2	-0.08	VAR	260	2.28	N/A

<i>Constant Amplitude Tests</i>			
Specimen	R	Temp (°C)	Max Load (N)
SPT4CL	0.1	27	5782
SPT7CL	0.1	260	3336
SPT9CL	0.5	260	3380
SPT12CL	0.7	260	5338

R20431/21

APPENDIX C
AXIAL FATIGUE RESULTS OF PWA 1202

TABLE C-1. TEMP = 27°C K_t = 1.0

Figure	S/N	Stress Ratio	Maximum Stress (MPa)	Cycles to Failure	Remarks
1	1	-1.0	563	1.55E5	
1	18	-1.0	517	2.19E5	
1	14	-1.0	517	3.97E5	
1	15	-1.0	517	3.49E6	
1	48	-1.0	483	2.82E6	
1	5	-1.0	483	7.60E6	
1	11	-1.0	448	4.07E6	
1	46	-1.0	448	1.00E7	Did not fail
1	12	-1.0	448	1.00E7	Did not fail
1	20	-1.0	414	1.00E7	Did not fail
2	41	0.1	758	2.62E5	
2	49	0.1	690	4.29E5	
2	32	0.1	690	1.24E6	
2	6	0.1	621	1.22E6	
2	24	0.1	621	3.68E6	
2	45	0.1	587	7.69E6	
2	76	0.1	552	2.00E6	
2	79	0.1	552	2.66E6	
2	53	0.1	552	4.27E6	
2	75	0.1	517	1.00E7	Did not fail
2	78	0.1	517	1.00E7	Did not fail
2	7	0.1	517	1.00E7	Did not fail
3	73	0.5	862	4.18E5	
3	57	0.5	827	5.96E5	
3	61	0.5	758	5.91E5	
3	9	0.5	758	1.09E6	
3	64	0.5	690	1.08E6	
3	65	0.5	690	2.41E6	
3	77	0.5	655	2.58E6	
3	51	0.5	621	1.00E7	Did not fail
3	69	0.5	621	1.00E7	Did not fail

R20431/35

TABLE C-2. TEMP = 260°C K_t = 1.0

Figure	S/N	Stress Ratio	Maximum Stress (MPa)	Cycles to Failure	Remarks
4	10	-1.0	552	7.44E4	
4	4	-1.0	517	5.35E5	
4	3	-1.0	483	7.71E5	
4	2	-1.0	483	2.24E6	
4	67	-1.0	448	7.40E6	
4	13	-1.0	448	1.00E7	Did not fail
4	43	-1.0	414	1.00E7	Did not fail
4	62	-1.0	414	1.00E7	Did not fail
5	16	0.1	690	3.12E5	
5	47	0.1	621	1.04E6	
5	76	0.1	621	1.40E6	
5	22	0.1	552	7.82E5	
5	30	0.1	552	1.05E6	
5	19	0.1	552	6.37E6	
5	52	0.1	517	3.36E6	
5	44	0.1	517	7.39E6	
5	58	0.1	517	1.00E7	Did not fail
5	38	0.1	483	1.00E7	Did not fail
5	75	0.1	483	1.00E7	Did not fail
6	80	0.5	896	9.59E4	
6	72	0.5	827	7.56E5	
6	77	0.5	758	1.30E6	
6	33	0.5	758	1.34E6	
6	63	0.5	690	3.79E6	
6	26	0.5	655	3.49E6	
6	55	0.5	621	2.33E6	
6	40	0.5	621	1.00E7	Did not fail
6	74	0.5	587	1.00E7	Did not fail
16	23	0.7	772	1.00E7	
16	27	0.7	758	1.00E7	
16	25	0.7	827	5.08E6	
16	30	0.7	827	4.06E6	
16	26	0.7	862	1.57E6	
16	24	0.7	896	5.38E6	

R20431/35

TABLE C-3. TEMP = 260°C 0.20mm DEFECT

Figure	S/N	Stress Ratio	Maximum Stress (MPa)	Cycles to Failure	Remarks	Defect Size
9	B21	-1.0	483	3.00E4		0.15mm
9	B31	-1.0	414	6.40E4		0.18mm
9	B45	-1.0	379	3.58E5		0.18mm
9	B39	-1.0	345	1.52E6		0.15mm
9	B67	-1.0	310	6.27E6	Surface damage	
9	B66	-1.0	293	5.83E6	Surface damage	
10	B63	0.1	552	3.60E4		0.18mm
10	B23	0.1	552	1.11E5		0.18mm
10	B27	0.1	517	1.00E5		0.13mm
10	B60	0.1	483	4.58E5		0.18mm
10	B73	0.1	483	1.33E6		0.15mm
10	B37	0.1	414	7.39E6		0.15mm
10	B71	0.1	414	1.00E7	Did not fail	
10	B51	0.1	379	1.00E7	Did not fail	
11	B33	0.5	690	3.60E4		0.18mm
11	B8	0.5	621	5.60E4	Surface damage	
11	B70	0.5	552	1.08E5		0.15mm
11	B40	0.5	517	3.63E5		0.15mm
11	B34	0.5	517	1.00E7	Did not fail	
11	B38	0.5	483	1.00E7	Did not fail	

R20431/35

TABLE C-4. TEMP = 260°C 0.38mm DEFECT

Figure	S/N	Stress Ratio	Maximum Stress (MPa)	Cycles to Failure	Remarks	Defect Size
12	7	-1.0	414	2.25E4		.28mm
12	13	-1.0	379	1.80E4		.38mm
12	15	-1.0	345	1.76E4		.38mm
12	10	-1.0	345	7.93E5		.28mm
12	8	-1.0	310	2.07E6		.36mm
12	9	-1.0	276	4.07E6	Failed outside flaw	
12	6	-1.0	241	1.00E7	Did not fail	
13	B36	0.1	483	7.85E4		.25mm
13	B47	0.1	414	7.48E4		.28mm
13	B65	0.1	345	6.25E4		.36mm
13	12	0.1	345	9.26E4		.41mm
13	4	0.1	310	1.00E7	Did not fail	
13	16	0.1	310	1.00E7	Did not fail	
13	11	0.1	310	1.00E7	Did not fail	
14	19	0.5	552	6.68E4		.36mm
14	14	0.5	483	1.08E5		.43mm
14	20	0.5	448	5.61E6		.36mm
14	17	0.5	414	7.44E4		.46mm
14	5	0.5	414	9.60E5		.33mm
14	3	0.1	379	1.00E7	Did not fail	

R20431/35

TABLE C-5. TEMP = 260°C K_t = 1.0, 30 Hz/2 MINUTE DWELL

<i>Figure</i>	<i>S/N</i>	<i>Stress Ratio</i>	<i>Maximum Stress (MPa)</i>	<i>Cycles to Failure</i>	<i>Remarks</i>
16	37	0.7	690	1.00E7	
16	39	0.7	758	1.00E7	
16	2	0.7	772	1.00E7	
16	79	0.7	827	3.02E6	
16	29	0.7	862	8.16E5	
16	28	0.7	862	2.93E6	
16	1	0.7	896	4.80E5	
15	31	0.5	621	1.00E7	
15	35	0.5	655	3.22E6	
15	36	0.5	655	1.87E6	
15	27	0.5	690	4.63E6	
15	34	0.5	758	1.03E6	
15	28	0.5	827	5.52E5	

R20431/35

APPENDIX D

MONTE CARLO SIMULATION

Monte Carlo simulation involves the construction of a model of an entire system in terms of individual statistical events (elements) representing the individual components of the system. In particular, the system (crack growth from an initial flaw) is divided into elements whose behavior can be quantified in terms of probability distributions for each of the possible states of the system. The interrelationships among the elements are also incorporated into the model. This process provides a means of dividing the model-building job into smaller component parts, combining these parts in their natural order, and allowing the computer to present the effects of their interaction on the behavior of the system.

A Monte Carlo simulator was built which allows sampling from up to three different defect distributions. The user specifies frequency of sampling, distribution type, and distribution parameters for each distribution. Distribution type is restricted to lognormal or two parameter Weibull. The three distributions may be thought of as representing initial material quality (IMQ), repairable FOD (RFOD), and non-repairable FOD (NRFOD).

The simulator first attempts to sample from the IMQ distribution. If the sampling frequency for the IMQ distribution is non-zero, a uniform random number [0,1], RN is generated. If RN is less than the specified sampling frequency, the IMQ distribution is sampled from, producing a random crack size. Applied stress for 10^7 cycles is calculated from the equation:

$$\sigma = K_{th} / \sqrt{\pi a / QF}$$

where K_{th} is the input threshold stress intensity value. If, however, RN was greater than the sampling frequency the simulator attempts to sample from the RFOD distribution. The same logic is applied until either a cracksize has been generated or the simulator has attempted to sample from all three distributions. Since the sampling frequencies sum to 1.0, a cracksize is always generated.

The above logic is repeated 1000 times to generate 1000 stresses. A heapsort routine then sorts the stresses in ascending order. To determine the "average" applied maximum stress, the 500th of the 1000 stresses is selected. The "25th" applied maximum stress provides the 25/1000 or 2½% lower bound. The corresponding alternating and mean stresses for the Goodman diagram are calculated for the input stress ratios and printed out.

Tables D-1 and D-2 show sample inputs and outputs respectively.

TABLE D-1. SAMPLE INPUT DATASET

Simulate All Specimens; Use KTH Not Closure Corrected				
• XBAR	SIGMA	%	Type (IMQ, from Blade Inspections)	
-3.3248	0.0500	0.00	L (71.02%)	
• BETA	ETA	%	Type (FOD, Repairable)	
1.3473	0.0082	0.00	W (18%)	
• XBAR	SIGMA	%	Type (Shift Non Repairable To 0.015)	
-1.824	0.495	1.00	L (0.08%)	
• R	KTH			
0.1	4.7			
0.5	3.2			
0.7	2.3			
-999.				

R20431/28

TABLE D-2. SAMPLE OUTPUT DATASET

Simulate All Specimens; Use KTH Not Closure Corrected				
• XBAR	SIGMA	%	Type (IMQ, from Blade Inspections)	
-3.3248	0.0500	0.00	L (71.02%)	
• BETA	ETA	%	Type (FOD, Repairable)	
1.3473	0.0082	0.00	W (18%)	
• XBAR	SIGMA	%	Type (Shift Non Repairable to .015)	
-1.824	0.495	1.00	L (0.08%)	
• R	KTH			
0.1	4.7			
0.5	3.2			
0.7	2.3			
-999.				

Lognormal Distribution for IMQ.

Weibull Distribution for Repairable FOD.

Lognormal Distribution for Non-Repairable FOD.

Data Analysis for Stress Ratio = 0.10000

Simulated Mean Stress for 50% Probability = 20.235

Simulated Mean Stress for 2.5% Lower Bound = 6.8894

Simulated Alternating Stress 50% Probability = 16.556

Simulated Alternating Stress for 2.5% Lower Bound = 5.6367

Data Analysis for Stress Ratio = 0.50000

Simulated Mean Stress for 50% Probability = 35.888

Simulated Mean Stress for 2.5% Lower Bound = 11.653

Simulated Alternating Stress 50% Probability = 11.963

Simulated Alternating Stress for 2.5% Lower Bound = 3.8844

Data Analysis For Stress Ratio = 0.70000

Simulated Mean Stress for 50% Probability = 45.551

Simulated Mean Stress for 2.5% Lower Bound = 14.388

Simulated Alternating Stress 50% Probability = 8.0384

Simulated Alternating Stress for 2.5% Lower Bound = 2.5391

R20431/28